UNIVERSIDAD NACIONAL AUTÓNOMA DE MÉXICO

PROGRAMA DE POSGRADO EN ASTROFÍSICA

Instituto de Ciencias Nucleares, Ciudad Universitaria.

Modeling Strongly Interacting Supernovae

Que para optar por el grado de:
Doctor en Ciencias (Astrofísica)

PRESENTA:

M. en C. Felipe Ventura Vargas

TUTOR PRINCIPAL

Dr. Fabio De Colle,

Instituto de Ciencias Nucleares

Ciudad de México, Agosto 2023

"The saddest aspect of
life right now is that
science gathers knowledge
faster than society
gathers wisdom."
Isaac Asimov

Agradecimientos

aaa Uma frase

aaa

Abstract

This thesis discusses the environment of interacting supernovae and the challenges in accurately modeling them due to the limited amount of data, and to the complexity of the physical processes involved.

We discuss the classification system of supernovae and how interaction with the environment can modify their spectral properties, leading to a misclassification. Advanced computational techniques such as machine learning and genetic algorithms are necessary to provide a more precise understanding of these transients. The methodology section describes the use of hydrodynamic codes, radiation codes, and optimization techniques to model the physical properties of the environment of interacting supernovae in an independent and automated manner.

Two papers are presented in subsequent chapters. In the first one, we couple a hydrodynamic code and a genetic algorithm to investigate the transition of supernova SN 2014C from type Ib to type II, which occurred around 100 days after the explosion. This transition is believed to be the result of the interaction between the supernova shock wave and a massive shell previously ejected from the progenitor star. We use numerical simulations to model the propagation of the shock through the star and its wind, as well as the interaction of the ejecta with the shell. We employ a genetic algorithm to determine the structure and location of the shell, which is found to have a mass of 2.6 $M_\odot$ and extend from 1.6 $\times 10^{16}$ cm to 1.87 $\times 10^{17}$ cm. The shell was ejected approximately $60/(v_w/100 \text{ km s}^{-1})^*$ years before the supernova explosion, and has a density stratification with an average behavior $\sim r^{-3}$, but with large density fluctuations.

In the second paper (currently in process) we employ a machine learning algorithm trained on 6000 simulations to determine the angular distribution of the circumstellar material. The study investigates the behavior of the shell surrounding the progenitor of SN 2014C and

*Where v_w is the wind velocity

explores variations in four parameters that describe the general structure of the circumstellar medium. The simulations produce synthetic data that mimic observed emission, which is used to train a neural network to map observed emission to the underlying parameter space. This approach enables us to infer parameter values from observational data and gain insights into the characteristics of interacting supernovae. In particular, it is confirmed that the radio and X-ray observations are more consistent with the SN 2014C being highly asymmetric, with the region emitting the X-ray about ~ 100 times denser than the region emitting in radio. The study highlights the potential of combining simulations and machine learning to improve our understanding of astrophysical systems and has important implications for future studies of supernovae and other phenomena. By using a combination of observational data, simulations, and machine learning, we can better understand the behavior of complex systems and make more accurate predictions about their evolution and characteristics.

Contents

Chapter 1

Introduction

Generated by Midjourney Algorithm

Supernovae are like cosmic fireworks, exploding in a blaze of glory and lighting up the universe with their brilliance. These awe-inspiring events give us a fascinating insight into the stars that created them, they also play a crucial role in the distribution of chemical elements within galaxies and are instrumental in galaxy feedback. These explosive events not only release a significant amount of newly synthesized elements into the interstellar medium, but they also provide the necessary energy and momentum to influence the surrounding gas and trigger subsequent star formation. The enriched elements released by supernovae remain within the galaxy, contributing to an increase in overall metallicity and serving as building blocks for the formation of new stars.

By studying shockwaves and debris left behind by these massive explosions, we can learn a lot about their progenitor stars and their evolution. So, it's no surprise that the study of supernovae has become an important tool for astronomers to unravel the mysteries of the cosmos.

Stars are some of the most complex and dynamic objects in the universe, each one with its own characteristics and life cycle. And when massive stars (with more than 8 $M_{\odot}$) reach the end of their lives, they can produce a variety of core-collapse supernovae. In the next few pages, we will briefly discuss the fascinating world of supernova classification and explore the different types of stars that can give rise to these explosive events.

1.1 Supernovae and their progenitors

Stars are "giant balls" of plasma in hydrostatic equilibrium, engaged in a constant battle against and gravity. Before collapse, the core of a star possesses enough temperature to maintain processes of nuclear fusion, wherein lighter elements combine to form heavier elements. As a result, massive stars with $\gtrsim 8$ solar masses ($M_{\odot}$), which lead to supernova explosions, are composed of layers (Figure 1.1), with the heaviest chemical elements situated in the core and the lightest in the outermost layers at the end of their life cycle (Janka and Mueller 1996).

As nuclear fusion occurs in the core of a star, gamma-ray photons are produced, and their interaction with the gas heats up the environment, resulting in high temperatures and pressure within the stellar core. At the end of a star life cycle, two different paths may occur: stars with less than 8 M$\odot$ do not reach temperatures high enough to fuse elements heavier than Oxygen and Neon, resulting in a gradual expansion of the outer layers and the formation of a white dwarf. These stars, however, do not cross the line of degeneracy, where the core becomes degenerate due to quantum mechanical effects. On the other hand, stars with more than 8 M$\odot$

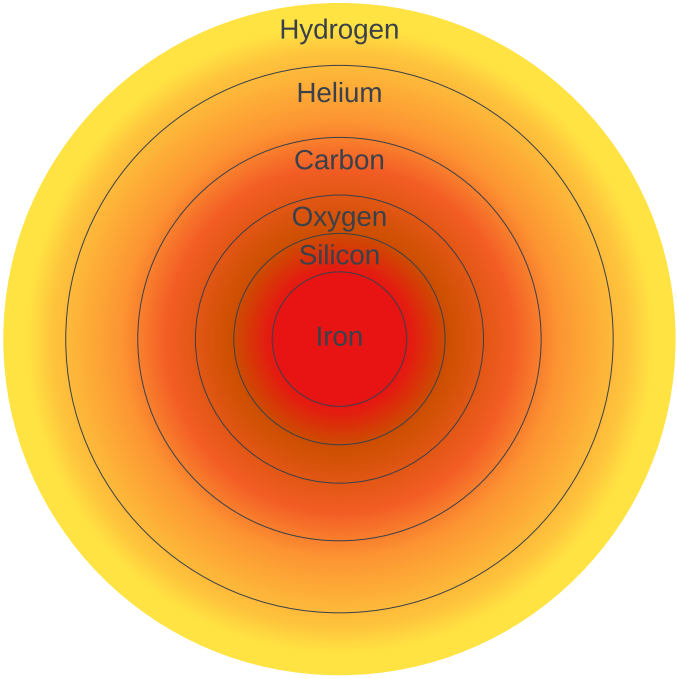

Figure 1.1: "*Onyon Layers*" scheme of the stellar structure before core collapse. Stars burn elements, leaving heavier elements in the core and lighter elements in the outer parts.

contract enough to reach temperatures that allow them to fuse all elements up to iron (Fe). However, since iron has the highest binding energy per nucleon, fusion involving iron becomes an endothermic reaction, consuming more energy than it adds to the system (Janka, Hanke, et al. 2012). The formation of iron through nuclear fusion takes a toll on the progenitor star, causing the material to contract quickly due to the loss of energy. This contraction results in a pressure that is no longer sufficient to maintain hydrostatic equilibrium. The increase in pressure and temperature triggers a series of nuclear processes that release an enormous amount of energy, approximately $\sim 10^{49}$ ergs are emited as light, $\sim 10^{51}$ ergs as kinetic, and $\sim 10^{53}$ ergs as neutrinos (Heger, Fryer, et al. 2003), leading to the birth of a Supernova (SN).

Supernovae (SNe) are explosive phenomena that signal the end of a massive star's life. These events can occur in binary systems, or in massive stars at the conclusion of their evolutionary process. SNe can take different forms depending on the circumstances in which they occur. Core-collapse SNe (Heger, Fryer, et al. 2003) happen during the final stages of evolution of stars with more than 8 $M_\odot$ and are named after the mechanism that triggers them. In contrast, Type Ia SNe occur in binary systems where a white dwarf fuses with a white dwarf or it accretes mass from a bigger companion until it reaches the Chandrasekhar

limit, 1.44 $M_{\odot}$ (Chandrasekhar 1931).

As mentioned, Type Ia SNe are different from core-collapse SNe, since they are not the end of a star life cycle; they are actually the result of a white dwarf fusing with a companion or, as more recent studies show, a fusion between two white dwarfs, causing it to explode in a thermonuclear reaction (da Silva 1993). Despite the two different physical mechanisms that create supernovae, the supernova classification system is mainly based on spectroscopy and light curve behavior (Chevalier and Fransson 2003; Janka, Hanke, et al. 2012).

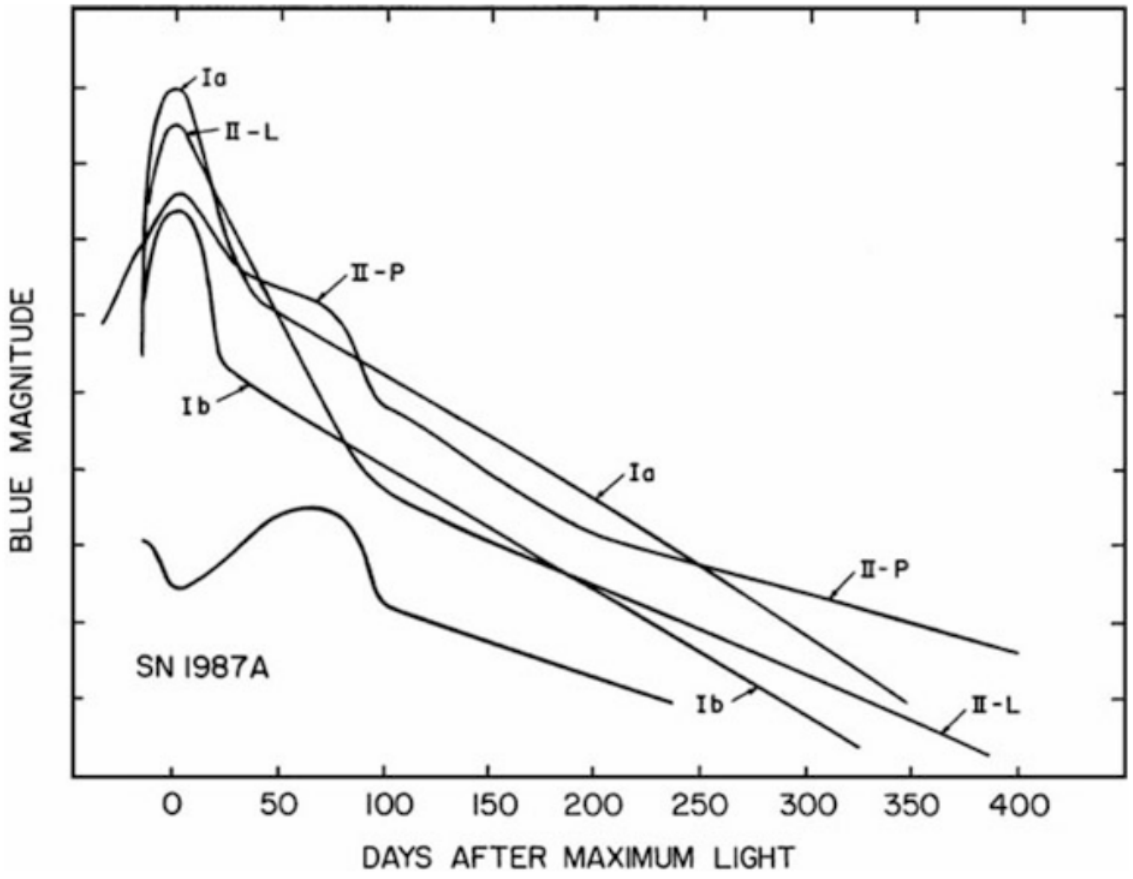

Figure 1.2: Comparative Light Curves of SN Ia, Ib, II-L and II-P. From Branch and Wheeler 2017b

1.1.1 SNe Classification System

There are two main spectroscopic types of SNe: Type I and Type II. Type I SNe do not exhibit hydrogen lines in their spectra, while Type II SNe display prominent hydrogen lines

(Branch and Wheeler 2017a). These two main types of SNe are further classified based on their spectra (Type I) and their light curve slope and spectra (Type II).

To better understand how SNe are classified, refer to Figure 1.3, which presents a schematic diagram of the SN classification system. For example, Type Ia SNe are characterized by the absence of hydrogen lines but the presence of silicon (Si) lines, while Type II-P SNe display a plateau in their light curves and prominent hydrogen lines in their spectra. Spectroscopy and light curve behavior are the main tools used to classify SNe (da Silva 1993; Chevalier and Fransson 2003; Janka, Hanke, et al. 2012).

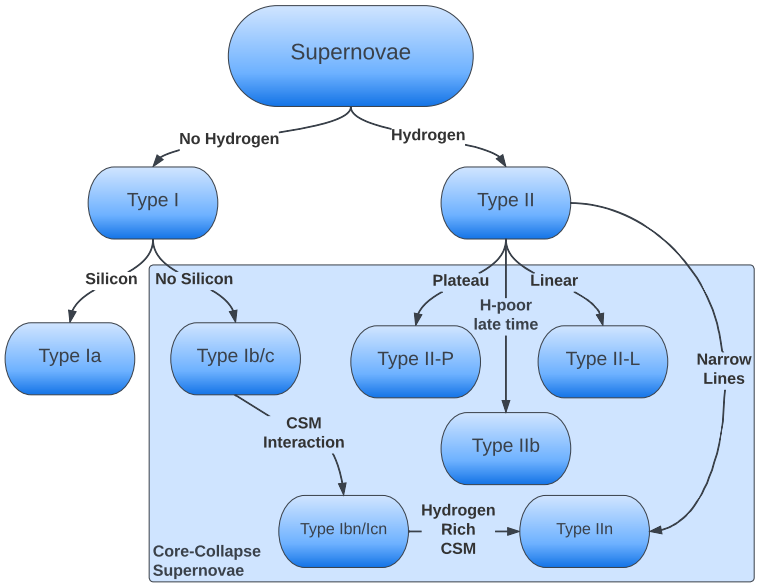

Figure 1.3: There are two main types of SN, Type I (without hydrogen) and Type II (with hydrogen). Type I SNe sub-classification is made according to the presence of spectral lines of different elements, while Type II SNe are mainly sub-classified according to the slope of its light curve. SN with light curves presenting a *Plateau* are classified as type II-P, while SNe presenting a linear decay in their light curve are classified as Type II-L. Interacting SNe are identified by the presence of narrow lines in their spectra, emitted when the shock wave from the SN starts interacting with a dense CSM, creating peculiar transitional SNe that might change their classification due to the emission or absorption of material that was not present in the progenitor before explosion.

In a study conducted by Perley et al. 2020, based on a sample of 1206 supernovae with magnitudes $m < 18.5$, it was found that 72.5% of the supernovae were of type Ia, 26% were core collapse supernovae, and 1.5% belonged to other types. Among the core collapse super-

novae, 72.2% were hydrogen-rich (H-rich) while 27.8% were hydrogen-poor (H-poor). Within the H-rich group, 75.7% were classified as type II supernovae (SN II), 6.6% as SN IIb, 14.2% as SN IIn, and 3.5% as superluminous supernovae of type II (SLSN II). In contrast, within the H-poor group, 19.5% were identified as type Ic-BL supernovae (SN Ic-BL), 9.2% as SN Ibn, 12.6% as SLSN I, and the majority, 58.6%, as SN Ic/c. A scheme of the SN distribution can be seen in figure 1.4. These findings provide valuable insights into the distribution and categorization of supernovae in the observed sample.

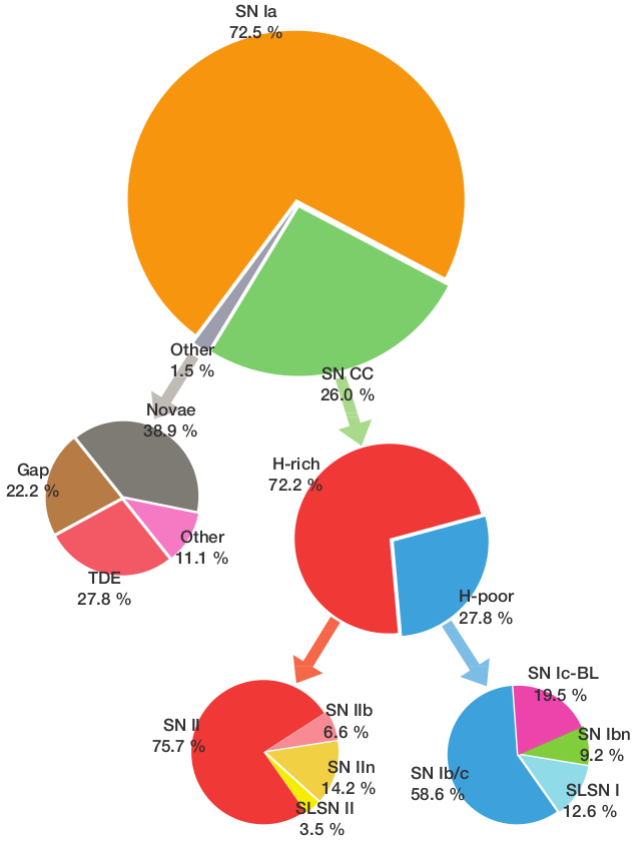

Figure 1.4: Distribution of Supernova Types in a Sample of 1206 Supernovae This figure presents the distribution of supernova types based on a sample of 1206 supernovae with magnitudes m ¡ 18.5. The majority of supernovae in the sample were type Ia (72.5%), followed by core collapse supernovae (26%) and other types (1.5%). Among the core collapse supernovae, there was a distinction between hydrogen-rich (72.2%) and hydrogen-poor (27.8%) supernovae. The figure provides insights into the relative occurrence of different supernova types within the observed sample. Extracted from Perley et al. 2020.

1.1.2 Type I SNe

SNe that do not present hydrogen spectral lines are classified as type I SNe (Filippenko 1997). SNe Type I are sub-classified into three main sub-classes depending on the lack or presence of silicon (Si) and helium lines: SN Ia, SN Ib, and SN Ic. The progenitor of type Ib/c SNe are stripped-envelope stars that have lost their outermost layers due to strong mass losses, while the progenitors of type Ia SNe are white dwarfs. In the early phase of the evolution of a SN, when the explosion is still dense enough to be optically thick to electromagnetic radiation, only spectral lines from the outermost layers of the star (where there are the lightest elements) can be detected.

1.1.2.1 Type Ia

A white dwarf in a binary system can accrete material from its companion star, increasing its mass and eventually leading to the Chandrasekhar limit - around 1.44 $M_\odot$ - and reaching enough mass to start thermonuclear reactions. Type Ia SNe have a very characteristic behavior. Since the explosion in this kind of system always occurs burning nearly all its mass, the width and the peak of the light curve acquire a fixed relation. Thus, such types of SNe are used as *"standardizable candles"*. Type Ia SNe present silicon (Si), iron (Fe), magnesium (Mg), and calcium (Ca) lines in their spectra (Provencal et al. 1998).

1.1.2.2 Type Ib/c

SNe Ib and Ic progenitors are usually unstable stars like Wolf-Rayet, which are progenitors that undergo episodes of mass loss before the collapse, possibly creating a dense CSM around their progenitor. These SNe do not present hydrogen lines because the hydrogen present in the outermost layers has already been ejected from the progenitor. Disregarding the presence of He, the spectrum of SNe Ib and SNe Ic are very similar. The amount of He in a SN can be small, making the classification between these two types ambiguous. The main features of SNe Ib are the presence of He lines and no signs of Si. Still, SNe Ic usually do not present He (Branch and Wheeler 2017a).

1.1.3 Type II-P/L

The light curve of the SNe II-P does not fall as quickly as other types of SNe, remaining almost constant for $\approx$ 100 days, as can be seen in figure 1.2. The progenitor of SNe II-

P/L are red super-giants (RSGs) with mass loss rates $10^{-6} < \dot{M} < 10^{-4}$ $M_\odot$ yr^{-1}. Their winds have a velocity $v_w > 10$ km s^{-1}. These SNe do not present a highly dense CSM, CSI (circumstellar interaction) is detected mainly in nearby galaxies (Chevalier, Fransson, and Nymark 2006). Low-density CSM and CSI might be detected by Balmer Lines and He I (Chugai, Chevalier, and Utrobin 2007; Faran et al. 2014). During the early phases of the SN explosion, its ejecta is optically thick. However, as it expands and becomes less dense, the material starts to become optically thin. SNe then enter into the nebular phase, where photons are released since the environment starts to become optically thin and the density is low enough so forbidden transitions are allowed. After the peak in the light curve, the emission from all ejecta is observed. Subsequently, the light curve shows an exponential decay and the temperature drops adiabatically, since photon energy is transferred to the outermost layers of the SN and transformed into kinetic energy (Branch and Wheeler 2017a).

In the special case of SNe II-P, the light curve shows a plateau. Red supergiant (RSG) have their outermost layers filled with hydrogen. When the collapse happens, their outermost layers are heated above the hydrogen photoionization temperature (≈ 10000 K). As the ejecta expands and cools adiabatically, the heated hydrogen recombines. A cooling recombination phase starts, emitting mostly of the radiation responsible for the light-curve plateau. The duration of this plateau phase depends on the amount of hydrogen to be recombined and also on the number of radioactive elements like ^{56}Ni, ^{56}Co, which can extend the duration of the plateau phase. ^{56}Ni decays into ^{56}Co with a half-life of 6 days, however, its contribution is not important until the ejecta becomes optically thin and photons leave it. Subsequently, there is the contribution of ^{56}Co, which has a half-life of 80 days and decays into ^{56}Fe, increasing the intensity of the observed luminosity for a longer time, creating the plateau-tail phase (Branch and Wheeler 2017a).

1.2 Interacting Supernovae (iSNe)

So far, we have discussed the most common types of SNe and the standard classification system. But there are also other types of SNe that are the cause of great debate in the academic community, the "strongly interacting" SNe or, for short, I propose iSNe. These SNe can convert almost 50% of their kinetic energy into luminosity, emitting $\sim 10^{51}$ erg as radiation. The origin of this type of transient is still a subject of debate. These transients are believed to potentially arise from highly unstable progenitors such as Wolf-Rayet (WR) stars Benetti, Cappellaro, et al. 2006; Fraser et al. 2013; Pastorello, Smartt, et al. 2007) or binary

systems Eldridge, Langer, and Tout 2010. In all cases the outermost layers of the stars were stripped away, creating a dense CSM (Chugai 1997; Chugai and Danziger 1994).

iSNe are transients that deceive the spectrum-based classification system, since SNe of many types that interact with a dense CSM might become part of this SN subclass. Examples of these transients are the SN 2006jc, a Wolf-Rayet star that exploded and interacted with a dense CSM (Foley et al. 2007), the SN 2014C that in its early days of observation was classified as type Ib and after a hundred days presented H lines in its spectra (Milisavljevic, Margutti, et al. 2015), and the SN 2002ic, that was first classified as type Ia, then presented characteristics of a type Ic that later on interacted with a dense CSM, becoming a type IIn (Benetti, Cappellaro, et al. 2006).

These transients are interesting because the origin of the dense CSM is still a matter of debate. The study of iSNe might help to understand the evolution of its progenitors since the material around stars provides information about it before the collapse, and the emission from the interaction can be studied in order to obtain the distribution of the material in the CSM, its composition, ionization and even to make predictions about how the layers of the progenitor were before the progenitor loses it.

1.2.1 Observations

The expected number of SNe per century and their distribution are influenced by various factors, such as the stellar formation rate, the age distribution of stars, the physical properties of the host galaxy, and other astrophysical processes. On average, it is estimated that there occur approximately 1 to 3 supernovae per century in the Milky Way, our galaxy, and around 4 % are iSNe. However, it is important to note that this estimate can vary depending on the assumptions and models used. A idea of the proportion of each type of SN can be seen in figure 1.4.

There are many examples of iSNe like the SN 1988Z (Foley et al. 2007) and SN 2006jc (Pastorello, Smartt, et al. 2007), SN 2005ip (Chugai and Danziger 1994), the Superluminous SNe IIn SN 2006gy, SN 2006tf, SN 2010jl, SN 2003ma (Branch and Wheeler 2017a), the SN IIn SN 1998S, PTF11iqb, SN 2013cu, SN 1993J, SN 1986J, SN 2009ip, SN 2010mc, SN 2008iy, SN 1961V (Brethauer, Margutti, Milisavljevic, Bietenholz, et al. 2022; Branch and Wheeler 2017a), Type IIn-P SN 1994W, SN 2011ht and SN 1054 (Janka, Hanke, et al. 2012). Some type Ib/c SNe like SN 2006jc (Foley et al. 2007) and SN 2001em (Chugai and Chevalier 2006) have shown signs of strong interaction between the shock and the material ejected just before

the explosion.

In these transients, as the shock front interacts with a massive CSM, that might be really close to the progenitor or far away. In the case the material is close enough, the narrow lines will be detected always in the spectra and the is usually classified as SN IIn from early times. However, when the material is far away the spectrum changes over time, starting to present emission lines from lighter elements, like H, that were not on the spectra at early times, changing their classification to type IIn or type Ibn. For instance, although it is believed that SNe Ib progenitors are mainly highly massive unstable stars, there is evidence for type Ib and IIb supernova progenitors in interacting binary systems (Yoon, Dessart, and Clocchiatti 2017). An interesting case was the SN 1993j (Nomoto et al. 1993), where the broadening of H and He II lines constrain the wind velocity to values up to 170 km s^{-1}, making the SNe inconsistent with believed progenitor, a RSG. Recent studies revealed that SN 1993J originated from a K-type supergiant star with an ultraviolet excess, possibly attributed to nearby hot stars or a hot binary companion. It is classified as a type IIb supernova, and the progenitor was identified in pre-explosion images. The progenitor exhibited a helium-rich envelope that may have influenced the explosion's energy. The massive star responsible for the core collapse had a non-variable red supergiant profile and a mass approximately 15 times that of the Sun. While the companion remains undiscovered, it is highly likely that the supernova progenitor was part of a binary system. The progenitor image is surrounded by faint extended emission, supporting a composite model and specifically an OB association contamination model (Maund et al. 2004). Radio and X-ray light curves suggest an increase in the mass-loss rate around ten thousand years before the explosion. The highly ionized lines showed that CSM was close enough to the exploding star to be heated by the UV and X-rays from shock breakout (Nomoto et al. 1993). The CSI in SN 1993j continued for over a decade (Stevance et al. 2020). This was also observed in SN 1992j, where three days after the explosion it started to present narrow lines of Hα, He II λ4686, Fe X λ6374, Fe XIV λ5303 (Benetti, Patat, et al. 1994). Another example is the SN 2014C (Margutti, Kamble, et al. 2017; Milisavljevic, Margutti, et al. 2015). As shown in Figure 1.5, there was an increase over time in the Hα flux, at 656.28 nm. Initially, four days before the maximum brightness of the SN (t = -4 days), the flux in Hα corresponded to the host galaxy. Then, there was a noticeable increase in the Hα flux over the different epochs (113, 282 and 373 days), as well as an increment in the X-ray emission over time (Figure 1.6). In contrast with the expected behavior we can see in figure 1.2. In general, the light curve is expected to exhibit a gradual decline over time, as demonstrated in Figure 1.2. This decay in brightness can be attributed

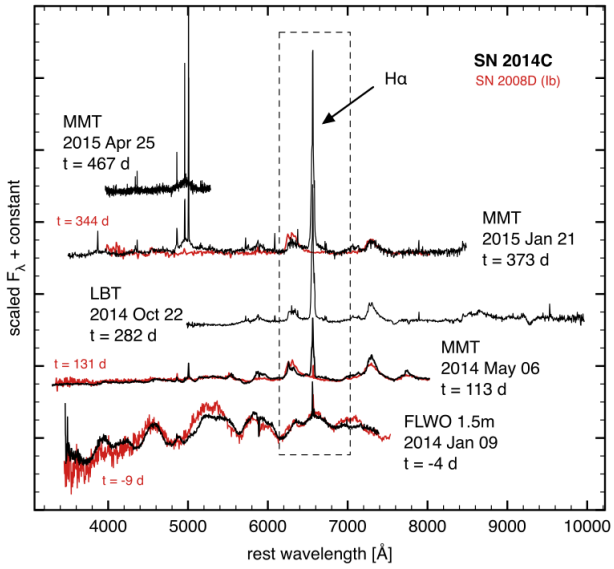

Figure 1.5: The image shows the increase of flux in the Hα line with time observed in the SN 2014C. The time is set in days with respect to the SN peak time. The curves correspond to $t = -4$ days, $t = 113$ days, $t = 282$ days and $t = 373$ days. From Milisavljevic, Margutti, et al. 2015.

to the radioactive decay of unstable isotopes synthesized during the explosion, as well as the expansion of the SN ejecta. By analyzing the characteristics of the light curve, such as its shape, duration, and decline rate, valuable insights can be gained regarding the nature of the SN event and the physical processes involved. This provides strong evidence that the SN ejecta interacted with a shell. The observed X-ray radiation, according to Margutti, Kamble, et al. 2017, is compatible with a bremsstrahlung radiation model with a temperature around $T = 18$ keV, which corresponds to a temperature of 2×10^8 K. Radio, on the other hand, is well fit by non-thermal synchrotron radiation resulting from the interaction between the supernova shock front and the dense CSM.

Another anomalous transient, source of great debate, has been the SN 2001em. The SN was discovered on September 20 of 2001, in the galaxy UGC 11794 (z = 0.1935) at a distance of 83 Mpc (Papenkova et al. 2001). It was first classified as a SN Ib/c (Filippenko and Chornock 2001) and its emission is well fit by a dense CSM created by a Wolf-Rayet star (Chugai and Chevalier 2006). Follow up observations in radio by VLA between October 17 of 2003 and January 1 of 2004 showed that the flux in radio increased (Stockdale, Kaster, et al. 2005) and X-rays observations at later times (April 4 of 2004) made by Chandra X-Ray Observatory in the range 0.5 - 8 keV showed an increase of luminosity $\approx 10^{41}$ ergs s^{-1} which is consistent

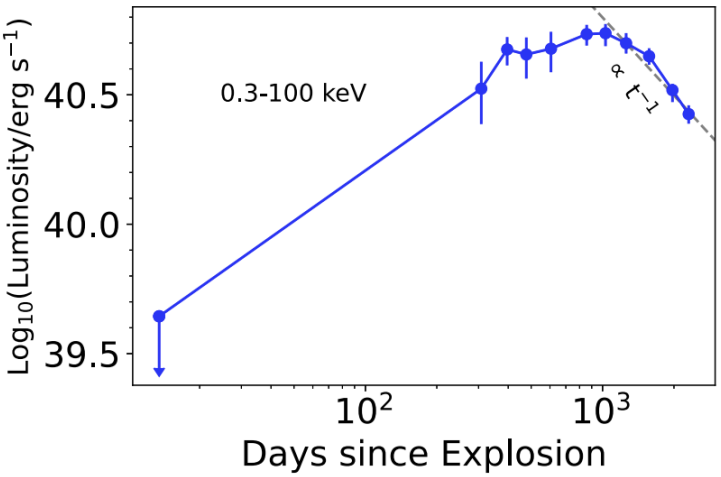

Figure 1.6: X-ray light curve integrated between 0.3 keV and 100 keV. The image shows the evolution of the X-ray light curve as a function of time for the SN 2014C. Unlike expected, the brightness of the SN increases over time. From Brethauer, Margutti, Milisavljevic, Bietenholz, et al. 2022.

with a column density of $N_H = 1.6 \times 10^{21}$ cm^{-2} (Pooley and Lewin 2004). Its spectrum in the range of 5×10^9 to 1.5×10^{10} Hz is from non-thermal emission, with a flux proportional to frequency $F_\nu \approx \nu^{-0.37}$ (Stockdale, Van Dyk, et al. 2004).

1.2.1.1 Types of Interacting Supernovae

The main two categories of SN that arise from iSNe event are the SNe IIn, which shows bright and narrow Balmer H lines, and the SN Ibn, wich present He narrow lines. The SNe type IIn might provide a possible explanation for the Superluminous SNe (SLSNe) (Dessart, Audit, and Hillier 2015) and the SN Ibn were first identified only in more recent years in the SN 2006 jc (Foley et al. 2007). Both SNe types present narrow lines since the material in the CSM moves slower than the ejecta of a normal SN (Branch and Wheeler 2017a). Smith 2017a presents a sub-classification according to all kind of interacting SNe ever observed. In order to keep the study of iSNe simple and didactic, I have gathered the subclassifications made by Smith 2017a in three groups by their common characteristics:

- **Group 1:** The Standard IIn
  Most standard type of interacting SNe. The overall emission is smooth and blue-shifted due to the motion of the shock wave in a dense CSM.

- **Enduring IIn:** Extended CSM, presents narrow lines of Hα emission and has no PCygni absorption features in their spectra (Chandra 2018). The shock wave can cross ~ 20 $M_\odot$ over the years of interaction. Examples are the SN 1988Z and SN 2005ip (Aretxaga et al. 1999; Chugai and Danziger 1994).
- **Superluminous IIn with extended shell:** As bright as SLSNe, with a bolometric luminosity exceeding 10^{44} erg s^{-1}. These SNe presents narrow Hα since their beginning. They would be ordinary iSNe if it were not for their extreme brightness. Examples of these transients include the SN 2006tf, SN 2010jf and SN 2003ma (Fransson et al. 2014; Smith 2017a).
- **Superluminous IIn with compact shell:** Present narrow lines and a slow rise peak (≈ 70 days), fading very quickly in an interval of ≈ 150 days after peak. The only example of this transient is the SN 2006 gy (Smith, Li, Foley, et al. 2007).

- **Group 2:** The *Chameleon* SNe
  As chameleons, they modify their spectra over time. This group might deceive the current system of classification in absence of follow-up observations.

  - **Type IIn, late II-P:** These transients are standard SN IIn. Their only difference is that the interaction luminosity fades enough so the emission of the decay of ^{56}Ni into ^{56}Co can be seen. Examples of these transients are the SN 1994W and the SN 2011ht (Mauerhan, Smith, Silverman, et al. 2013; Smith 2017a).
  - **Transitional IIn:** Show narrow lines only at the beginning of the event and the signs of interaction might be missed if the transients are observed too late. Usually, the transition of classification is from a type IIn to an II-L, with no signs of interaction. Some examples of this SNe are the SN 1998S, PFT11 iqb, SN 2013 cu (Leonard et al. 2000; Shivvers et al. 2015; Smith 2017a).
  - **Normal SN with late-time interaction:** A normal SN that after a few days starts to present narrow lines. The interaction usually appears when the SN emission starts to fade. Examples are SN 1993J and SN 1986J (Matheson et al. 2000; Milisavljevic and Fesen 2013).
  - **Delayed, slow rise, multi-peaked:** This group of SNe has an emission peak during the SN nebular phase, as usual, but, a few days after that, it starts to rise again, forming another peak due to CSM interaction. Sometimes even changing its classification with the presence of narrow Hα lines in its spectra, where there was

no H observed before. A famous case is the SN 2014C (Margutti, Kamble, et al. 2017; Margutti, Alexander, et al. 2018; Milisavljevic and Fesen 2013; Vargas et al. 2022). Other examples are the SN 2009 ip, SN 2010 mc, SN 2008 iy and SN 1961V (Mauerhan, Smith, Filippenko, et al. 2013; Smith 2014).

- **Group 3:** *Exotic* SNe
  - **SN IIn impostors:** Not really a SN. Sub-luminous events that might be caused by eruptions of unstable stars or other unknown events. They present narrow lines due to interaction with a dense CSM caused by dense and steady wind or previous eruptions. One example of this kind of transient is the SN 2008S (Smith, Li, Silverman, et al. 2011).
  - **Type Ia/IIn or Ia-CSM:** Better seen when the CSM interaction does not overcome the SN Ia spectrum signature (Benetti, Cappellaro, et al. 2006), as it happened with PTF11kx. Some other examples of this transient are SN 2002 ic and SN 2005 gj (Silverman et al. 2013);
  - **Type Ibn:** Instead of having Hα narrow emission, present He λ5876 line. One example is the SN 2006jc (Smith 2017a).
  - **Type Icn:** By the time Smith 2017a published his system of classification, this kind of transient was only theoretical. But recent observations have discussed candidates for Typer Icn SNe (Perley, Schulze, et al. 2021; Gal-Yam, Yaron, et al. 2021; Pellegrino et al. 2022). A SN that interacts with a dense CSM and present no signs of H or He, but narrow lines of Ca.

1.2.1.2 iSNe Emission

iSNe need a very efficient mechanism to convert kinetic energy into radiation (Pozzo et al. 2004; Arnett and Meakin 2011), as the region of interaction with the CSM emits much more light than one would expect from a normal SN. A SN usually has around 10^{51} ergs of kinetic energy with an efficiency of 1% in converting this kinetic energy into luminosity (producing $\sim 10^{49}$ ergs), where most of the emission comes from freely expanding ejecta or from material heated by radioactive decay.

Most SNe IIn spectrum do not present strong radio emission (van Dyk et al. 1996)*. The

*Either because this kind of transient does not present radio emission or because the instruments used in are not sensitivie for radio.

interaction with CSM usually leads to an increase in the X-ray emission due to thermal bremsstrahlung and inverse Compton. The analysis of the interaction provides a constraint on $\dot{M}$ and the CSM density. Although there are indications that $\dot{M}$ is not only responsible for a high-density CSM, in some cases the CSM could be formed by a disk from the protostellar phase (Metzger 2010), allowing the progenitor to have a lower constraint in its $\dot{M}$.

1.2.2 Theoretical Models

1.2.2.1 Interaction between the SN shock front and their massive shell

There are three primary regions that contribute to the high luminosity of interacting supernovae (iSNe) besides the usual emission: the CSM pre-shock (1) region, which may already be photoionized by X-ray radiation from the hot post-shocked plasma; the forward shock (2) of the SN, which reaches the material and transfers energy to it; and the ejecta material (3) decelerated by the reverse shock.

Since iSNe come from progenitors with a history of high mass loss, studying their interaction with the CSM can help constrain the mass-loss history and properties of the surrounding environment. Figure 1.7 illustrates the four main regions responsible for the emission observed in iSNe:

The four regions are:

- Zone 4: Freely expanding supernova ejecta that emits in the optical spectrum, showing broad emission and absorption lines;
- Zone 3: Decelerated supernova ejecta that encounters the reverse shock (emits in X-ray and radio);
- Zone 2: CSM that has been hit by the forward shock (emits X-ray and radio);
- Zone 1: Unshocked CSM outside the forward shock (the medium may be photoionized, and absorption lines may appear).

In a Type IIn supernova, the narrow component of the hydrogen lines is produced by ionized circumstellar gas, while the broad components and flux increase in various wavelengths are produced by the shocked ejecta. The interaction process can be either radiative, where photons are scattered and absorbed by the dense environment, or hydrodynamical, where

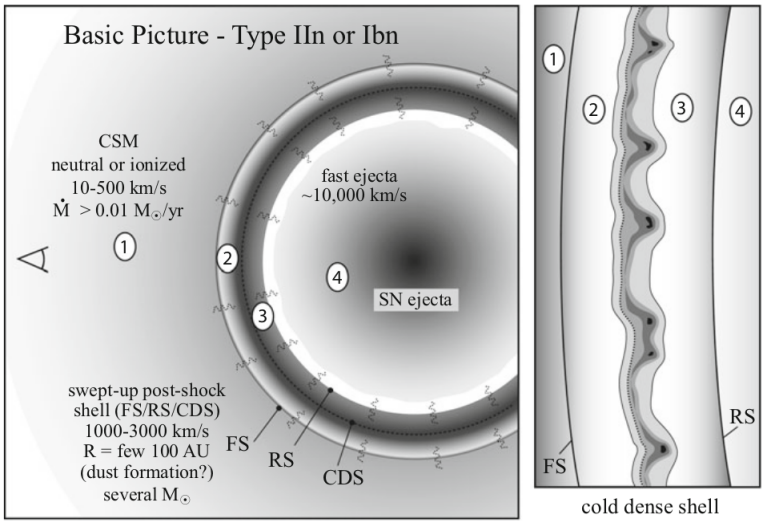

Figure 1.7: The components responsible for the emission observed in interacting supernovae (iSNe): Zone 1) Absorption by unshocked material. Zone 2) Emission from the interaction between CSM and FS. Zone 3) Material from the ejecta decelerated by the reverse shock (RS). Zone 4) Standard emission from a supernova, consisting of freely expanding material, cooling adiabatically. Adapted from Branch and Wheeler 2017a.

the ejecta collides with the dense region, emitting X-rays due to thermal bremsstrahlung and inverse Compton.

1.2.2.2 Origin of the massive shell

The dense CSM around iSNe progenitors can originate from giant eruptive LBVs (Hoffman et al. 2008), which have high mass-loss rates ranging from $\sim 10^{-3}$ to $\sim 10^{-2}$ $M_{\odot}$ yr^{-1} (Moriya and Maeda 2014). Observations before the explosion of SN 2005gl showed an LBV-like star as the progenitor (Gal-Yam and Leonard 2009). There is also evidence that the CSM might be formed due to binary interaction with compact objects (Chevalier 2012). Examples of high-density, clumpy CSM caused by LBV eruptions include SN 1993J (Dwarkadas 2011) and SN 2014C (Vargas et al. 2022).

1.3 Thesis Objectives

The aim of this thesis is to characterize supernovae that interact with massive shells by employing cutting edge methods.

In my first paper, I analyzed the density profile and metallicity of the SN 2014C. In future works, I plan to further improve the accuracy of these measurements, determine the shell speed in the CSM, and gain insight into the origins of these massive shells. By studying the coupling between X-ray and synchrotron emission, it may also be possible to determine microphysical parameters related to the particle acceleration mechanism. And also, apply machine learning techniques to determine the initial conditions of the systems in a fast and automated way, avoiding the bias of a human researcher.

The progenitors of the dense CSM responsible for these interacting supernovae may be giant eruptive LBVs with high mass-loss rates ranging from $\sim 10^{-3}$ to $\sim 10^{-2}$ $M_{\odot}$ yr^{-1} (Moriya and Maeda 2014), or binary systems involving compact objects (Chevalier 2012). Evidence of these progenitors has been found in observations of SN 2005gl, which displayed an LBV-like star before the explosion (Gal-Yam and Leonard 2009), as well as SN 1993J and SN 2014C, which both exhibited high-density, clumpy CSM possibly resulting from LBV eruptions (Dwarkadas 2011; Vargas et al. 2022).

By studying interacting supernovae and their massive shells in detail, we can gain a better understanding of the late-stage evolution of massive stars and the mechanisms that govern their explosive deaths. This knowledge can have implications for a variety of astrophysical phenomena, from the enrichment of the interstellar medium with heavy elements to the formation of compact objects like neutron stars and black holes.

Chapter 2

Methodology

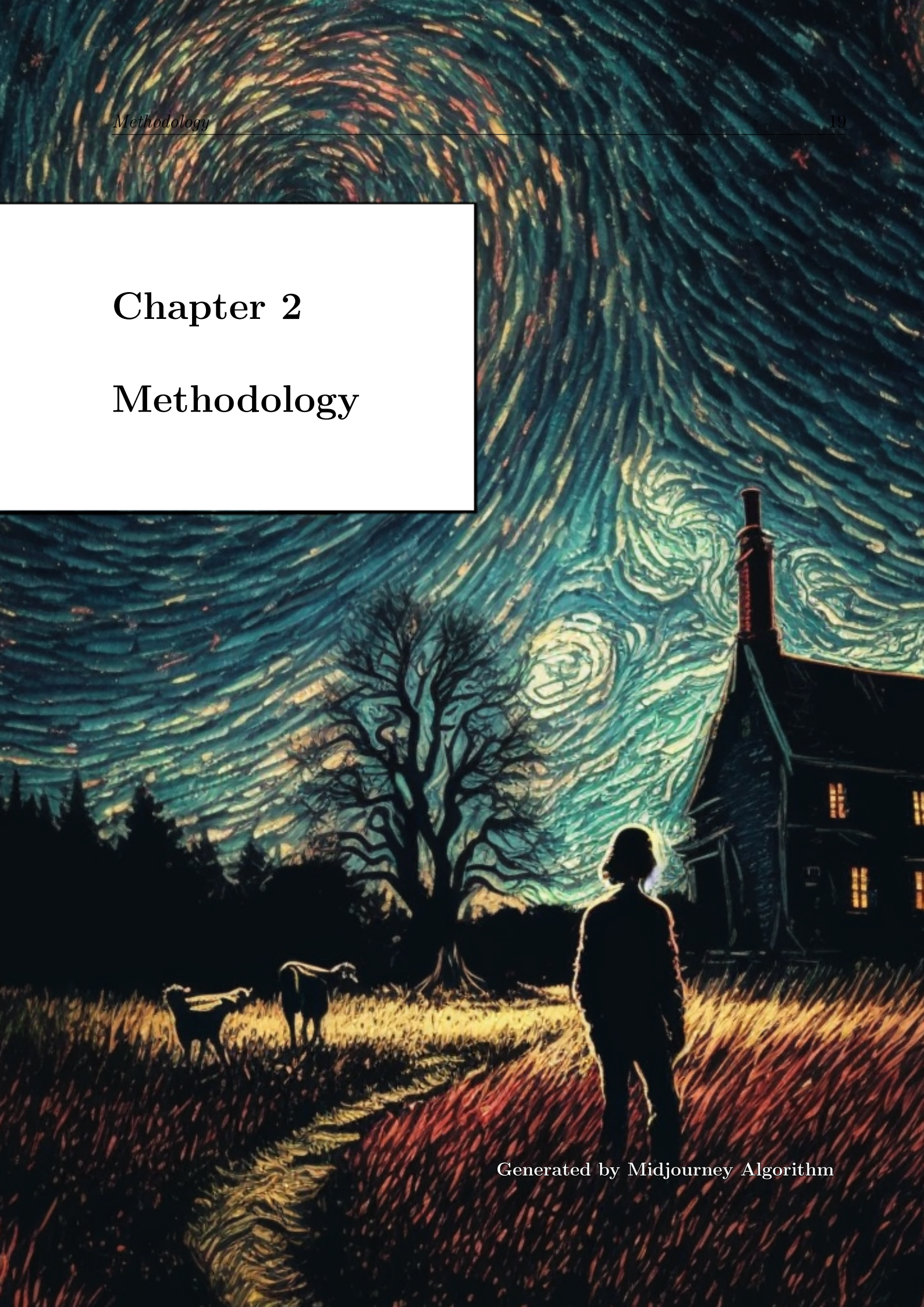

Generated by Midjourney Algorithm

Modeling SNe with strong interaction is a challenging task and requires state-of-the-art techniques. With the evolution of computers, in the last decades, a revolutionary branch of scientific research has developed: the application of optimization algorithms to data analysis to find solutions to problems that would otherwise be very difficult to study. In this section, I will describe the tools employed in this thesis to study strongly interacting SNe.

2.1 Hydrodynamic simulations

Hydrodynamic simulations are made with the code *Mezcal* (De Colle, Granot, et al. 2012). The *Mezcal* code is an adaptive mesh refinement, parallelized, Eulerian code, capable of solving the equations of hydrodynamics, relativistic hydrodynamics, and magnetohydrodynamics. The code employs cartesian, cylindrical, and spherical coordinate systems. In the following, we will assume spherical symmetry and employ a one-dimensional (1D), spherical symmetric grid.

The special relativistic hydrodynamic equations are based on the conservation of three physical quantities: mass, moment, and energy (De Colle, Granot, et al. 2012).

- Mass conservation

$$\frac{\partial D}{\partial t} + \nabla \cdot (D\vec{v}) = 0. \tag{2.1}$$

- Momentum conservation

$$\frac{\partial \vec{S}}{\partial t} + \nabla \cdot \left(\vec{S}\vec{v} + p\vec{I}\right) = 0. \tag{2.2}$$

- Energy conservation

$$\frac{\partial \tau}{\partial t} + \nabla \cdot (\tau\vec{v} + p\vec{v}) = 0, \tag{2.3}$$

where $\vec{v} = \vec{\beta}c$ is the velocity of the fluid, $\vec{I}$ is the identity matrix, c the speed of light. The conserved variables D, $\vec{S}$ and τ, are measured in the laboratory system of reference and are related to the primitive variables ρ, $\vec{u}$ and p by:

$$D = \rho\Gamma, \tag{2.4}$$

$$\vec{S} = Dh\Gamma\vec{v}, \tag{2.5}$$

$$\tau = Dh\Gamma c^2 - p - Dc^2, \tag{2.6}$$

being h the specific enthalpy, and Γ the Lorentz factor,

$$\Gamma = \frac{1}{\sqrt{1-\beta^2}}. \tag{2.7}$$

In a general form, the conservation equations can be written as

$$\frac{\partial \vec{U}}{\partial t} + \nabla \cdot \vec{F}(U) = 0, \tag{2.8}$$

where the vector $\vec{U}$ represents the conserved quantities (mass, momentum, and energy), and the vector $\vec{F}$ represents the flux of these quantities.

To solve the conservation equations in a computational mesh, we discretize the time into small steps, Δt^n, and the space into small cells, Δx_i. The average values of the conserved quantities in a cell i at t^n, are represented by U_i^n. The values at the boundaries are indicated as $U_{i+1/2}$ or $U_{i-1/2}$. The same notation applies to the flux, where the values of the fluxes at the cell boundaries are written as $F_{i+1/2}$ and $F_{i-1/2}$. The averaged quantities over a cell in a given time step are obtained by integrating over the cell volume, i.e,

$$\frac{\partial}{\partial t}\int_{x_{i-1/2}}^{x_{i+1/2}} u(x,t)dx + \int_{x_{i-1/2}}^{x_{i+1/2}} \frac{\partial F(u)}{\partial x}dx = 0 \tag{2.9}$$

Numerically, the time evolution in one dimension is given by

$$U_i^{n+1} = U_i^n - \frac{\Delta t^n}{\Delta x_i}\left(F_{i+1/2} - F_{i+1/2}\right), \tag{2.10}$$

where the cell size is $\Delta x_i = \Delta x_{i+1/2} - \Delta x_{i-1/2}$. The method used to solve the system of equations 2.8 is the Harten-Lax-van Leer (HLL) method (Schneider et al. 1993). The time integration is done using the second-order Runge-Kutta method.

2.2 Radiation Transfer

The amount of energy that passes through an area in a given time is directly proportional to the change in the area and the change in time $E = FdAdt$. The quantity that equals this proportion is known as the flux, F,

$$F \equiv \frac{E}{dAdt}, \tag{2.11}$$

being defined as the energy carried by all rays crossing a certain area per unit of time.

It makes no sense to define the amount of energy carried by just one ray since a macroscopic approximation requires a statistical treatment. To be able to treat the problem of radiation transfer in a differential way, we must then define a new quantity, I_ν. I_ν is the specific intensity, which is the total energy crossing a perpendicular surface dA in a time dt, with a frequency $d\nu$ and moving along the solid angle $d\Omega$;

$$dE = I_\nu dA dt d\Omega d\nu. \tag{2.12}$$

For a small variation loss of the specific intensity, we can write the differential form of the absorption equation as (Rybicki and Lightman 1986)

$$\frac{dI}{I} = -n\sigma dx. \tag{2.13}$$

Where n is the number density, σ is cross section, and x is the position. If n and σ do not depend on x,

$$I(x) = I_0 e^{-n\sigma x}, \tag{2.14}$$

where $I = I_0$ in $x = 0$. When rays interact with matter, energy can be emitted or absorbed. We can define an emission coefficient (j_ν) as the intensity emitted, and an absorption coefficient (α_ν) as the proportion of intensity that is absorbed in a given path. Then we can write the intensity change in a path (s),

$$\frac{dI_\nu}{ds} = j_\nu - \alpha_\nu I_\nu, \tag{2.15}$$

being ds the path that a ray travels and depends on the coordinate system used. For instance, in a cylindrical two-dimensional coordinate system we can write ds as

$$\frac{d}{ds} = \left(\frac{\partial r}{\partial s}\right)\frac{\partial}{\partial r} + \left(\frac{\partial \theta}{\partial s}\right)\frac{\partial}{\partial \theta} \tag{2.16}$$

or

$$\frac{d}{ds} = \left(\frac{\partial r}{\partial s}\right)\frac{\partial}{\partial r} + \left(\frac{\partial \theta}{\partial s}\right)\frac{\partial}{\partial \theta} = cos\theta\frac{\partial}{\partial r} - \frac{sin\theta}{r}\frac{\partial}{\partial \theta}. \tag{2.17}$$

In order to simplify the equation, we define $\mu = cos\theta$. We get

$$cos\theta\frac{\partial}{\partial r} - \frac{sin\theta}{r}\frac{\partial}{\partial \theta} = \mu\frac{\partial}{\partial r} + \frac{\sqrt{1-\mu^2}}{r}\frac{\partial}{\partial \theta}, \tag{2.18}$$

then our equation 2.15 becomes

$$\left[\mu\frac{\partial}{\partial r}+\frac{\sqrt{1-\mu^2}}{r}\frac{\partial}{\partial\theta}\right]I_\nu = j_\nu - \alpha_\nu I_\nu. \tag{2.19}$$

We can define the source function S_ν as the ratio between the emission and the absorption coefficient

$$S_\nu \equiv \frac{j_\nu}{\alpha_\nu}. \tag{2.20}$$

Considering the optical depth τ defined as

$$\tau_\nu = \int \alpha_\nu ds, \tag{2.21}$$

or differentially

$$d\tau_\nu = \alpha_\nu ds \tag{2.22}$$

we can rewrite equation 2.15 in terms of the source function, S_ν, and τ_ν

$$\frac{dI_\nu}{d\tau_\nu} = S_\nu - I_\nu, \tag{2.23}$$

This equation has a formal solution

$$I_\nu(\tau_\nu) = I(0)_\nu e^{-\tau_\nu} + \int_{0\nu}^{\tau} S_\nu(\tau'_\nu)e^{-(\tau_\nu-\tau'_\nu)}d\tau'_\nu. \tag{2.24}$$

This solution depends on the physical properties of the medium. Numerically, the differential equation 2.23 can be rewritten as,

$$I_\nu[n+1] = \frac{j_\nu}{\alpha_\nu} + \left(I_\nu[n] - \frac{j_\nu}{\alpha\,\nu}\right)e^{-\tau_\nu}, \tag{2.25}$$

where the specific intensity in the cell $n+1$ can be computed from the intensity and the values of j_ν, α_ν and τ_ν, where τ_ν is the optical depth along the path between the center of cell n and the center of cell $n+1$. From a numerical distribution of density, $n(r)$, and temperature $T(r)$, we can then evolve the intensity $I(\nu)$ for a range of frequencies in the direction of n.

The code created is composed of two main subroutines. The first subroutine calculates the emission in a cell. The second subroutine uses the spherical symmetry of the system to transform the one-dimensional results of the *Mezcal* code into a two-dimensional region, applying the first subroutine in each of cell of this new mesh and projecting it along the line of sight.

The RT code was developed in Fortran 90 Vargas et al. 2022. The RT code is coupled with the output data from the *Mezcal* code and uses the radiation transfer equations in each cell of the mesh of the output. It considers photoionization, recombination, collisional ionization, cooling and Hα emission.

2.2.1 Free-free emission for thermal electrons

The functions that define the emission and absorption coefficients depend on the physical processes responsible for producing the radiation. For bremsstrahlung (in CGS units) we have (Rybicki and Lightman 1986)

$$j_\nu = \frac{6.8}{4\pi} \times 10^{-38} Z^2 n_e n_i T^{-1/2} e^{\frac{-h\nu}{kT}} G, \tag{2.26}$$

$$\alpha_\nu = 3.7 \times 10^8 T^{-1/2} \frac{Z^2 n_e n_i}{\nu^3} (1 - e^{\frac{-h\nu}{kT}}) G, \tag{2.27}$$

where Z is the atomic number, n_e and n_i are the electron and ion densities, ν is the frequency, G is the quantum correction known as the Gaunt factor ($G \approx 1$ in classical regimes), T is the temperature, k is the Boltzmann constant and h is the Planck constant.

In order to compute the specific flux one must integrate the intensity over the transverse area

$$F_\nu = \frac{1}{D^2} \int I_\nu cos\theta d\Omega. \tag{2.28}$$

The total flux is given by integration over all frequencies

$$F = \int_0^\infty F_\nu d\nu. \tag{2.29}$$

To test the developed code, an example from the book by Ghisellini et al. (2013) was reproduced. It involved calculating the intensity as a function of frequency for Bremsstrahlung emission in a spherical region while varying the density in each position of r correspondent to the observations. The density varied from 10^{10} particles cm^{-3} to 10^{18} particles cm^{-3}. Each curve in Figure 2.1 represents a different density. The temperature was kept constant at 10^7 K for all cases.

As observed in Figure 2.1, the results obtained from the code closely match those presented in the literature, indicating that the code reproduces known outcomes. Both results demonstrate that as the density increases, the behavior of intensity as a function of frequency approaches that of a blackbody. This outcome is expected because as the density

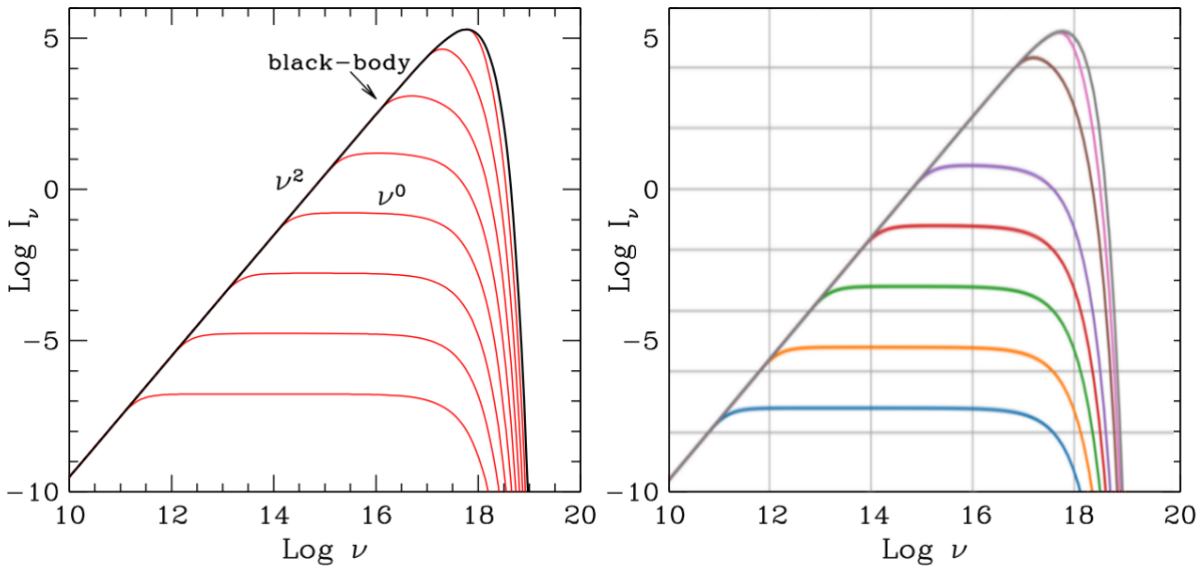

Figure 2.1: Comparison of intensity versus frequency in logarithmic scale. On the left, an image extracted from ghisellini2013radiative. On the right, the Python code's output.

of a medium increases, the collisional rate among particles also increases. Consequently, in a denser medium, particles exchange energy more rapidly and reach the most probable energy distribution associated with thermodynamic equilibrium. In the case of a highly dense medium, this behavior resembles that of a blackbody since, in complete thermal equilibrium, all emission is thermal and solely dependent on temperature.

It is worth noting that the figures shown in the left panel of Figure 2.1 were extracted from Ghisellini et al. (2013), while the right panel presents the results obtained using the Python code.

2.2.2 Photoionization and Recombination

We also consider photoionization and recombination of atoms in the plasma. Since the progenitors of iSNe are produced by unstable progenitors, the medium might already be photoionized, reducing the bound-free absorption cross-section of X-ray emitted in the post-shock region. Additionally, the recombination of material might increase the observed luminosity.

In order to consider these effects we add to the RT code analytical equations for photoionization extracted from Verner, Ferland, et al. n.d. and analytical equations for recombination from Verner and Ferland n.d. Both works present a complete set of analytic fits to non-relativistic photoionization and recombination cross sections for ground states of atoms and ions of elements (H, He, Li, Be, B, C, N, O, F, Ne, Na, Mg, Al, Si, S, Ar, Ca, Fe).

The photoionization cross-section is given as (Verner, Ferland, et al. n.d.):

$$\sigma(E) = \sigma_0 F(y), \tag{2.30}$$

where

$$F(y) = [(x-1)^2 + y_w^2] y^{0.5P-5.5} (1 + \sqrt{y/y_a})^{-P} \tag{2.31}$$

and

$$x = \frac{E}{E_0}, \tag{2.32}$$

$$y = \sqrt{x^2 + y_1^2}. \tag{2.33}$$

In these equations, E is free parameter, known as photon energy in eV, σ_0, E_0, y_w, y_a, P, y_0, y_1 are fit parameters tabled for each element (Verner, Ferland, et al. n.d.). Figure 2.2 shows a comparison between the fit and experimental data, the difference between the model and experimental data is due to Auger effect, which was implemented in our code. Those cross-sections have been corrected by Auger effect (McLaughlin 2001).

In the same way, as it was made for photoionization, in Verner and Ferland n.d. a fit is made for the recombination cross-section. The equation used is

$$\sigma_r(T) = a \left[\sqrt{T/T_0} \left(1 + \sqrt{T/T_0}\right)^{1-b} \left(1 + \sqrt{T/T_1}\right)^{1-b} \right]^{-1}, \tag{2.34}$$

where a, b, T_0, and T_1 are the fitting parameters tabled in the paper for each element.

Defining the mean intensity J_ν as the integral of specific intensity over the solid angle

$$J_\nu = \frac{1}{4\pi} \int I_\nu d\Omega, \tag{2.35}$$

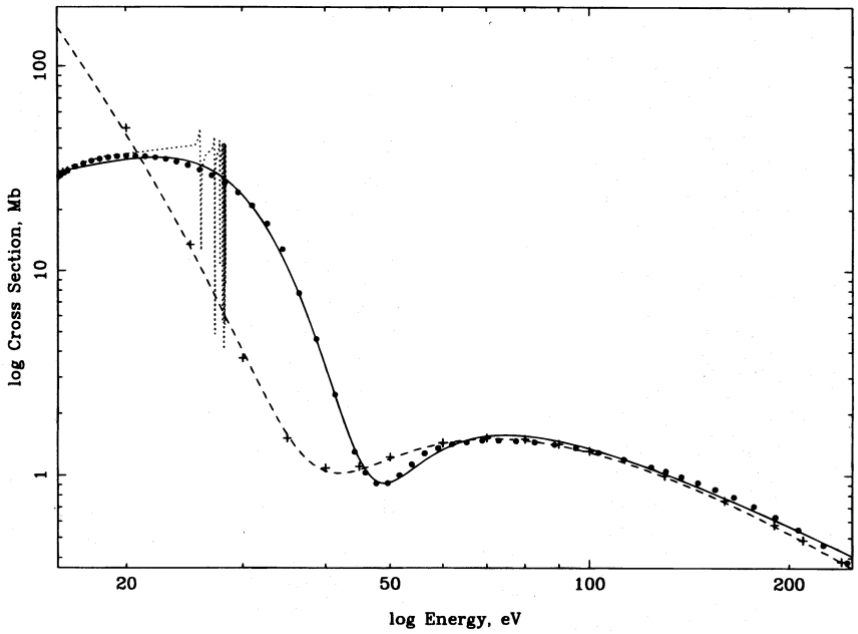

Figure 2.2: Comparison between the experimental photoionization cross-section for Ar I (solid line) and fitted model (dashed line). From Verner, Ferland, et al. n.d. The difference between the model and experimental data is due to Auger effect, which was implemented on the code used in this work.

the photoionization coefficient Φ can be calculated as

$$\phi = 4\pi \int_0^\infty \frac{J_\nu \sigma_\nu}{h\nu} d\nu. \tag{2.36}$$

In order to compute the ionization state of each ion n_i we consider the equilibrium between radiative recombination, collisional ionization, and photoionization

$$\frac{\partial n_i}{\partial t} = \sum_{i=I}^{N} n_e n_{i-1} C_{i-1} + n_{i-1}\Phi_{i-1} + n_e n_{i+1} R_{i+1} - n_e n_i C_i - n_i \Phi_i - n_e n_i R_i \tag{2.37}$$

where

- $n_e n_{i-1} C_{i-1}$
  is the formation rate of the ion i by collision of the ion $i-1$ with free electrons

- $n_{i-1}\Phi_{i-1}$
  is the formation rate of the ion i by photoionization giving the ion $i-1$

- $n_e n_{i+1} R_{i+1}$
  if the formation rate of the ion i by recombination of the ion $i+1$ with electrons

- $n_e n_i C_i$
  is the loss rate of the ion i by collision, forming the ion $i+1$

- $n_i \Phi_i$
  is the loss rate of i by photoionization, forming the ion $i+1$

- $n_e n_i R_i$
  is the loss rate of i by recombination with free electrons, forming the ion $i-1$

where C_i, Φ_i and R_i are respectively the collisional, photoionization and recombination coefficients, and n_e and n_i are the electron and ion numerical densities. In Figure 2.3 we can see

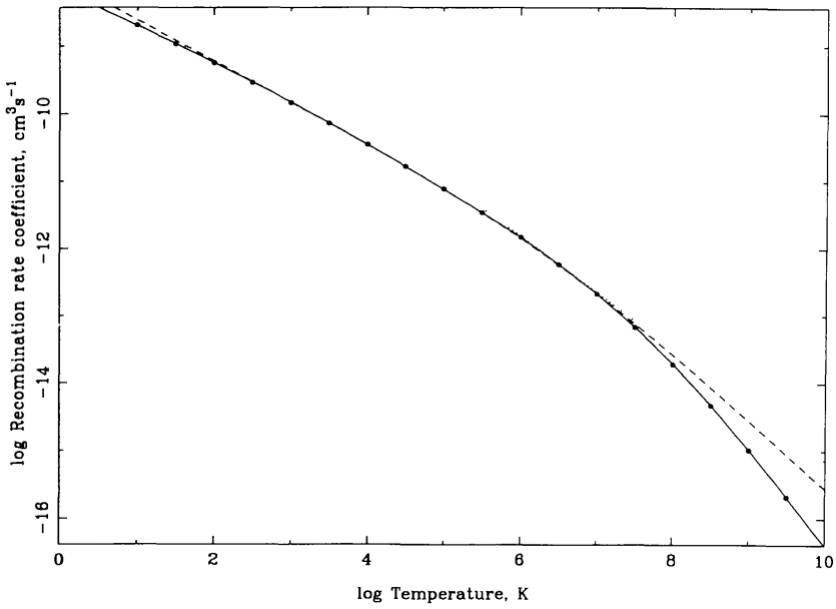

Figure 2.3: Recombination rate coefficient for O VII as a function of temperature. The solid line shows the fitting equation and the circles are the experimental data. From Verner and Ferland n.d.

an example of the recombination coefficient, $R = R(Z, e_i, T)$, as a function of temperature.

In order to understand the recurrence formulas used in the code developed, we make an example of an atom with a few possible ionization states. As an example, we consider lithium (Li), with an atomic number equal to 3. Li has 4 possible states of ionization: the ground state, LiI, and the ions, LiII, LiIII, and LiIV. The ionization network is the following:

- LiI can be formed by recombination of LiII and can be ionized by collision and photoionization, i.e.,

$$\frac{dn_I}{dt} = n_e n_{II} R_{II} - n_e n_I C_I - n_e n_I \Phi_I \tag{2.38}$$

- LiII can be formed by ionization of LiI and recombination of LiIII and can be destroyed by ionization into LiIII and recombination into LiI

$$\frac{dn_{II}}{dt} = n_e n_I C_I n_I + n_I \Phi_I + n_e n_{III} R_{III} - n_e n_{II} C_{II} - n_{II} \Phi_{II} \tag{2.39}$$

- LiIII can be formed by ionization of LiII and recombination of LiIV and can be destroyed by ionization into LiIV and recombination into LiII

$$\frac{dn_{III}}{dt} = n_e n_{II} C_{II} n_{II} + n_{II} \Phi_{II} + n_e n_{IV} R_{IV} - n_e n_{III} C_{III} - n_{III} \Phi_{III} \tag{2.40}$$

- LiIV can be formed by ionization of LiIII and can be destroyed by recombination into LiIII

$$\frac{dn_{IV}}{dt} = n_e n_{III} C_{III} + n_{III} \Phi_{III} - n_e n_{IV} R_{IV} \tag{2.41}$$

Considering that the total Li density is conserved,

$$\frac{dn}{dt} = \frac{d}{dt}(n_I + n_{II} + n_{III} + n_{IV}) = 0, \tag{2.42}$$

and assuming equilibrium between recombination and ionization, we can find a recurrence formula based on the sum of all fractions for the first state of ionization by applying equations 2.38, 2.39, 2.40 and 2.41 in equation 2.42. We can write the first state of ionization as

$$n_I = \frac{n}{B}, \tag{2.43}$$

where

$$B = \left(1 + \frac{\phi_I + n_e C_I}{n_e R_{II}}\right)\left(1 + \frac{\phi_{II} + n_e C_{II}}{n_e R_{III}}\,(...)\right) \tag{2.44}$$

After computing the numerical density of the element in the ground state using equation 2.43, we can calculate the numerical density distribution of states. Ions densities are calculated through recurrence formulas

$$n_{[i+1]} = n_{[i]} \frac{\phi_{[i]} + n_e C_{[i]}}{n_e R_{[i+1]}}\ . \tag{2.45}$$

Then, the electron density is given as

$$n_e = \sum_i \sum_j Z_j n_{[i+1],[j]}. \tag{2.46}$$

Where j and i are index used to represent the different elements and its states of ionization.

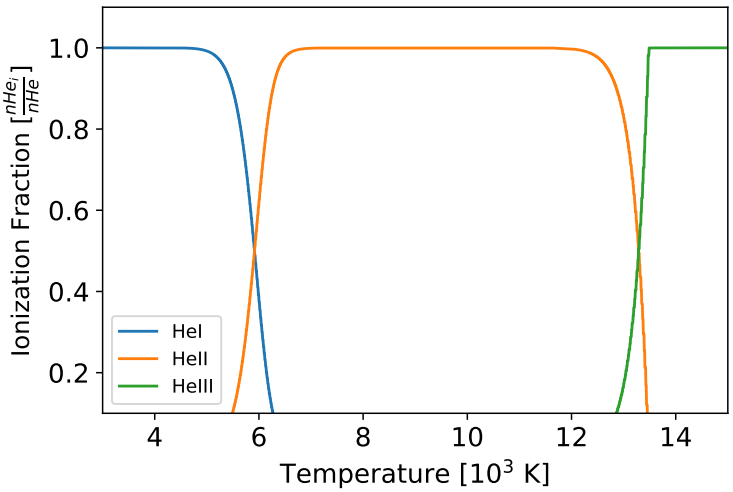

Figure 2.4: Normalized density of states of ionization of Helium, He, as a function of the temperature, from ground state Helium, He I, to Helium two times ionized, He III.

Figures 2.4, 2.5 and 2.6 show examples of the ionization fractions of Helium, Lithium and Carbon (assuming that the photoionization is negligible). As the gas temperature rises there are changes in the state of ionization of the atoms and when a fraction o the ionization energy of each state is reached, the new state of ionization becomes dominant.

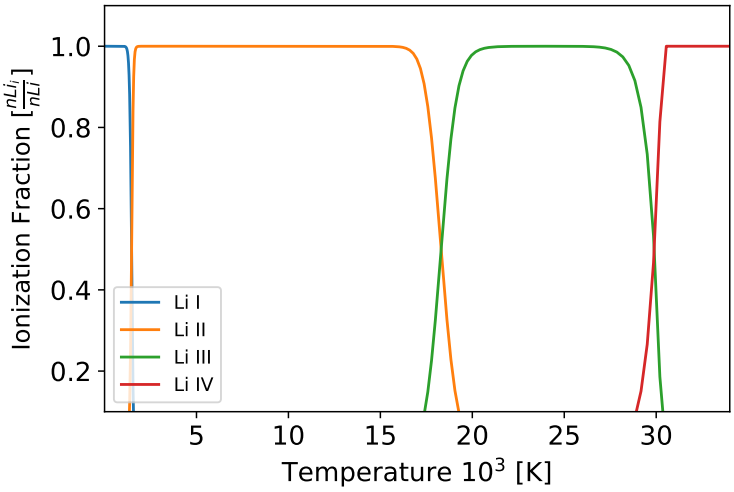

Figure 2.5: Normalized density of states of ionization of Lithium, Li, as a function of the temperature, from ground state Lithium, Li I, to Lithium three times ionized, Li IV.

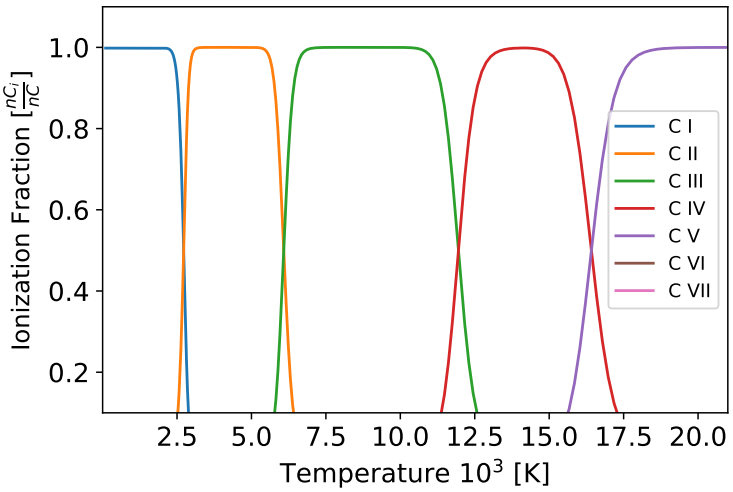

Figure 2.6: Normalized density of states of ionization of Carbon, C, as function of the temperature, from ground state Carbon, C I, to carbon six times ionized, C VII.

2.2.3 Cooling

We consider the cooling of a photoionized and collisional plasma. At high temperatures, or in a fully ionized gas, the cooling process is dominated by collisionally excited lines of ionized elements and free-free emission. At intermediate temperatures, or in a medium not completely ionized, cooling is due to bound-free and collisionally excited lines of neutral elements.

The computation takes into account the specific cooling for the 30 lightest elements and it is based on Lykins et al. 2013, which is the most recent work on cooling for the code *CLOUDY* (Ferland et al. 2017). The Tables with all data can be seen in Lykins et al. 2013.

In Figure 2.7 we can see that the work is in agreement with other cooling fit models.

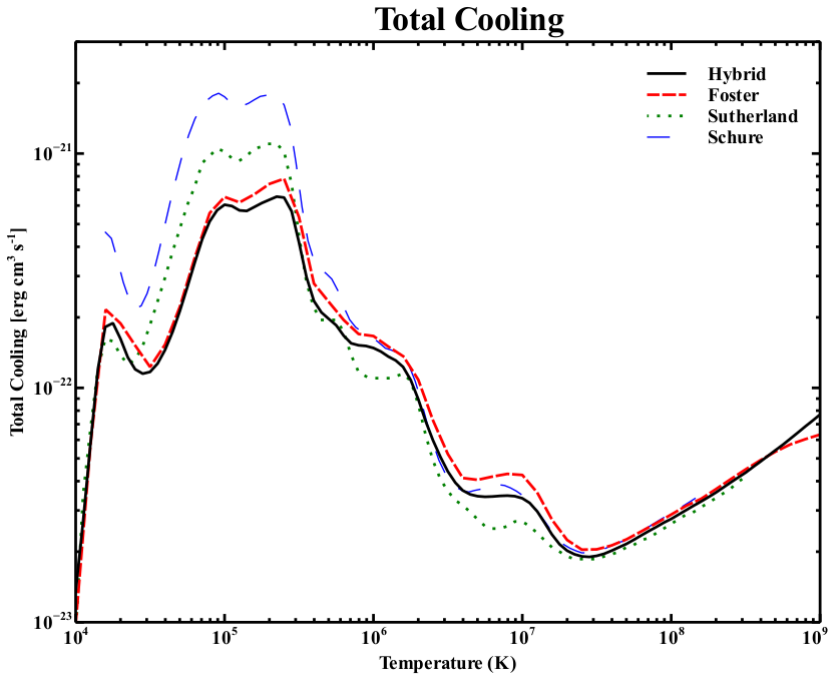

Figure 2.7: Comparison between different cooling models for solar metallicity as function of temperature (Lykins et al. 2013).

Using the data from Lykins et al. 2013 we created a code that computes the cooling as a function of the metallicity of the gas, Z. We plot in figure 2.8 the specific cooling for different values of Z (solar metallicity corresponds to Z = 0.01).

In Figures 2.9, 2.10 and 2.11 we show the specific cooling as a function of temperature for three different elements: Carbon (C), Oxygen (O) and Iron (Fe) and for three different

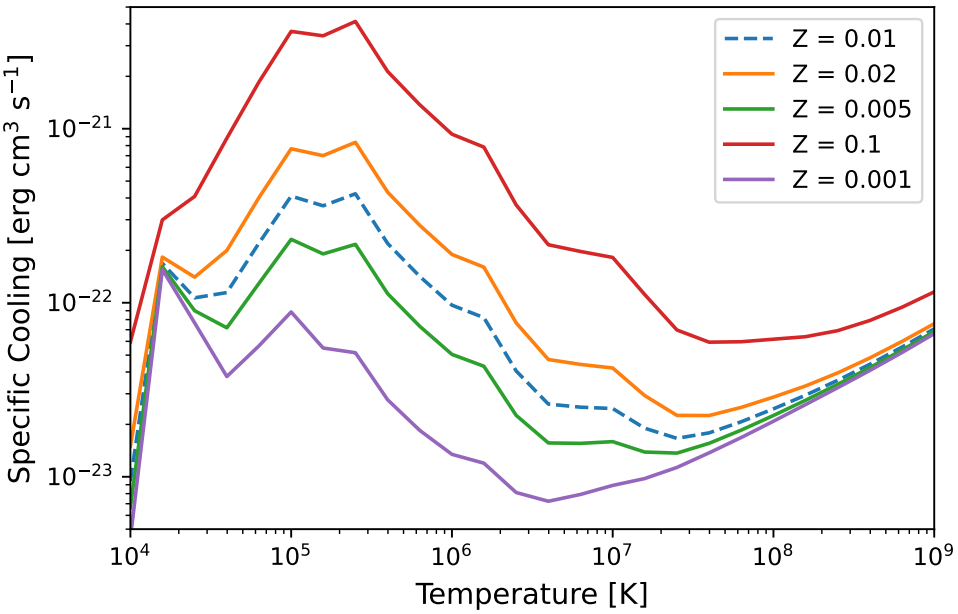

Figure 2.8: Here we present the result of our code. The figure shows the specific cooling for different metallicities using the data from Lykins et al. 2013. The dashed line represents solar metallicity.

metallicities: solar metallicity, $Z = Z_\odot = 0.01$, half solar metallicity, $Z_\odot/2$ and two times solar metallicity, $2Z_\odot$. As metallicity decreases it is possible to observe a proportional decrease in the specific cooling for all three elements.

2.2.4 Hα emission

In order to compute the Hα emission we consider the contribution from collisional excitation (Giovanardi and Palla 1989) and radiative recombination (Aller 1984). The Hα emission is obtained as a function of neutral and total densities and the local temperature of the gas.

The emission used is the same used by De Colle and Raga 2006,

$$H\alpha = n_e(E_{\rm rec} + E_{\rm coll}) \tag{2.47}$$

where n_e is the electron density, and

$$E_{\rm rec} = \frac{4.161 \times 10^{-25} n_{HII}}{10^{0.0424/T_4} \times T_4^{0.983}}, \tag{2.48}$$

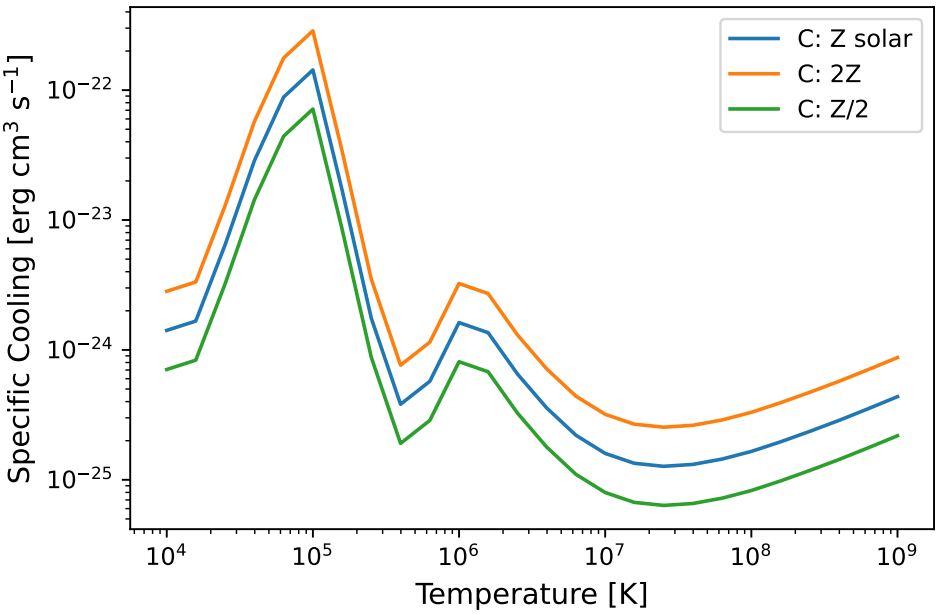

Figure 2.9: Our computed specific cooling of Carbon, C, as a function of temperature for three different metallicities. Solar metallicity, Z = 0.01, half solar metallicity, Z/2, and the double of solar metallicity, 2Z.

considering $T_4 = T \times 10^{-4}$, where T is the gas temperature, and $E_{\rm coll}$

$$E_{\rm coll} = 0.4 \times n_{H_I} \times 3.028 \times 10^{-12} \times 0.0858 \times \frac{8.628 \times 10^{-6} \Omega^{-140336/T}}{2T^{1/2}}, \tag{2.49}$$

being n_{HI} the density of ionized hydrogen and Ω defined as

$$\Omega = 0.1934 + T\left[-4.698 \times 10^{-7} + T\left(8.352 \times 10^{-11} - 5.576 \times 10^{-16} T\right)\right]. \tag{2.50}$$

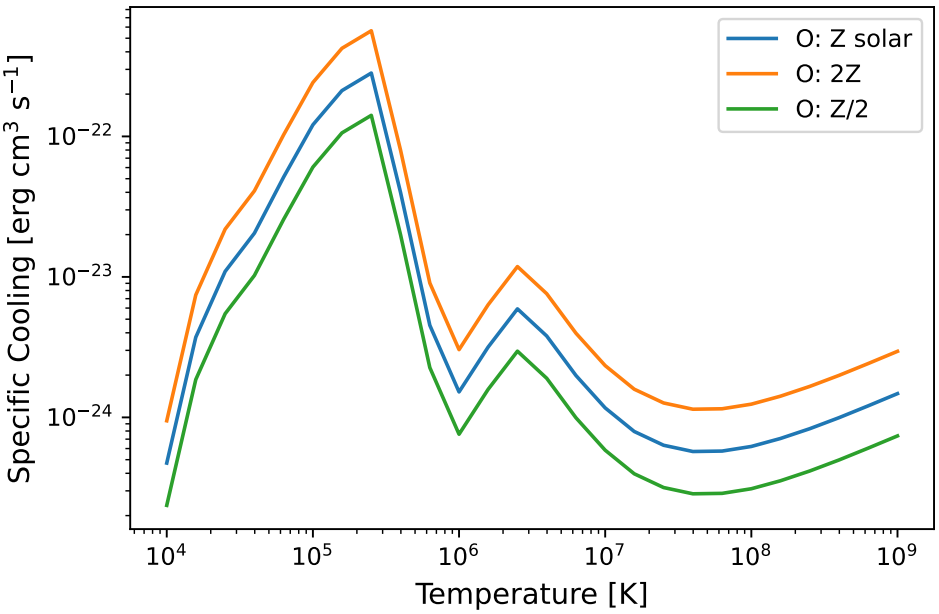

Figure 2.10: Specific cooling of Oxygen, O, as a function of temperature for three different metallicities. Solar metallicity, Z = 0.01, half solar metallicity, Z/2, and the double of solar metallicity, 2Z.

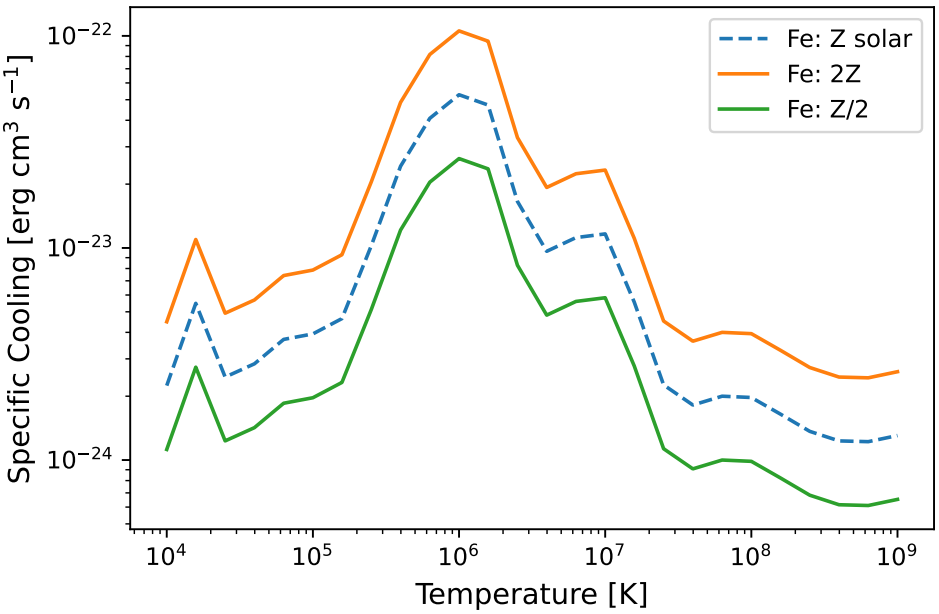

Figure 2.11: Specific cooling of Iron, Fe, as a function of temperature for three different metallicities. Solar metallicity, Z = 0.01, half solar metallicity, Z/2, and the double of solar metallicity, 2Z.

2.3 Genetic Algorithm

As part of this thesis, we created an algorithm to model the complex structure of CSM in interacting SNe. As mentioned before, interacting SNe might have a dense and complex CSM. We applied this algorithm in the SN 2014C in order to fit the 11 observed epochs of emission, creating 11 regions with different densities. The algorithm created couples a Genetic Algorithm with the hydrodynamic code *Mezcal* and a radiation transfer code as post-processing, iteratively modifying the density in this 11 different regions.

Genetic Algorithms (GA) are based on the theory of natural selection. GA are commonly used optimization methods employed also in astrophysics to solve problems with many degrees of freedom, in which finding the optimal solution would be very hard otherwise. We employ GA but the results obtained are independent of the particular optimization method chosen. Nevertheless, this is the first time, as far as we know, that optimization methods are coupled directly to hydrodynamical simulations.

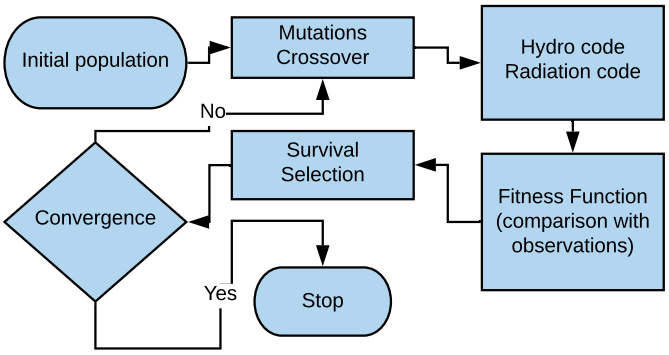

Figure 2.12: Flowchart showing the Genetic Algorithm employed to determine the density stratification of the massive shell interacting with the SN 2014C.

Figure 2.12 shows schematically the GA we implement. A population formed by 10 elements (the "chromosomes" in the GA terminology) is chosen at the beginning of the iterative process. Each element of the population is defined by setting 11 values of the density at different radii inside the shell (the "genes"). At each step, we create 90 new elements of the population. Half of them are defined by randomly choosing two elements of the original population and applying to them cross-over and mutation, while the other half is initialized by directly copying the density values from one random element of the population and modifying it only by mutation.

In the cross-over process, the two "parents" are mixed by choosing randomly a certain

number of densities from each element (e.g., the first and second densities from the first element, the third density from the second element, and so on). This process is inspired by the genetic mixing present in biological evolution. In the mutation process, we modify randomly one density in each element. We do so by setting a Gaussian distribution around the original value of the density ρ_0, with a width given, in 90% of the cases, by $\rho_0/2$, and in 10% of the cases by $10\rho_0$, so that in a few cases the system explores density values far away from the initial one (to avoid being trapped by a local minimum).

The shell densities are then mapped as initial conditions into the HD code. Then, after the simulation is completed, the RT code is computed by post-processing taking as input the results of the HD calculation. A fitness function (a reduced χ^2 test) is applied to compare the synthetic spectra produced by the model and observational data. The fittest 10 elements (out of the new 90 and the old 10 elements of the population) are saved and used as the initial condition for a new loop. This process is repeated for ~ 100 iterations so then a total number of $\sim 10^4$ simulations is done. Each simulation takes ~ 10 minutes in a 1D system so that the entire process can be completed in less than a day.

In practice, the simulations are done by using the "Message Passing Interface" library. At each iteration, the master node initialized and synchronized the simulations, selected the best elements, and managed the cross-over/mutation processes, while the other nodes run (in parallel) each of the 90 hydrodynamics simulations, compute the X-ray spectra and the fitness function.

Chapter 3

Survival of the Fittest: Numerical Modeling of SN 2014C

This chapter presents a study of the SN 2014C, published as (Vargas et al. 2022): "Survival of the Fittest: Numerical Modeling of SN 2014C", by Felipe Vargas, Fabio De Colle, Daniel Brethauer, Raffaella Margutti, and Cristian G. Bernal, The Astrophysical Journal, 930, 150 (2022)

3.1 Abstract

Initially classified as a supernova type Ib, $\sim$ 100 days after the explosion SN 2014C made a transition to a SN type II, presenting a gradual increase in the Hα emission. This has been interpreted as evidence of interaction between the supernova shock wave and a massive shell previously ejected from the progenitor star. In this paper, we present numerical simulations of the propagation of the SN shock through the progenitor star and its wind, as well as the interaction of the SN ejecta with the massive shell. To determine with high precision the structure and location of the shell, we couple a genetic algorithm to a hydrodynamic and a bremsstrahlung radiation transfer code. We iteratively modify the density stratification and location of the shell by minimizing the variance between X-ray observations and synthetic predictions computed from the numerical model, allowing the shell structure to be completely arbitrary. By assuming spherical symmetry, we found that our best-fit model has a shell mass of 2.6 $M_\odot$, extends from 1.6 $\times 10^{16}$ cm to 1.87×10^{17} cm, implying that it was ejected $\sim 60/(v_w/100\ \mathrm{km\ s^{-1}})$ yrs before the SN explosion, and has a density stratification with an

average behavior $\sim r^{-3}$ but presenting density fluctuations larger than one order of magnitude. Finally, we predict that, if the density stratification follows the same power-law behaviour, the SN will break out from the shell by mid 2022, i.e. 8.5 years after explosion.
Supernovae - Stellar mass loss - Circumstellar shells - Astronomy data modeling - Stellar-interstellar interactions

3.2 Introduction

While mass loss is one of the key mechanisms regulating the evolution of massive stars, a complete understanding of it is still missing, specially during the final phases before the supernova (SN) explosion (Smith 2014). The mass loss history $\lesssim 100 - 1000$ yrs before core-collapse supernova explosions can be inferred from the radio and X-ray emission resulting from the propagation of the SN shock through the circumstellar material (for a review see, e.g., Chevalier, Fransson, and Nymark 2017). While the bulk of the SN ejecta emits in optical, the shock heated gas resulting from the interaction with the environment might be observed in X-ray and radio due to bremsstrahlung and synchrotron radiation from relativistic electrons accelerated at the shock front.

The forward shock of type Ib/c SNe, originated from pre-supernova stars with high mass loss before collapse, interacts with the wind of the progenitor star, which has typical mass loss rates of $\dot{M}_w \sim 10^{-4} - 10^{-6}$ $M_\odot$ yr^{-1}. The wind is often not smooth, as proven by radio emission, showing small flux fluctuations of $\sim$ a few over timescales of tens-hundreds of days after the explosion (Bietenholz and Bartel 2005; Soderberg et al. 2006; Schinzel et al. 2009b; Wellons, Soderberg, and Chevalier 2012; Salas et al. 2013; Bietenholz, De Colle, et al. 2014; Corsi et al. 2014; Palliyaguru et al. 2021).

In a few cases, type Ib/c SNe show signs of much stronger interaction between the ejecta and shells of material ejected before the explosion. For instance, SN 2006jc exploded inside a dense He rich environment (Foley et al. 2007), likely produced by an outburst ejected $\sim$ two years before the SN event. As well SN 2001em, initially classified as type Ib SN, presented prominent Hα emission lines at 2.5 yrs. Associated with strong radio and X-ray emission, this was interpreted as evidence of the interaction between the SN ejecta and a massive (~ 3 $M_\odot$) hydrogen-rich shell located at $\sim 7 \times 10^{16}$ cm from the progenitor iron core (Chugai and Chevalier 2006; Chandra et al. 2022). Several other SNe show similar signs of early interaction with massive shells (Anupama et al. 2005; Moriya and Maeda 2014; Chen et al. 2018; Pooley, Wheeler, et al. 2019; Dwarkadas, Dewey, and Bauer 2010; Ben-Ami et al. 2014;

Mauerhan, Filippenko, et al. 2018; Suzuki et al. 2021.) Nevertheless, while in all these cases the intermediate phases of the transition between type Ib and type IIn SN were not observed, this transition has been observed in detail in the SN 2014C.

Discovered by the *Lick Observatory Supernova Search* (LOSS) (Kim et al. 2014) in the NGC 7331 galaxy at a distance of 14.7 Mpc and initially classified as a type Ib SN, SN 2014C made a transition to a type IIn SN about ~ 100 days after the explosion, showing strong Hα emission (Milisavljevic, Margutti, et al. 2015). The modelling of the optical/UV light curve shows that SN 2014C has a kinetic energy of $1.75 \pm 0.25 \times 10^{51}$ erg, with an ejecta mass of 1.7 ± 0.2 M$_\odot$ and a Nickel mass of 0.15 ± 0.02 M$_\odot$ (Margutti, Kamble, et al. 2017).

SN 2014C has also been extensively observed with X-rays Telescope (XRT, Burrows et al. 2005) on board the *Neil Gehrels Swift Observatory (XRT)* (Gehrels et al. 2004) and the *Chandra X-ray Observatory (CXO)* in the 0.3-10 keV energy band, and by the *Nuclear Spectroscopic Telescope Array (NuSTAR)* from 3 keV to 79 keV (Margutti, Kamble, et al. 2017; Brethauer, Margutti, Milisavljevic, and Bietenholz 2020; Brethauer, Margutti, Milisavljevic, Bietenholz, et al. 2022). Most of the detected X-ray emission is concentrated in the 1-40 keV energy band, while emission below ~ 1 keV is strongly absorbed.

The observed X-ray emission increased at 250 days, although the lack of temporal coverage between 100 and 250 days implies that likely the onset of the X-ray increase was at a smaller time. Integrated over the spectral range 0.3-100 keV, it raised from 5×10^{39} erg s^{-1} to 5×10^{40} erg s^{-1}. Then, it peaked $\sim 850-1000$ days and maintained a nearly constant flux until ~ 2000 days after the explosion (Brethauer, Margutti, Milisavljevic, and Bietenholz 2020).

Radio observations showed a similar behaviour. Light curves of the SN at 15.7 GHz taken with the *Arcminute Microkelvin Imager* (AMI) between 16 and 567 days showed that the flux increased rapidly at $\sim$ 100-150 days (Anderson et al. 2017). A similar increase (by more than one order of magnitude) was observed by the *Very Large array* (VLA) Margutti, Kamble, et al. 2017. Furthermore, observations done by using the *Very Long Baseline Interferometry* (VLBI) found that the shock expansion has already strongly decelerated 384 days after the explosion (Bietenholz, Kamble, et al. 2018; Bietenholz, Bartel, et al. 2021).

The evolution of radio, optical and X-ray emission have been interpreted by considering the interaction of the SN ejecta with a low density steady wind with $\dot{M}_w = 5 \times 10^{-5}$ M$_\odot$ yr^{-1} (assuming a wind velocity $v_w = 1000$ km s^{-1} - see Anderson et al. 2017; Margutti, Kamble, et al. 2017), and a higher density, extended circumstellar medium (CSM). Although most previous studies agree on the position of the denser shell (e.g. $R_{\rm shell} \sim 5 - 6 \times 10^{16}$ cm from the progenitor iron core, Anderson et al. 2017; Margutti, Kamble, et al. 2017;

Milisavljevic, Margutti, et al. 2015; Tinyanont et al. 2019; Sun, Maund, and Crowther 2020), different models have been proposed with respect to the shell thickness, mass and structure. Consistently with the fact that the interaction lasts several years, (Bietenholz, Bartel, et al. 2021; Bietenholz, Kamble, et al. 2018; Margutti, Kamble, et al. 2017; Milisavljevic, Margutti, et al. 2015) interpreted the data as evidence of the interaction between the SN shock and a thick and massive shell with a size $\Delta R_{\rm shell} \sim R_{\rm shell}$ and a mass $M_{\rm shell} \sim 3.00$ M$_\odot$. On the other hand, Harris and Nugent 2020 considers a progenitor with a lower mass-loss rate, which formed a "*wall*" at $R_w \sim 10^{16}$ cm and resulted in a thin shell with size $\Delta R_w \lesssim 0.25 R_w$, corresponding to a lower mass, $M_w = 0.04 - 0.31$ M$_\odot$. A similar structure, with a thin high-density shell and an extended outer medium is also inferred by (Tinyanont et al. 2019).

In order to explain the presence of a dense CSM around the progenitor of SN 2014C, two possible scenarios have been suggested. In the first scenario, it is assumed that the progenitor of SN 2014C was a star with a steady mass-loss rate, resulting in a stratified, low density environment with a density $\rho \propto \dot{M}_w r^{-2}$ (Anderson et al. 2017; Bietenholz, Bartel, et al. 2021; Bietenholz, Kamble, et al. 2018; Harris and Nugent 2020; Margutti, Kamble, et al. 2017). In this scenario, the mass-loss rate had an abrupt increase $\sim$ tens-hundreds of years before the explosion (with $\dot{M}_w \sim 10^{-3} - 10^{-2}$ M$_\odot$ yr^{-1} assuming an wind velocity $v_w \sim 100$ km s^{-1}) creating a spherically symmetric expanding high density CSM (with a density $\sim 10^6$ cm^{-3}). Sun, Maund, and Crowther 2020 depicted a different scenario, in which the dense CSM results from an 11 M$_\odot$ star stripped of its outer envelope by binary interaction.

In synthesis, in addition to the progenitor star, the structure, extension and mass of the environment leading to the X-ray emission has been extensively debated. Clarifying the structure of the dense CSM leading to the X-ray emission, i.e. its density profile and total mass, is the main aim of this paper.

Radio and X-ray emission from the SN shock are typically described by considering a self-similar behaviour for the dynamics (Chevalier 1982b; Chevalier and Liang 1989; Chevalier 1998). In the case of a supernova interacting with a massive shell, we can not assume a self-similar behaviour for the flow as the interaction with the shell leads to the formation of a strong reverse shock. Then, although an analytical description gives a qualitative picture of the problem, a detailed understanding of the dynamics can be achieved only employing numerical simulations.

Typically, running a large number of models covering a predefined number of parameters provides sufficient detail of the dynamics. When running computational intensive hydrodynamical simulations, however, this approach necessarily limits the parameter space explored.

To handle this limitation, in this paper we use an optimization method (a genetic algorithm) to iteratively determine a relatively large number of parameters by running a limited number of numerical simulations. Although there have been a wide range of applications of genetic algorithms in astrophysics (Charbonneau 1995), it is the first time that this method has been applied by coupling hydrodynamic simulations with radiative transfer, in order to obtain an optimized solution for the CSM density profiles.

Specifically, we run a set of numerical simulations coupled to a Genetic Algorithm (GA). The GA iteratively adapts the values of the shell density by minimizing the difference between the synthetic X-ray emission (computed by post-processing the results of the hydrodynamical simulations) and observations of this SN presented in (Margutti, Kamble, et al. 2017; Brethauer, Margutti, Milisavljevic, and Bietenholz 2020; Brethauer, Margutti, Milisavljevic, Bietenholz, et al. 2022). In this approach, the physical space is divided in several parts (according to the epochs of observations) and each part has a density $\rho(r_i)$ (being $i = 1, \ldots, N$) that is considered a parameter of the model.

The paper is organized as follows: in Section 2 we describe the hydrodynamics code and the initial conditions of the simulations, the bremsstrahlung radiation transfer code and the genetic algorithm employed to solve the optimization problem and to find the density stratification of the shell. In Section 3 we present the results of our numerical calculations. In Section 4 we discuss the limits of the simulations presented, and the implications of our findings. Finally, in Section 5 we draw our conclusions.

3.3 Methods

3.3.1 Numerical codes and initial conditions

We study the interaction of a SN shock with a massive shell by running a set of one-dimensional (1D), spherically symmetric simulations with the Adaptive Mesh Refinement (AMR) code *Mezcal* (De Colle, Granot, et al. 2012). The code solves the special relativistic hydrodynamics equations, and has been extensively used to run numerical simulations of astrophysical flows (González-Casanova et al. 2014; De Colle, Raga, et al. 2014; De Colle, Kumar, and Aguilera-Dena 2018a; De Colle, Kumar, and Aguilera-Dena 2018b).

We follow the propagation of the SN shock front as it moves through a computational grid covering $\sim$ nine orders of magnitude in space, from $\sim 2 \times 10^8$ cm (the outer edge of the iron core) to $\sim 2 \times 10^{17}$ cm. We do so by running two sets of simulations. First, we follow the

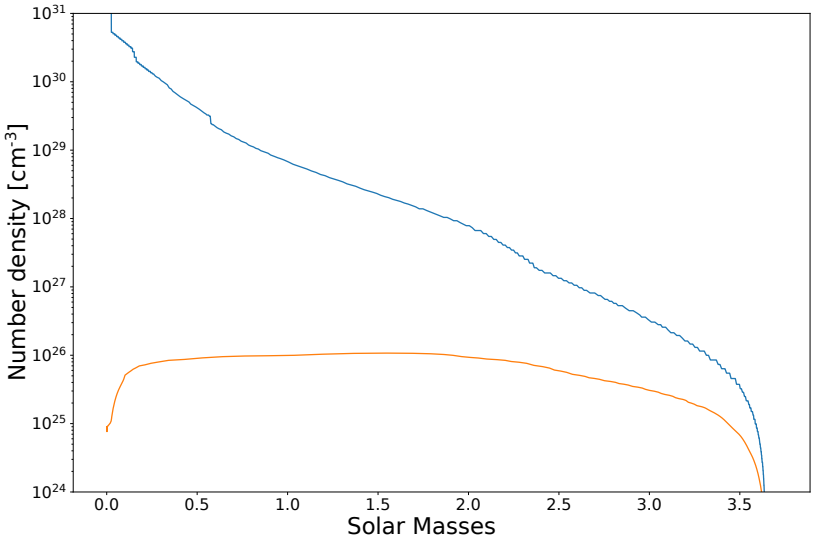

Figure 3.1: Progenitor pre-explosion density profile (blue line) and ejecta density profile (orange line, at 50 s) in mass coordinates. As the computational box extends from 2.2×10^8 cm, the figure does not include the mass of the iron core (corresponding to about 1.8 $M_\odot$)

.

propagation of the SN shock front as it moves through the progenitor star, e.g., from $\sim 10^8$ cm to 10^{11} cm. Then, after remapping the results of the small scale simulation into a much larger computational box, we follow its propagation through the wind of the progenitor star and its interaction with the massive shell located at $\gtrsim 10^{16}$ cm.

We set the density profile of the progenitor star by using the E25 pre-supernova model from Heger, Langer, and Woosley 2000. This corresponds to a star which has lost its outer envelope. The resulting star has a mass of 5.45 $M_\odot$ and a radius of $\sim 3 \times 10^{10}$ cm.

The computational grid extends radially from 2.2×10^8 cm to 6.6×10^{11} cm. We employ 20 cells at the coarsest level of refinement, with 22 levels of refinement, corresponding to a resolution of 1.6×10^4 cm. We set reflecting boundary conditions at the inner boundary and outflow boundary conditions at the outer boundary of the computational box. The SN energy ($E_{\rm SN} \approx 10^{51}$ erg) is imposed by setting the pressure of the two inner cells of the computational box as $p = E_{\rm SN}(\Gamma_{\rm ad} - 1)/V$, being $\Gamma_{\rm ad}$ the adiabatic index and V the volume of the two cells. We employ a variable adabiatic index $\Gamma_{\rm ad}$, bridging between the relativistic $\Gamma_{\rm ad} = 4/3$ and the newtonian $\Gamma_{\rm ad} = 5/3$ cases (see Section 2.4 of De Colle, Granot, et al. 2012).

Figure 3.1 shows the initial density stratification of the star and of the ejecta at 50 s. The SN energy has been chosen to match the one derived by Margutti, Kamble, et al. 2017, while

the ejecta mass is larger (3.5 $M_\odot$ in our simulations vs. 1.7 ± 0.2 inferred by Margutti, Kamble, et al. 2017). Anyway, we notice that: 1) the mass inferred depends strongly on the (uncertain) opacity coefficient κ (Maund 2018); and 2) as we set a reflective boundary condition at the inner boundary, our simulations do not include fallback which could decrease the ejecta mass.

Outside the stellar surface, we take $\rho = \dot{M}_w/(4\pi r^2 v_w)$, being $\dot{M}_w = 5 \times 10^{-6}$ $M_\odot$ yr^{-1} and $v_w = 10^8$ cm s^{-1} the mass loss rate and velocity of the wind launched by the star before the collapse. As the velocity of the SN shock front is about two orders of magnitude larger than the stellar wind (i.e., $\sim 10^{10}$ cm s^{-1} vs. $\sim 10^8$ cm s^{-1}), we assume that the wind medium is static. The propagation of the SN shock front is followed as it breaks out of the progenitor star and arrives to 4.5×10^{11} cm in 50 seconds.

In the large scale simulations, the computational box goes from 10^{10} cm to 5×10^{17} cm. For $r < 4.5 \times 10^{11}$ cm we set the density, pressure and velocity by using the values determined from the small scale simulation. We save outputs each ~ 20 simulated days, and at the times corresponding to the available observational epochs. For larger radii, we take the density stratification as $\rho = \dot{M}_w/(4\pi r^2 v_w)$, with $\dot{M}_w = 5 \times 10^{-6}$ and $v_w = 10^8$ cm s^{-1} as in the small scale simulation. We employ 150 cells, with 20 levels of refinement in the AMR grid, corresponding to a resolution of 2.5×10^9 cm. By running different simulations in which we change the number of levels of refinement between 14 and 22 levels, we verify that 20 levels of refinement are enough to achieve convergence.

3.3.2 Bremsstrahlung Emission Code

To compare models with observations, we compute the X-ray bremsstrahlung emission coming from the shocked plasma by post-processing the results of the hydrodynamical simulations. We assume that the shocked material is completely ionized* so that it does not contribute to the bound-free opacity and that the unshocked shell is neutral. Extending the radio synchrotron emission to X-rays by assuming $F_\nu \propto \nu^{-(p-1)/2} \propto \nu^{-1}$ with $p \sim 3$, Margutti, Kamble, et al. 2017 showed that the contribution of synchrotron emission to the X-ray flux is negligible (~ 2 orders of magnitude smaller than the observed values), suggesting a thermal origin for the X-rays.

*This assumption is justified by the large post-shock temperature and the presence of strong photo-ionizing X-ray and UV emission.

The specific flux is given by

$$F_\nu = \int I_\nu \cos\theta d\Omega \ , \tag{3.1}$$

where $d\Omega = 2\pi \sin\theta d\theta / D^2$, being $D = 14.7$ Mpc the luminosity distance from the SN 2014C Freedman et al. 2001, and I_ν is the specific intensity.

The observed X-rays radiation is due to thermal bremsstrahlung emission caused by the interaction between the SN shock and a massive shell (Margutti, Kamble, et al. 2017). To determine the specific intensity, we solve the radiation transfer equation

$$\frac{dI_\nu}{d\tau_\nu} = S_\nu - I_\nu \ , \tag{3.2}$$

where $S_\nu = j_\nu/\alpha_\nu$ is the source function, $\tau_\nu = \int \alpha_\nu dl$ is the optical depth, and j_ν and α_ν are the emissivity and the absorption coefficient respectively. The radiation transfer equation is solved by a standard approach (Bodenheimer et al. 2006). Shortly, we created a two-dimensional grid in cylindrical coordinates. We mapped the results of our 1d simulations on this grid, and integrate along 200 rays. We compute the intensity in the plane of the sky, which integration leads to the flux (see equation 3.1).

In addition to the bremsstrahlung (free-free) self-absorption, we also consider bound-free absorption, which at early times dominates absorption for frequencies $\lesssim 10^{18}$ Hz, so that

$$\alpha_\nu = \alpha_{\nu,\mathrm{ff}} + \alpha_{\nu,\mathrm{bf}} \ , \qquad j_\nu = j_{\nu,\mathrm{ff}} \ . \tag{3.3}$$

To compute the bound-free absorption, we use tabulated cross-sections for solar metallicity (Morrison and McCammon 1983). For the bremsstrahlung coefficients we take (Rybicki and Lightman 1986)

$$j_\nu = \frac{6.8}{4\pi} \times 10^{-38} Z^2 n_e n_i T^{-1/2} e^{-\frac{h\nu}{kT}} G \tag{3.4}$$

$$\alpha_\nu = 3.7 \times 10^8 T^{-1/2} \frac{Z^2 n_e n_i}{\nu^3} \left(1 - e^{-\frac{h\nu}{kT}}\right) G \ , \tag{3.5}$$

where Z, n_e and n_i are the atomic number, electron and ion densities respectively, and G is the Gaunt Factor (~ 1 for the range of parameters considered here). All other variables have their usual meaning and everything is in cgs units. The electron/ion densities and the temperature are directly determined from the numerical simulations by assuming that the ejecta is an ideal gas with solar metallicity. We also assume that electrons and ions have the same temperature. Cooling is not included in the numerical simulations as the bremsstrahlung cooling timescale is $t_{\mathrm{ff}} = 60(T/10^8\,\mathrm{K})(n_e/10^6 \mathrm{cm}^{-3})$ yrs, so it is much larger than the timescales studied here.

3.3.3 Computing the shell parameters from a grid of models

As a first attempt to reproduce the observed X-ray emission, we have first considered a massive, uniform cold shell located at the radius R_s, with mass M_s and thickness ΔR_s. To determine the best values for these three parameters, we run a grid of 1815 models by using 11 values of M_s (in the range 1.5 $M_\odot$ to 2.5 $M_\odot$), 15 values of ΔR_s (ranging from 7.5×10^{14} up to 2.5×10^{15} cm), and 11 values of R_s (from 1.8×10^{16} to 7.8×10^{16} cm). To compare the results of the numerical simulations with observations, we have then employed the ray-tracing code described in Section 3.3.2.

Unfortunately, none of the models provided a reasonable fit of the data. In particular, shells with larger density (i.e., larger mass and smaller thickness) reproduce well the early observational epochs, while shells with smaller densities (i.e. smaller mass and thicker) reproduced well the late observational epochs. This indicates that the shell density is not constant, and has a decreasing density from smaller to larger radii.

We notice that, as the origin of the massive shell is not understood, it could in principle have an arbitrary shape. In this case, to find the density at several radii is a task that is not possible to achieve with a grid of numerical models. For instance, a grid of ten values for the density at 10 different radii implies running 10^{10} simulations. Thus, to determine the density stratification of the shell, we decided to solve the "full" optimization problem. This is done by coupling the *Mezcal* code with other two codes: a radiation transfer code which computes the bremsstrahlung radiation (see Section 3.3.2), and a genetic algorithm (described in Section 3.3.4) that automatically and randomly changes the density profile inside the shell by minimizing the variance between the synthetic observations computed from the numerical model and the X-ray observations, allowing the density profile to be completely arbitrary.

3.3.4 Genetic Algorithm

Genetic algorithms, GA hereafter. Rajpaul 2012 are based on the theory of natural selection. GA are commonly used optimization methods[†], employed also in astrophysics to solve problems with many degrees of freedom, in which finding the optimal solution would be very hard otherwise (Canto, Curiel, and Martinez-Gomez 2009; De Geyter et al. 2013; Morisset 2016). Nevertheless, this is the first time, as far as we know, that optimization methods are coupled

[†]We have employed GA in this paper but the results obtained are independent on the particular optimization method chosen.

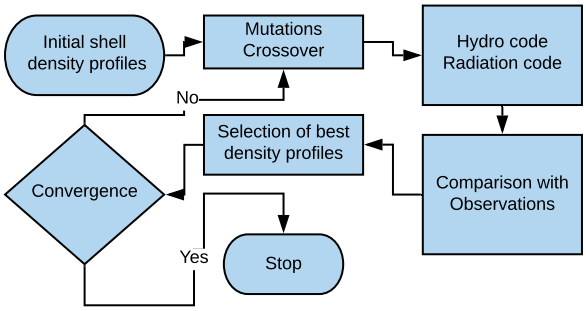

Figure 3.2: Flowchart showing the genetic algorithm employed to determine the density stratification of the massive shell interacting with the SN 2014C. First, we initialize a a set of shell density profiles. We modify the initial densities by mutations and cross-over (see the text for details). We run hydrodynamical simulations following the interaction of the SN ejecta with the shell and we compute synthetic X-ray spectra which are compared with the observations. We select the "best" simulations using a "fitness function" (the χ^2 test). The process is repeated until convergence.

directly to hydrodynamical simulations.

We run a single small scale simulation following the propagation of the shock wave in the interior of the star. Then, we use the SN ejecta structure given by this simulation to initialize large scale numerical simulations. The GA (see Figure 3.2 for a schematic description of the algorithm) is then used to find the best density stratification of the shell by running several simulations of the interaction of the SN ejecta with the massive shell.

The initial conditions of the large scale simulations are described in Section 2.1. The shell structure is initialized in the numerical simulations by a power-law interpolation of the densities $\rho(r_i)$ (with $i = 1, \ldots, 11$) defined at 11 radial position r_i. Nine of the radii r_i are determined directly from the numerical simulations and are given by the location of the shock at the nine available observational epochs. Additionally, we define two densities, one at a smaller (r_1) and one at a larger radius (r_{11}). While the value of $r_1 = r_2/2$ is fixed, r_{11} is allowed to vary to get the necessary absorption.

Thus, the 11 values of density (and the corresponding 11 radial positions) represent the parameters of the optimization process. We do not impose any constrain on the value of the densities. At the beginning of the iterative process, 10 constant density shell structures are defined, with equally spaced values (defined in log space) between $n = 10^2$ cm^{-3} and

$n = 10^8$ cm^{-3} and located at a radius $r_i = 2 \times 10^{16} - 4 \times 10^{16}$ cm. This choice of the initial parameters is completely arbitrary. Indeed, as usual in optimization methods, the final results are independent on the initial choice of the parameters.

Then, we create 90 new shell structures. Half of the densities $\rho(r_i)$ are defined by randomly choosing two shell structures from the initial set and applying to them cross-over and mutation (see below), while the other half is initialized by directly copying the density values from one random shell structure and modifying it only by mutation. In GA, the fraction of the parameters which should change due to mutation and cross-over depends on the particular problem studied. Empirically, we found that, for the optimization problem discussed in this paper, setting equal probability for the cross-over and mutation processes was producing reasonably fast results. Anyway, we did not attempt to find the fraction of mutations/cross-over which reduces the number of iterations to a minimum. Optimizing it, and replacing the GA with more efficient optimization methods could reduce substantially the final computational time.

In the cross-over process, two values of density taken from a previous iterative step are mixed by choosing randomly values of densities from each shell structure (e.g., the first and second densities from the first density profile, the third density from the second profile and so on). This process is inspired by the genetic mixing present in biological evolution. In the mutation process we modify randomly one density in each profile. We do so by setting a Gaussian distribution around the original value of the density ρ_0, with a width given, in 90% of the cases, by $\rho_i/2$, and in 10% of the cases by $10\rho_0$, so that in a few cases the system explores density values far away from the initial one (to avoid being trapped by a local minimum).

The shell densities are then mapped as initial conditions into the *Mezcal* code in each step. Then, after each simulation is completed, the bremsstrahlung X-ray emission is computed by post-processing the results. A fitness function (a reduced χ^2 test) is applied to compare the synthetic spectra produced by the model and the observational data at 9 epochs: 308, 396, 477, 606, 857, 1029, 1257, 1574 and 1971 days after explosion. The fittest 10 simulations (out of the new 90 and the old 10 set of simulations) are then used as initial condition for a new step.

This process converged in ~ 150 iterations, for a total number of $\sim 10^4$ simulations, then reducing the number of simulation by a factor of 10^6 with respect to a grid of simulations covering a similar number of parameters. Each simulation took ~ 10 minutes so that the entire process could be completed in less than a day.

The simulations were done on a cluster of CPUs, by using the "Message Passing Interface"

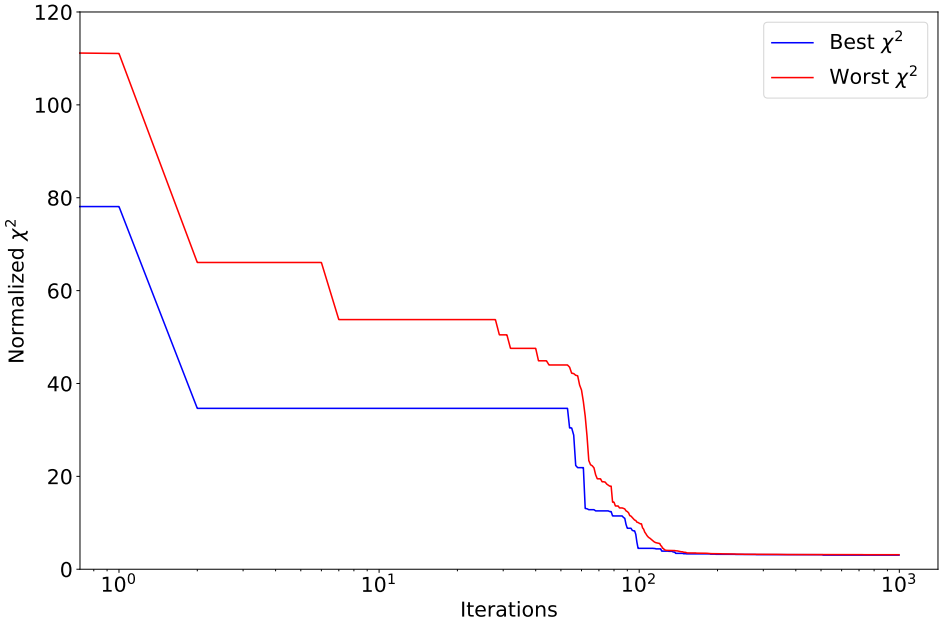

Figure 3.3: Normalized χ^2 for the best and worst model among the fittest 10 simulations, shown as function of the iteration number. After $\sim$ 150 iterations the system converges to the optimal solution, corresponding to a normalized $\chi^2 \approx 3.03$.

library. At each iteration, the master node initialized and synchronised the simulations, selected the best simulations/shell structures and managed the cross-over/mutation processes, while the other nodes run (in parallel) each of the 90 hydrodynamics simulation, compute the X-ray spectra and the fitness function (a χ^2 test).

Figure 3.3 shows the evolution of the fitness function (the normalized χ^2) for the best and worst simulation (among the 10 fittest simulations) during each iteration step. The solution reaches a minimum of $\chi^2 \approx 3.03$. The evolution of the density profile of the massive shell as function of radius and iteration is shown in Figure 3.4. At the beginning of the iteration process, the solution fluctuates substantially between different iterations, to then converge to a final density profile (shown in blue in the figure). The density profile and the value of χ^2 are discussed in more detail below.

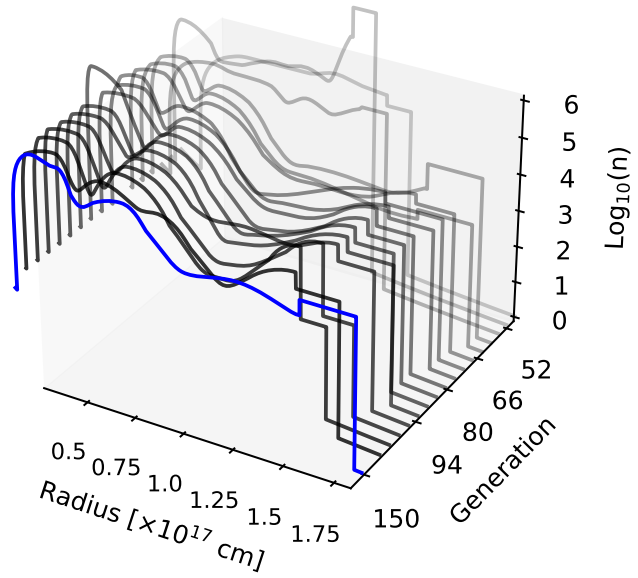

Figure 3.4: Evolution of the number density profiles (in units of cm^{-3}) of the outer shell during the iteration process (black lines, with increasing opacity from lower to larger iteration numbers). The final density profile is shown in blue.

3.4 Results

3.4.1 SN shock propagation through the progenitor wind

The propagation of the shock wave through the star has been extensively studied both for the non-relativistic (Sakurai 1960; Matzner and McKee 1999) and mildly relativistic regime (Tan, Matzner, and McKee 2001; Nakar and Sari 2010; Smith 2017b). As the shock approaches the surface of the progenitor star and it moves in the stellar envelope, in which the density drops steeper than $\rho \propto r^{-3}$, the shock velocity increases to mildly relativistic speeds.

As a result, once the SN shock breaks out in ~ 25 s, most of the mass (and energy) of the SN moves at velocities $\sim 10^4$ km s^{-1}, while a small fraction of the mass (corresponding to a kinetic energy $\approx 10^{47}$ ergs) expands with larger velocities (up to $v_{\rm sh} \sim 0.5$ c in our simulations). Self-similar solutions describing the propagation of the SN shock through a politropic envelope (with $\rho_{\rm env} \propto (R/r-1)^k$) predict an ejecta density stratification $\rho \propto r^{-n}$ after the break-out, with $n = 7-11$, depending on the structure of the progenitor star. We get a nearly constant density profile in the inner ejecta (containing most of the mass, see

figure 3.5), while the outer ejecta has a steep density profile, i.e. $\rho \sim r^{-10.3}$.

Then, we run a set of simulations by using as input the outcome of the small scale simulations, i.e., density, pressure and velocity profiles. As described in section 3.3.4, we compute the shell density profile that minimizes the variance between the bremsstrahlung emission computed from the numerical model and the observations. In the following, we discuss the evolution of the SN shock front while it propagates into the progenitor wind and interacts with the shell density profile obtained after the GA algorithm has converged.

Figure 3.5 shows the evolution of the ejecta before interacting with the outer shell. The expansion of the SN ejecta through the progenitor wind leads to the formation of a double shock structure, formed by the forward shock (FS), which accelerates and heats the WR wind, and the reverse shock (RS), which decelerates and heats the SN ejecta. Following Chevalier 1982b, the evolution of the forward and reverse shocks is self-similar, with $R \sim t^m$, where $m = (n-3)/(n-2)$. By taking $n = 10.3$, we get $m \sim 0.88$, which is consistent with the evolution of the shock wave obtained in our simulation.

In our simulations, the SN shock acceleration stops only when the shock arrives to the very edge of the progenitor star. This leads to an overestimation of the true shock velocity, as the shock acceleration should stop once the stellar envelope becomes optically thin to the radiation coming from the post-shock region. A detailed calculation of the shock acceleration and break-out is an open problem, which requires a radiation hydrodynamics code. Once the SN ejecta interacts with the shell (see below), the shock velocity quickly drops. Then, the late evolution of the system will be independent on the particular shock velocity obtained, while it will depend on the energy stratification of the SN ejecta, i.e. on the properties of the explosion (energy, ejected mass, fallback and so on) and of the progenitor star. A detailed study of it could potentially constrain the progenitor star, and is left for a future study.

3.4.2 SN shock interaction with the massive shell

At ~ 50 days after the explosion, the shock begins interacting with the massive shell. Radio and optical observations showed that the interaction started ~ 100 days after the explosion (Milisavljevic, Margutti, et al. 2015; Anderson et al. 2017). Then, our simulations overestimate the average shock velocity by a factor of ~ 2 with respect, e.g., to radio observation by (Bietenholz, Kamble, et al. 2018) or to the shock velocity inferred by (Milisavljevic, Margutti, et al. 2015) from absorption lines at 10 days. A lower shock velocity can be due, as mentioned above, to the loss of thermal energy during the shock breakout or, alternatively, to a less steep

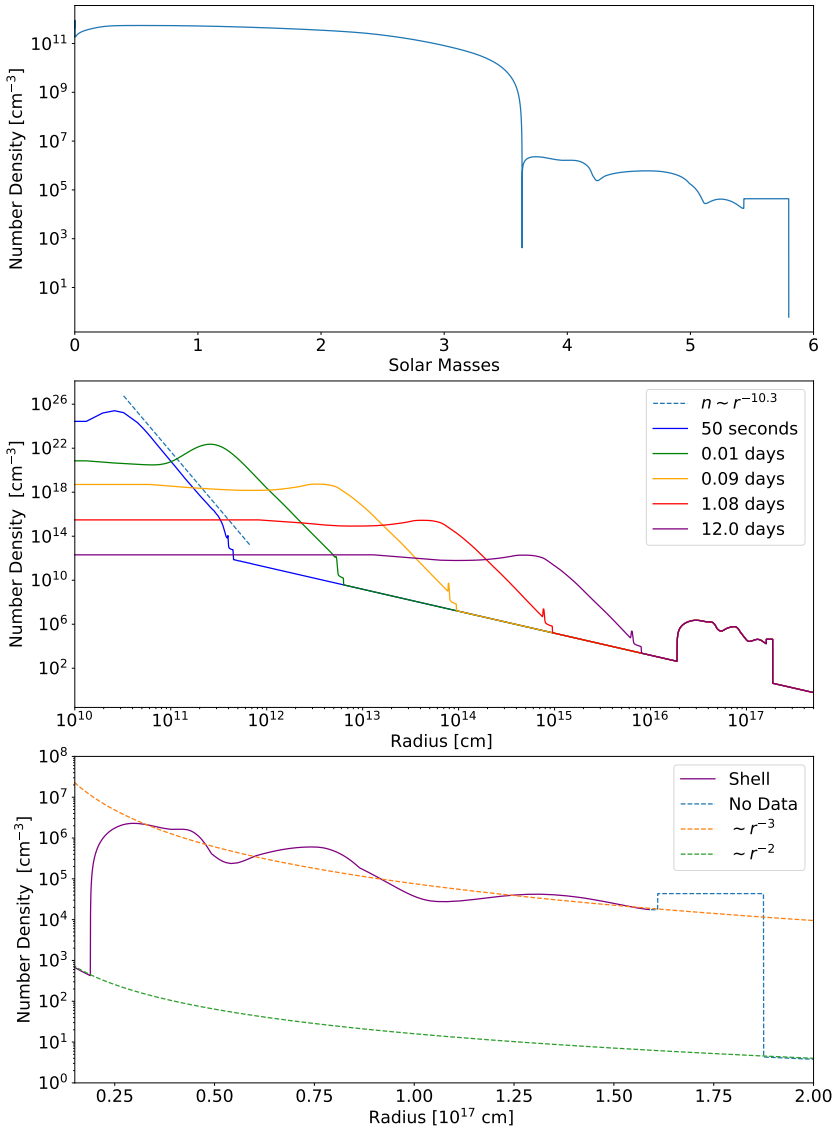

Figure 3.5: *Upper panel*: number density in mass coordinates at 50 s. *Middle panel*: time evolution of the SN shock as it moves through the wind of the progenitor star. The outer ejecta has a self-similar density profile $\rho \propto r^{-10.3}$. *Bottom panel*: structure of the dense CSM located between 1.6×10^{16} cm and 2×10^{17} cm. The plot also shows r^{-2} and r^{-3} density profiles as a reference. The dense CSM is roughly comprised of three consecutive shells, the first goes from 2×10^{16} up to 5×10^{16} cm, the second from 5×10^{16} up to 10^{17} cm, and the third from 10^{17} up to 1.6×10^{17} cm, with an average shell density declining like r^{-3}.

density profile in the outer layers of the progenitor stars.

The interaction of the ejecta with the shell is shown in Figures 3.6 and 3.7. The shell presents large density fluctuations (see the upper panel of Figure 3.7). Then, the shock propagation leads to the formation of strong reverse shocks which interaction produces the complex shock structure observed in Figure 3.7. Once interacting with the shell, the shock velocity[‡] quickly drops to ~ 7500 km s^{-1}, then maintain an approximately constant velocity (see Figure 3.6). Small fluctuations in the shock velocity are present at $\sim 10^3$ days (see the bottom panel of Figure 3), with increases (drops) in velocity by ~ 3000 km s^{-1} corresponding to drops (increases) in the density. The velocities inferred in our model differ from those estimated by VLBI obervations (Bietenholz, Kamble, et al. 2018) by $\approx 50\%$ (slightly larger than 1σ - see the middle panel of Figure 3.6).

The bottom panel of Figure 3.7 shows the evolution of the FS and RS in mass coordinates. Before interacting with the dense CSM, the low-mass post-shock structure remains thin, with the FS and RS very close to each other. While the ejecta interact with the dense CSM, more and more mass is accumulated in the post-shock region, separating the two shocks when seen in mass coordinates. By the end of the simulation (~ 2000 days after the explosion), most of the CSM mass and about $\sim$ a half of the ejecta mass have been shocked.

The velocity plot (third panel from the top in Figure 3.7) illustrates the evolution of the different components, i.e. the unshocked CSM (the stationary medium at large radii), the unshocked ejecta (the region with increasing velocities at small radii) and the shocked CSM and ejecta (the region with fluctuating velocities between the unshocked ejecta and CSM).

Initially, the reverse shock is stronger than the forward shock. Thus, the shocked ejecta is hotter than the shocked wind, i.e. the progenitor wind accelerated and heated by the SN shock front, (Figure 3.7, blue and green lines in the middle panel). As the ejecta crosses the reverse shock and approaches the reverse shock velocity, the RS temperature drops becoming smaller than the FS temperature. Thus, the bremsstrahlung specific emission (larger at smaller temperatures) is initially dominated by the shocked wind, and later mostly originated into the shocked ejecta. We also notice that the unshocked ejecta mainly cools by adiabatic expansion.

A fit to the density profile (see Figure 3.5, bottom panel) gives $\rho \propto r^{-3.00\pm0.06}$, consistently with the constant shock velocity seen in Figure 3.7 (as $E \sim Mv^2 \sim R^3\rho v^2$ implies that the

[‡]A velocity of $\sim$ half of this value is inferred from the Hα line (Milisavljevic, Margutti, et al. 2015). This is consistent with the hydrogen lines being produced in the post shock clumpy medium or by recombination of the upstream medium.

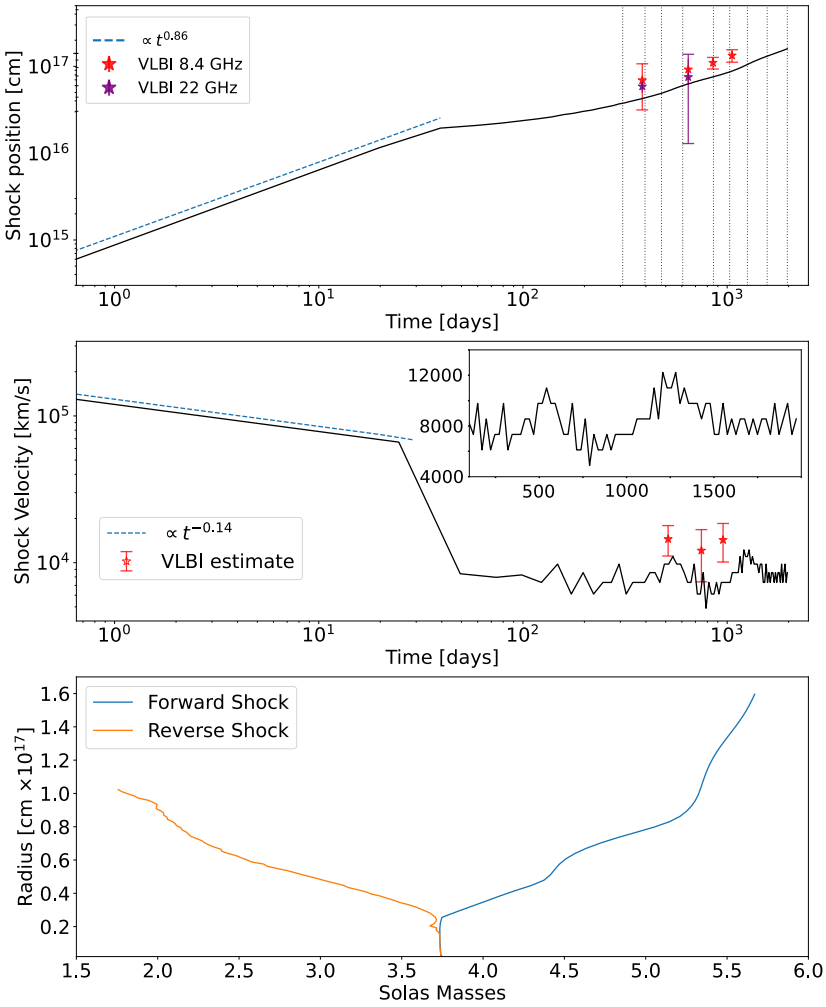

Figure 3.6: *Top panel*: position of the SN shock front as function of time. The break seen at $\sim$ 50 days corresponds to the beginning of the interaction with the shell. The thin vertical lines corresponds to the epochs observed in X-rays. The radii inferred by VLBI observations (Bietenholz, Kamble, et al. 2018) at 8.4 GHz and 22 GHz are also included in the plot. *Middle panel*: shock velocity as a function of time. During the self-similar phase, the shock velocity drops from $\sim$ 0.35c to $\sim$ 0.15c. After interacting with the shell, it drops to $\sim$ 0.025c. The inset shows a zoom corresponding to $t \lesssim 2000$ days. Velocities inferred from VLBI observations (Bietenholz, Kamble, et al. 2018) are also included in the plot. *Bottom panel*: evolution of the forward and reverse shock (in mass coordinates).

velocity is constant as long as $\rho \propto R^{-3}$ and the shock is adiabatic), although the density profile is clearly more complex than what predicted by a power-law fit, as it presents fluctuations larger than ~ 1 order of magnitude, apparently being formed by the joining of three different shells which are centered respectively at 4×10^{16}, 7.5×10^{16} and 13.75×10^{16} cm. The shell mass is 2.6 $M_{\odot}$. This value is consistent with the 3.0 M $\pm$ 0.6 $M_{\odot}$ (VLB model) determined by Brethauer, Margutti, Milisavljevic, Bietenholz, et al. 2022 which also assumes spherical symmetry and within the range of typical shell masses observed in type IIn SNe (0.1-10 $M_{\odot}$, see, e.g., Smith 2017b; Branch and Wheeler 2017b).

One of the parameter of the GA was the 11th density specified in the shell structure (corresponding to the dashed region of Figure 3.7). This was the average density of shell material not yet reached by the SN shock front. This density allows us to determine the amount of neutral hydrogen still to be crossed by the ejecta (inferred from the bound-free absorption). We get M = 0.38 $M_{\odot}$ solar masses for this component at t = 1971 days, which is represented by a constant density dashed line in the top panel of Figure 3.7. We notice that the exact structure of this region can not be determined. Nevertheless, it will extend to $r \sim 2.3 \times 10^{17}$ cm if the shell density continues dropping as r^{-3}, in which case (moving at a constant speed as discussed above) the SN shock will break out of it ~ 8.5 years after the explosion. Late X-ray and radio observations will help to constrain the outer structure of the shell. We also notice that (Milisavljevic, Margutti, et al. 2015) constrained the density of the unshocked CSM to be $< 10^7$ cm^{-3}, which is consistent with the results shown here, and the temperature of $\approx 2 - 8 \times 10^4$ K.

3.4.3 Radiation

Figure 3.9 shows the X-ray spectra at 308, 396, 477, 606, 857, 1029, 1257, 1571, 1971 days and the radiation emitted as a result from the models obtained by employing the GA (Section 3.3.4). Dashed lines are computed by assuming solar metallicity in the neutral shell, the continuous lines consider half of the cross section of the material used in the solar metallicity model. We include in the Figure also the X-ray emission computed by considering a simple r^{-3} density profile obtained by using as parameters of the GA the normalization factor (i.e., the parameter A in the equation $\rho = Ar^{-3}$) and the position and width of the shell. The fit is clearly poor in this case, implying that the "bumpy´´ structure inferred from the GA algorithm is not due to an overfitting of the X-ray data. We also notice that the presence of small scale fluctuations in the X-ray observations is not generated in our simple 1D model,

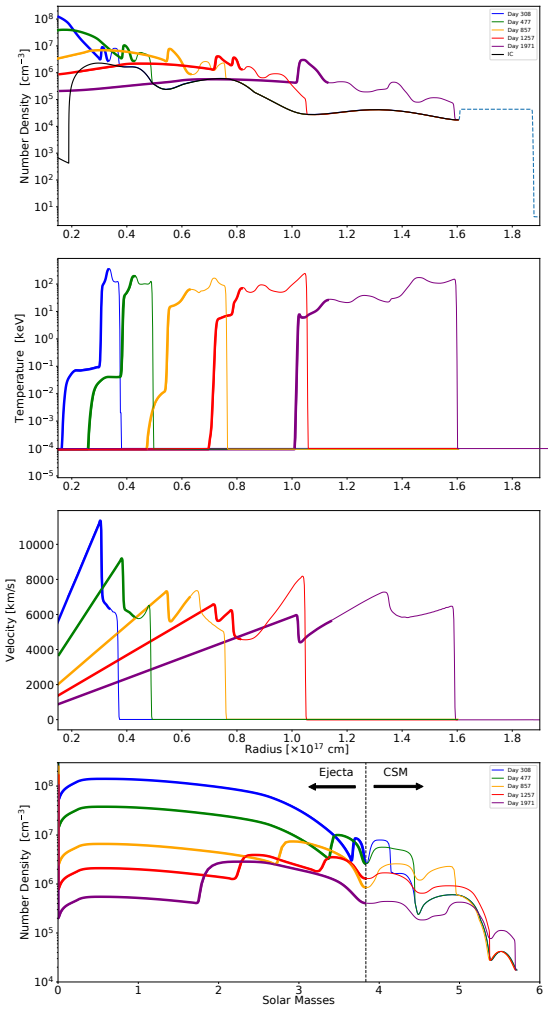

Figure 3.7: The figure illustrates the time evolution of the shock front and supernova ejecta as they interact with the dense circumstellar medium (CSM). X-ray observations are available for the epochs indicated by the lines. The initial shell density profile is denoted as "IC," with the ejecta and CSM material represented by thicker and thinner lines, respectively. The separation is fixed in mass coordinates, as shown in the bottom panel. In addition to the nine densities corresponding to the epochs with X-ray data, the unshocked neutral mass is estimated by considering bound-free X-ray absorption. This region, indicated by a dashed line in the top panel, is shown as uniform since the absorption depends only on the mass crossed by the X-rays, rather than the density stratification.

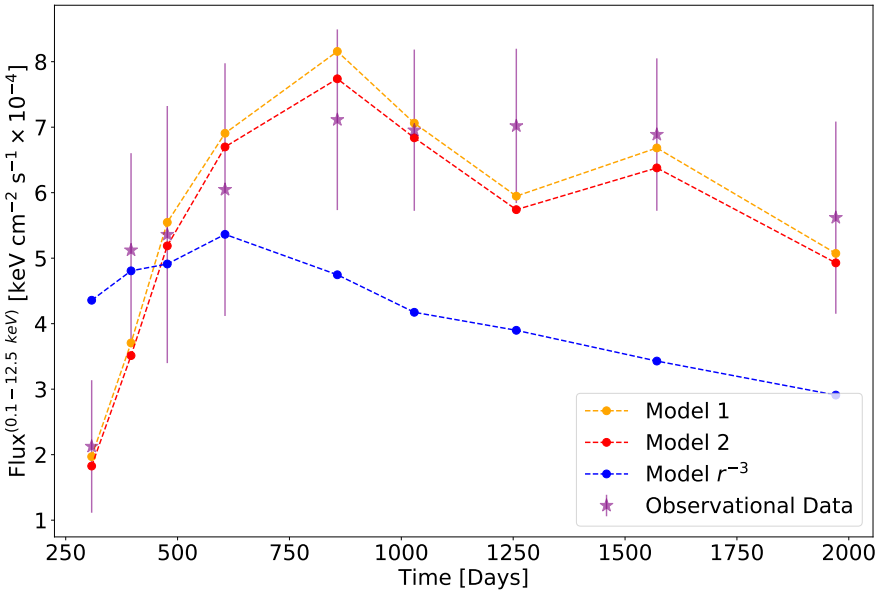

Figure 3.8: X-ray light curve at $0.1 - 12.5$ keV. The observational data (stars) is compared with the models computed by the GA. The three models shown correspond to a cross-section computed assuming solar metallicity (indicated by Model 2 in the Figure, and a model (1) computed assuming half of that cross-section. The third model is a simplified r^{-3} density profile model, where the formation of the bumps was not allowed, showing that the bumps are necessary to fit observational data.

and can be due to the presence of a clumpy medium which would require a multi-dimensional study, or to the presence of unresolved lines (this explain the normalized χ^2 larger than 1 obtained in our optimizing procedure).

The best fit, in this case, predicts a larger absorption by a factor $\lesssim 5$ at 2×10^{17} Hz than observed. Solid lines, which fits better the observational data, are computed by reducing the cross-section by a factor of two and, then, running a new set of simulations using the GA. We notice that the shell density structure obtained from this calculation is nearly identical to the first one, showing the robustness of the result. The implications of this result will be discussed in the next Section.

Finally, Figure 3.8 shows the X-ray flux integrated over the range of frequencies used in the GA, i.e. $0.1 - 12.5$ keV, excluding the region between 5.3 keV and 7.8 keV where the emission from Fe lines dominates the X-ray flux. The "bump" models are in general agreement with the observations and also it is possible to see that observations can not be explained by simple r^{-3} density profile.

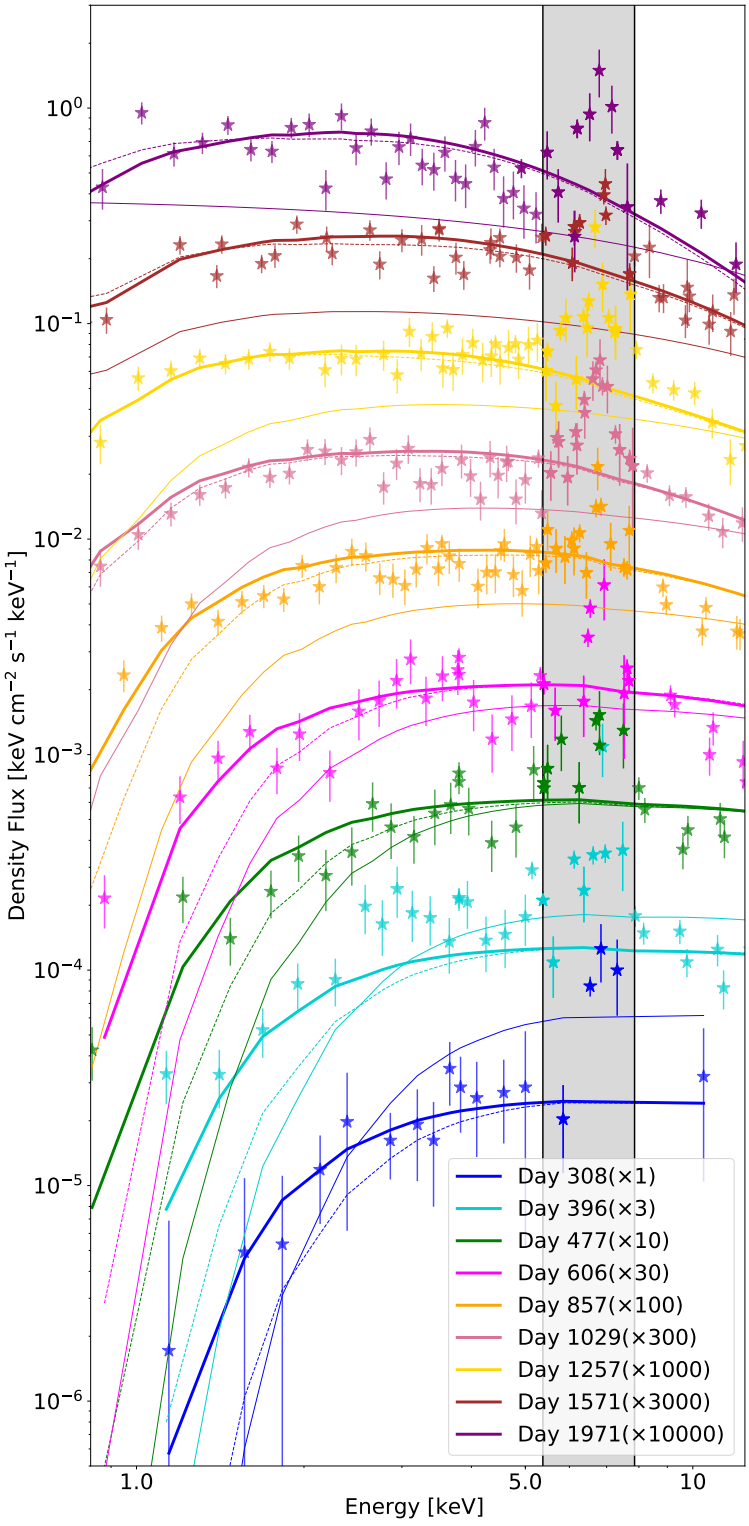

Figure 3.9: Comparison between X-ray observations and synthetic observations computed for the best model. Dashed lines correspond to a bound-free cross-section computed for solar metallicity and assuming that the upwind CSM is neutral. Full lines are obtained by considering a half of this bound-free cross-section. We do not include the shaded grey area in the fit, as it is dominated by Fe emission lines. The thin lines are computed by assuming a simple r^{-3} density profile. Curves at different times are rescaled as indicated in the Figure, so they do not overlap with each other.

3.5 Discussion

The optimization method employed in this work allows us to determine the detailed structure of the shell. As described in the previous section, the shell has a mass of 2.6 $M_\odot$ (2.2 $M_\odot$ of shocked and 0.4 $M_\odot$ of still unshocked gas), a density stratification which at first order can be approximated as $\rho \propto r^{-3}$ and extends from 2×10^{16} cm to 2×10^{17} cm. While uncommon in type Ib SNe, SN IIn show evidence of strong interaction, with shell masses of $0.1 - 10$ $M_\odot$ Smith 2017b; Branch and Wheeler 2017b. Also, many type IIn SNe show an X-ray emission inconsistent with a density profile $\rho \propto r^{-2}$, implying a steeper density stratification Dwarkadas and Gruszko 2012. While sharing many characteristics with SN IIn, in the case of the SN 2014C the shell is located at a much larger distance, implying that it was ejected $\sim 60/(v_w/100 \text{ km s}^{-1})$ yrs before the SN explosion.

Several papers have inferred the properties of the massive CSM from the observations. Based on the models of Chevalier and Liang 1989, Margutti, Kamble, et al. 2017 modelled the behaviour of the X-ray light curve by considering three components: a low-density wind, a high-density shell, and an outer wind with an unkown density profile. Margutti, Kamble, et al. 2017 modelled the high density shell as a $\approx$ 1-1.5 $M_\odot$, constant density medium (which is excluded by our numerical simulations). Tinyanont et al. 2019 and Harris and Nugent 2020 presented ea similar, three components models. These works focused on the high density shell and outlying material. Tinyanont et al. concluded that ~ 1 $M_\odot$ of material has been shocked by the SN 2014c ejecta by 400 days. Harris and Nugent 2020 presented numerical simulations of a SN ejecta interacting with a wall located at $r_0 \sim 2 \times 10^{16}$ cm, and with a CSM wind at larger radii. They deduce a small mass for the wall ($\sim 0.04 - 0.31$ $M_\odot$), while the CSM wind density is assumed to be a factor 4-7 smaller than the density of the wall at r_0. The CSM wind, then, corresponds to a mass loss $\dot{M}_w \sim 10^{-2}$ $M_\odot$ yr^{-1} (assuming $v_w = 10^8$ cm s^{-1}).

Our results (which, we stress, have been obtained by a "blind" fit, i.e. without assumptions on the final shell structure) clarify the structure of the massive CSM. In particular, our results imply that the wall and the CSM wind considered by Harris and Nugent 2020 are both part of the same extended structure (see Figure 3.7), with the densest shell material located at $\sim 2 \times 10^{16}$, and the outer shell density dropping quickly with radius. Thus, we conclude that the same event is responsible for the ejection of the full massive shell.

The parameters determined for the SN 2014C are remarkably similar to those inferred for the SN 2001em. The X-ray, radio and Hα emission from SN 2001em have been interpreted as evidence of interaction with a 3 $M_\odot$ hydrogen-rich shell (Chugai and Chevalier 2006). VLBI

observations showed that the shell is located at 7×10^{16} cm, and expanding with a velocity of 5800 ± 10^4 km s^{-1} Bietenholz and Bartel 2007, which is consistent with the 7500 km s^{-1} inferred here.

The X-ray emission is strongly absorbed at low frequencies. To compute it, we have used a tabulated cross-section which assumes solar metallicity and assuming that the upstream medium is neutral. We have also shown that employing a smaller cross-section leads to a better fit at low frequencies. This has interesting implications on the properties of the upstream shell material.

There are two physical main mechanisms which can modify the absorption cross-section. In the first one the metallicity can be lower than solar (which, by the way, would also lead to a lower X-ray flux). We notice that a lower metallicity is in contradiction with observations of the Fe line. The prominent Fe emission line at 6.7-6.9 keV is consistent with a metallicity larger by a factor of ~ 5 with respect to solar metallicity. This can be reconciled with our results by assuming that the medium is clumpy, with high density (and lower temperature) regions responsible for most of the Fe emission (Margutti, Kamble, et al. 2017). In the second the upstream medium can be partially ionized due to the strong ionizing X-ray flux coming from the post-shock region, as the optical depth is $\propto n_{H^0}\sigma_\nu$, being n_{H^0} the density of neutral hydrogen and σ_ν the bound-free cross-section. This is indeed very likely considering that the X-ray emission and/or UV radiation coming from the shocked shell and SN ejecta can partially ionize the unshocked material. In this case, we expect the mass of the shell to be larger than the value obtained in this paper, although by a small factor as the bremsstrahlung emission is $\propto n_e^2$. A detailed calculation of the ionization of the shell, left for a future work, will help to clarify which among these two effects is dominant, and will potentially help to determine the ionization degree and metallicity of the dense CSM.

Different origins for the shell have been considered. The possibility of the shell being due to a massive wind ejection is unlikely (De Jager, Nieuwenhuijzen, and van der Hucht 1988; Leitherer 2010; Kuriyama and Shigeyama 2020), as it would correspond to an extremely large mass loss rate of $\sim 10^{-2}$ M$_\odot$ yr^{-1} (v_w/100 km s^{-1}). Other possibilities include a sudden outburst some time before collapse, which would remove the most external layer of the star where almost all hydrogen is found (Smith and Arnett 2014), or binary system interactions in which the envelope of the most massive star has been stripped away (Sun, Maund, and Crowther 2020). A better understanding of the origin of this ejections can be achieved only by detailed theoretical models coupled to a larger sample of observed interacting supernovae. Anyway, that future models exploring the origin of this massive shell will need to account for

the density profile, size and mass obtained in this work.

The dense CSM presents density fluctuations. It is roughly formed by three consecutive shells, the first one from $(2-5)\times10^{16}$ cm, the second from $(5-10)\times10^{16}$ cm, and the third from $(10-16)\times10^{16}$ cm, with average shell density declining like r^{-3}.

The density fluctuations have a characteristic length scale of $\sim 4\times10^{16}$ cm. A similar length scale has been observed in the radio emission from SN 1979C (Weiler et al. 1991) and has been interpreted as evidence of a binary system in which the orbital motion modulates the wind density Yalinewich and Zwart 2019 which interacts with the stellar outburst. If this is also the case of SN 2014C, it would imply that the binary system is very detached (as the binary period is $\gg 4\times10^{16}/v_w \sim 10$ yrs $(v_w/10^8)^{-1}$). The companion star would then be not responsible for the loss of the envelope of the primary star. An alternative explanation is that the density fluctuations seen in the GA fit are the direct result of a modulation in the outburst from the progenitor star.

Finally, we notice that the simulations presented here assume that the shell is spherically symmetric. This is consistent with VLBI observations (Bietenholz, Kamble, et al. 2018). On the other hand, the velocities estimated by the GA are smaller than those inferred from VLBI observations (and, puzzling, larger than those inferred by the Hα emission line, corresponding to $\sim$ a few thousand km s^{-1}). The density profile shown in Figure 3.7 show large scale (i.e., much larger than the size of our computational cells) density fluctuations which, in spherical symmetry, correspond to fluctuations among contiguous shells of material. Actually, it is likely that the medium is clumpy, with the clumps necessarily breaking the spherical symmetry. In this case, the interaction with the SN ejecta will amplify the inhomogeneities (Guo et al. 2012; Velázquez et al. 2017), leading to a multi-phase medium with denser/colder regions in pressure equilibrium with more tenuous/hotter regions, which could explain the strong Fe emission line observed at $\sim$ 6.5 keV (Margutti, Kamble, et al. 2017).

A more realistic scenario, with density stratification in the shell not only in the radial, but also along the polar direction, could also explain the apparent discrepancies in the velocities inferred by the different emission processes, with faster material, moving along lower density regions of the shell, emitting in radio, and denser regions, moving at lower speeds, emitting in X-rays and radio. Such a complex (but possibly more realistic) scenario requires multi-dimensional simulations and is left for a future study.

Also if the shell is initially nearly perfectly homogeneous, the contact discontinuity which separates the shocked SN ejecta from the shocked shell is prone to Rayleigh-Taylor (RT) instabilities, so that we can expect the formation of plasma filaments and inhomogeneities

in the post-shock region which can not be captured by our numerical simulations (but see (Harris and Nugent 2020) for an approximated treatment of RT instabilities in one dimensional simulations). As the bremsstrahlung emission is $\propto Z^2 n^2$, inhomogeneities in the shell and mixing with the higher metallicity ejecta lead to a larger emissivity, implying that the mass of the shell should be taken as an upper limit.

3.6 Conclusions

In this paper, we presented hydrodynamical simulations of the strongly interacting SN 2014C. First, we follow the propagation of a SN shock through the progenitor star. Then, by using as input the outcome of the small scale simulation (i.e., density, pressure and velocity profiles), we run a large set of simulations. As described in section 3.3.4, we initialize the shell with a uniform density $n_{\rm shell} = 10^7$ cm^{-3}.

We followed the propagation of the SN shock as it interacts with the wind launched by the progenitor Wolf-Rayet star and with the massive shell. We computed the bremsstrahlung emission using the algorithm described in Section 3.3.2, and compare the results with observations. At each step, we run a large number of simulations changing the shell density profile. As a result, we determine the shell structure. In particular, we get a mass of 2.6 $M_\odot$ for the shell and a density profile roughly dropping as $\rho \propto r^{-3}$ although presenting large density fluctuations. We also found that the shell is very extended, with a size $\gtrsim 10^{17}$ cm. If the shell stratification continues with the same average slope, the SN shock will break out of it nearly 8 yrs after the explosion, i.e. during 2022.

Although this paper represents one of the most detailed model of the interaction between the SN ejecta and the surrounding massive CSM, several ingredients are still missing from our model. In particular: we have explored only one pre-supernova structure; we have modelled only the X-ray emission, while radio emission (specially images obtained by VLBI, see e.g. Bietenholz, Bartel, et al. 2021) contain detailed information about the evolution of the shock and its interaction with the medium; we have not included a detailed treatment of the photoionization of the upwind medium, which can affect the bound-free absorption. Finally, and most importantly, we assumed that the shell structure is spherically symmetric.

Radio and X-ray emission allows us to understand the mass loss history of core-collapse SNe progenitor on time-scales which are impossible to study by direct observations. As we have shown in this paper, optimization methods can be used, coupled with hydrodynamical simulations, to model the density stratification of the environment once data at several epochs

are available, as in the case of SN 2014C. The X-ray emission tracks the forward and reverse shock emission, depending on the density of the environment and the ejecta velocity. The Hα emission tracks the shocked shell and the unshocked medium fotoionized by the X-ray and UV radiation. All together, a detailed fit of the different components can help us to get a better understanding of this system. Then, coupled with detailed modeling of the radio emission, this analysis can allow us to determine the microphysical parameters as a function of time (which are usually degenerate with the density of the environment and ejecta velocity), giving us direct information on the particle acceleration process. In this paper, we describe this technique by analyzing the X-ray bremsstrahlung emission. The extension to radio and optical emission will be considered in a future study.

Acknowledgements

We thank the anonymous referee for the helpful comments, and constructive remarks on this manuscript. We thank Luc Binette, Cesar Fernández Ramírez, Leonardo Ferreira and Claudio Toledo Roy for useful discussions. FV and FDC acknowledge support from the UNAM-PAPIIT grant AG100820. We acknowledge the computing time granted by DGTIC UNAM (project LANCAD-UNAM-DGTIC-281). R.M. acknowledges support by the National Science Foundation under Award No. AST-1909796 and AST-1944985. Support for this work was provided by the National Aeronautics and Space Administration through Chandra Award Number GO9-20060A issued by the Chandra X-ray Center, which is operated by the Smithsonian Astrophysical Observatory for and on behalf of the National Aeronautics Space Administration under contract NAS8-03060.

Software

Matplotlib (Hunter 2007), NumPy (Contributors 2021), Mezcal (De Colle, Granot, et al. 2012).

Chapter 4

Machine learning the way through interacting supernovae

This chapter presents preliminary results of our study on the application of machine learning models to simulate the SN 2014C.

4.1 Abstract

We present a study of the early evolution of interacting supernovae, focusing on the behavior of the spherical shell surrounding the progenitor of SN 2014C. In Brethauer, Margutti, Milisavljevic, Bietenholz, et al. 2022 it was suggested that the density of the medium surrounding the SN 2014C could vary with angle, based on the observations of the radio emission and the position of the shock wave. To better understand the behavior of the shell surrounding the progenitor of SN 2014C, a series of simulations varying the characteristics of the shell are conducted. We produce synthetic observations in radio and X-rays, which are used to train machine learning models that can take observational data and directly provide the initial conditions that model the system. We train a neural network to map observed emission to the underlying parameter space, enabling us to infer parameter values from observational data. We find that variations in four key parameters significantly affect the early evolution of supernovae, and that our machine learning approach provides valuable insights into the characteristics of interacting supernovae. We show that the CSM is stratified along the angular direction. The X-ray emission is consistent with $\sim 50\%$ of the solid angle occupied by a dense shell, with a maximum density of 2×10^6 cm^{-3} located at 2×10^{16} cm, with a total mass of

3.8 $M_\odot$, while the radio emission is consistent with a region with a density about 100 times lower (2×10^4 cm^{-3}) peaking approximately at the same location as the X-ray emission, and with a mass of ~ 0.1 $M_\odot$. Our study highlights the potential of combining simulations and machine learning to improve our understanding of astrophysical systems, and has important implications for future studies of supernovae and other phenomena. By using a combination of observational data, simulations, and machine learning, we can better understand the behavior of complex systems and make more accurate predictions about their evolution and characteristics.

Supernovae - Stellar mass loss - Circumstellar shells - Astronomy data modeling - Stellar-interstellar interactions

4.2 Introduction

Interacting supernovae are a sub-class of core-collapse supernovae showing signatures of strong interaction between the ejecta and the circumstellar medium (CSM). By studying pre-supernova outbursts and iSNe UV emission, spectral lines, and X-ray and radio light curves rebrightening (Smith 2014; Pastorello, Kochanek, et al. 2018; Margutti, Milisavljevic, et al. 2014; Morozova, Piro, and Valenti 2018; Dessart and Hillier 2022; Filippenko 1997; Perley, Sollerman, et al. 2022; Sollerman et al. 2020; Jin, Yoon, and Blinnikov 2021; Soraisam et al. 2022; Chevalier and Fransson 2006; Chevalier, Fransson, and Nymark 2017; Chugai and Chevalier 2006; Mauerhan, Filippenko, et al. 2018; Schinzel et al. 2009a; Bietenholz, De Colle, et al. 2014; Tinyanont et al. 2019; Harris and Nugent 2020; Vargas et al. 2022), the mass-loss history from the progenitor massive stars and binary systems can be recovered.

Among iSNe, SN 2014C is an intriguing case that has garnered significant attention due to its unusual behavior. Recent observational studies and modeling efforts suggest that the presence of dense CSM in the vicinity of the SN is responsible for the observed emission (Milisavljevic, Margutti, et al. 2015; Margutti, Kamble, et al. 2017; Tinyanont et al. 2019; Brethauer, Margutti, Milisavljevic, Bietenholz, et al. 2022; Vargas et al. 2022). SN 2014C underwent a metamorphosis from an ordinary H-stripped core-collapse SN into a SN with clear signs of interaction with an H-rich medium (Milisavljevic, Margutti, et al. 2015). Understanding the observational signatures of iSNe and the underlying physical processes is crucial and a tool to unveil the history of mass loss in massive stars and the role it plays in their final evolutionary stages. Theoretical studies (Vargas et al. 2022; Harris and Nugent 2020) assumed that the CSM is spherically symmetric. On the other hand, while a SN shock wave

of $v_{\rm sh} \simeq 14000$ km s^{-1} has been inferred from radio VLBI images (Bietenholz, Bartel, et al. 2021), the X-ray and Hα emission are consistent with a lower velocity (i.e., 2000-6000 km s^{-1}, see Margutti, Kamble, et al. 2017; Brethauer, Margutti, Milisavljevic, Bietenholz, et al. 2022; Vargas et al. 2022). This discrepancy led Brethauer, Margutti, Milisavljevic, Bietenholz, et al. 2022 to suggest that there is an angular asymmetry in the CSM distribution. These models and observations highlight the need for a deeper understanding of the asphericity of iSNe and their circumstellar environments.

Modeling interacting supernovae (iSNe hereafter) is challenging since it involves complex physical processes that are difficult to simulate accurately, including shock breakout, shock-cloud interaction, among others. To model the interaction between the ejecta and the circumstellar medium (CSM), one needs to consider the density and composition of the surrounding medium, the strength and direction of the shock wave, and the energy and radiation emitted by the supernova. Thus, one of the major challenges in modeling iSNe is the computational complexity involved. Simulating these events requires advanced numerical methods and computational resources, which can be expensive and time-consuming. Additionally, there is still much that is not fully understood about the physical processes involved, which can make it difficult to develop accurate models. Another challenge is that iSNe are relatively rare events, and observations are limited. This means that one often has to rely on simulations and theoretical models to understand the underlying physics, which can be difficult to validate without direct observations.

Although it is a difficult task, modeling iSNe has the potential to provide important insights into the behavior of stars and the evolution of the progenitors of supernova (SN), since the material surrounding composes a dense circumstellar medium (CSM), that usually comes from its progenitor. Simulating the interaction of the SN shock wave with the CSM poses a challenge as well, due to the need for a detailed understanding of the progenitor mass loss history (Chevalier, Fransson, and Nymark 2017).

In order to better address these challenges, state-of-the-art methods are imperative to accurately describe the behavior observed in iSNe. Vargas et al. 2022 applied a genetic algorithm to model the CSM from SN 2014C, even without full knowledge of its mass loss history. Such methods have the potential to overcome the limitations of numerical simulations and provide valuable insights into the physics of iSNe.

In this work, we present a new approach to infer the conditions that govern the aspherical CSM distribution of the SN 2014C by training a Machine Learning model on a large dataset of one-dimensional hydrodynamic simulations. Machine learning has become increasingly impor-

tant in astrophysics as the amount of observational data continues to grow at an exponential rate. With the development of new telescopes and surveys, astronomers have access to vast amounts of data that would be impossible to analyze manually. Machine learning algorithms can analyze this data and extract useful information such as identifying patterns, classifying objects, and predicting properties. In astrophysics, machine learning has been used for a wide range of applications, including exoplanet detection (Malik, Moster, and Obermeier 2021), galaxy classification (Ferreira et al. 2020), SN classification (Lochner et al. 2016) and spectral modeling (Vogl et al. 2020), and gravitational wave detection (Ni 2016). Machine learning has enabled astronomers to make discoveries and gain new insights into the universe that would have been impossible with traditional methods. As the field of astrophysics continues to advance, machine learning will undoubtedly play an even more significant role in unlocking the mysteries of the cosmos.

Our methodology of coupling relativistic hydrodynamic codes with radiative transport codes and machine learning is a novel approach in astrophysics that has the potential to provide insights into the initial conditions of astrophysical systems. By using machine learning algorithms to analyze radiative emission simulations, we can identify the factors that determine the initial state of the system, which would be difficult to infer using traditional methods. We illustrate the effectiveness of this approach by applying it to the case of SN 2014C, which has been extensively studied in the literature. The successful application of machine learning to this system opens up new avenues for studying other astrophysical systems and could lead to a deeper understanding of the underlying physical processes.

4.3 Methods

In this paper, we present a novel methodology that combines the use of a hydrodynamic code (De Colle, Granot, et al. 2012) with a machine learning algorithm created using the library Keras in Python (Chollet 2015). Our methodology consists of two main components: the first, described in section 4.3.1, involves simulating the interaction of the SN ejecta with the environment (CSM) using the *Mezcal* hydrodynamic code. The second component, described in section 4.3.2, involves using the outputs of the hydrodynamic simulations to train a neural network. The neural network is then used to make predictions about the initial conditions of the system having as input the observational properties of iSNe.

This approach has the potential to greatly improve our ability to model and understand a wide range of iSNe, since once all simulations that generate the training data are finished, it

could be adapted to model the initial conditions of the CSM of any iSN without having to run new simulations.

4.3.1 Numerical codes and initial conditions

We performed about 6 thousand one-dimensional , spherical symmetric simulations using a modified version of the hydrodynamics code *Mezcal* (De Colle, Granot, et al. 2012). The evolution of the system depends on the properties of the CSM and the SN. The initial conditions of our hydrodynamical simulations are described by four parameters: α_1, α_2, R_1, and dR. The computational box spans over several orders of magnitude in space, from $R_i = 10^{-3} \times R_1$ to $R_f = 2.5 \times (R_1 + dR)$. We utilize an adaptive mesh with 10 levels of refinement and 100 cells at the coarsest level of refinement, to provide a fine-grained resolution and allocate computational resources only where necessary. The computational box is divided in two regions: 1) the SN ejecta, which initial conditions are described in section 4.3.1.1; and 2) the CSM, described in section 4.3.1.2.

4.3.1.1 Supernova shock wave and ejecta

The initial conditions for the SN ejecta are created analytically by using self-similar solutions (e.g., Chevalier 1982a). The advantage of using an analytical solution for the SN ejecta is that we can always initialize the shock at the position where it starts interacting with the dense CSM, saving computational time since we do not need to simulate the propagation of the shock before the interaction starts. The initial conditions for the SN ejecta are the following: an explosion energy of 10^{51} ergs; a supernova ejecta mass of $1.4 M_\odot$; a shock front velocity of 0.1 c; a post-shock region that has been partially swept up by a dense CSM, modeled as a uniform-density sphere with a radius of 10^{18} cm and a density of 10^{-21} g cm^{-3}.

We assume a power-law density profile for the ejecta, as described by Harris and Nugent 2020. From the inner boundary of the computational box, r_{1b}, up to a transitional radius called R_t, $(r_{1b} < r < R_t)$, we have

$$\rho(r) = \rho_0 \left(\frac{r}{R_t} \right)^{-1} , \tag{4.1}$$

while for $r > R_t$ the density is defined as

$$\rho(r) = \rho_0 \left(\frac{r}{R_t} \right)^{-n} , \tag{4.2}$$

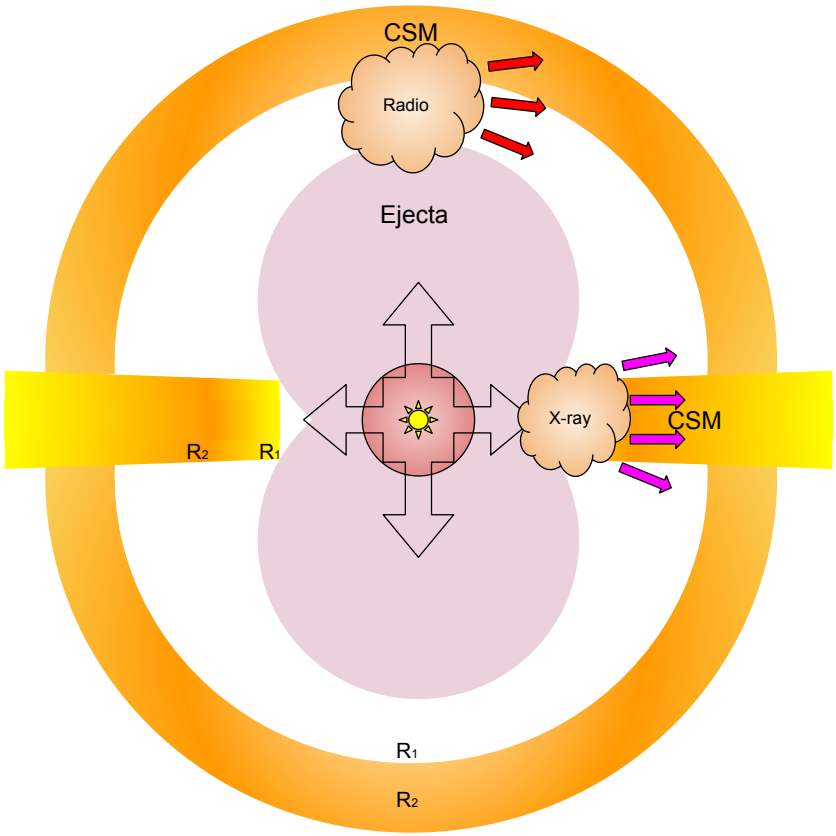

Figure 4.1: Schematic representation of the interaction between the ejecta of a SN and the CSM. The CSM has two main regions: the equatorial region, responsible for the X-ray emission, and the rest of the region, responsible for the radio emission. R_1 marks the initial position of dense CSM, which increases in density until it reaches its maximum value at R_2, after which the density starts to decrease.

where

$$\rho_0 = \frac{1}{2\pi}\frac{M_{\rm ej}}{Rt^3}\frac{(n-3)}{(n-1)} \tag{4.3}$$

The velocity in the SN ejecta is given as,

$$v(r) = v_{\rm sh}\frac{r}{R_{\rm sh}}\ , \tag{4.4}$$

being $v_{\rm sh} = 0.1$ c, and $R_{\rm sh} = v_{\rm sh}t$ the initial position of the SN shock. The velocity at the critical radius R_t is given as

$$v_t = 6\times 10^8 \xi_v \left(\frac{E_{51}}{M_c}\right)^{\frac{1}{2}}\ {\rm cm\ s^{-1}} \tag{4.5}$$

where E_{51} is the SN energy in units of 10^{51} ergs, $M_c = M_{\rm ej}/M_{\rm ch}$, being $M_{\rm ch}$ the Chandrasekhar mass, and

$$\xi_v = 2\left(\frac{n-5}{n-3}\right)^{\frac{1}{2}}\ . \tag{4.6}$$

The value of n depends on the specific model used and can range from $\approx 8-10$ (e.g., $n = 9$ for SN type Ib, $n = 10$ for SN type Ia) depending on the density stratification of the progenitor star. A schematic representation of the initial SN ejecta and CSM structures is shown in Figure 4.1.

4.3.1.2 Density of the circumstellar medium

The density of the CSM is parameterized by using four parameters. We assume that the supernova shock front expands freely up to the position of the shell ($r = R_1$). We initialize the density of the shell in the numerical simulation by using power-law segments. Before the beginning of the simulation, at radii $r < R_1$, the SN ejecta interacted with the wind of the progenitor star:

$$\rho(r) = Ar^{-2}\ , \tag{4.7}$$

being $A = \dot{M}_w/(4\pi v_w)$ the normalization factor, $\dot{M}_w$ the mass-loss rate and v_w the wind velocity. At distances $r > R_1$, we include in the numerical simulation a shell, with a maximum density at $r = R_2$. We assume that the shell density increases for $R_1 < r < R_2$ as

$$\rho(r) = \frac{A}{R_1^2}\left(\frac{r}{R_1}\right)^{\alpha_1}\ , \tag{4.8}$$

has a maximum ($\rho_{\rm max} = \dot{M}_w/(4\pi v_w)/R_1^2(R_2/R_1)^{\alpha_1}$) at $r = R_2$, and drops for $R_2 < r < R_f$ as

$$\rho(r) = \frac{A}{R_1^2}\left(\frac{R_2}{R_1}\right)^{\alpha_1}\left(\frac{r}{R_2}\right)^{-\alpha_2}\ , \tag{4.9}$$

with $\alpha_1, \alpha_2 > 0$. In these equations, the normalization factors are chosen such that the density is continuous at R_1 and R_2.

The masses of the CSM in the different regions are

$$M(< R_1) = 4\pi R_1 A = \frac{R_1 \dot{M}_w}{v_w} , \tag{4.10}$$

$$M(R_1 < r < R_2) = \frac{R_1 \dot{M}_w}{v_w} \frac{(R_2/R_1)^{3+\alpha_1} - 1}{3+\alpha_1} . \tag{4.11}$$

The mass in the external part of the shell, $M_e = M(R_2 < r < R_f)$, depends on the value of α_2. We get

$$M_e = \frac{R_1 \dot{M}_w}{v_w} \left(\frac{R_2}{R_1}\right)^{3+\alpha_1} \frac{(r/R_2)^{3-\alpha_2} - 1}{3-\alpha_2} , \tag{4.12}$$

if $\alpha_2 \neq 3$, and

$$M_e = \frac{R_1 \dot{M}_w}{v_w} \left(\frac{R_2}{R_1}\right)^{3+\alpha_1} \log\left(r/R_2\right) . \tag{4.13}$$

if $\alpha_2 = 3$.

4.3.1.3 Radio and X-ray emission

To compare models with observations, we compute the X-ray bremsstrahlung emission coming from the shocked plasma by post-processing the results of the hydrodynamical simulations as done previously in Vargas et al. 2022. We consider the bremsstrahlung (free-free) self-absorption

$$\alpha_\nu = \alpha_{\nu,\mathrm{ff}}; , \qquad j_\nu = j_{\nu,\mathrm{ff}}; . \tag{4.14}$$

For the bremsstrahlung coefficients we take e.g., Rybicki and Lightman 1986

$$j_\nu = \frac{6.8}{4\pi} \times 10^{-38} Z^2 n_e n_i T^{-1/2} e^{-\frac{h\nu}{kT}} G \tag{4.15}$$

$$\alpha_\nu = 3.7 \times 10^8 T^{-1/2} \frac{Z^2 n_e n_i}{\nu^3} \left(1 - e^{-\frac{h\nu}{kT}}\right) G , \tag{4.16}$$

where Z, n_e and n_i are the atomic number, electron and ion densities, respectively, and G is the Gaunt Factor (~ 1 for the range of parameters considered here).

The radio emission was calculated as well by post-processing the results of the numerical simulations, using the equations described by Chevalier 1998. We consider a standard low-frequency, self-absorbed flux, with a flux given as

$$F_{\mathrm{thick}} = \frac{\pi r^2 c_5 B^{-\frac{1}{2}} \left(\frac{\nu}{2c_1}\right)^{\frac{5}{2}}}{D^2 c_6} , \tag{4.17}$$

and a high frequency, optically thin spectrum with

$$F_{\text{thin}} = \frac{4\pi f r^3 c_5 N_0 B^{\frac{\gamma+1}{2}} \left(\frac{\nu}{2c_1}\right)^{\frac{1-\gamma}{2}}}{3D^2} \tag{4.18}$$

where B is the magnetic field, c_1, c_5, c_6 are tabulated constants, r is the shock position, ν the observed frequency, D the distance from the source, f is the filling factor, N_o is a normalization constant proportional to the density of relativistic electrons per unit energy, and γ is the power-law index of the population of accelerated electrons

From these equations, we get the values of the syncrotron self-absorption ν_{sa} and the flux at ν_{sa} as:

$$\nu_{sa} = 2c_1 \left(\frac{4rc_6 f N_{\text{o}}}{3}\right)^{\frac{2}{4+\gamma}} B^{\frac{\gamma+2}{\gamma+4}} , \tag{4.19}$$

$$F(\nu_{sa}) = \frac{\pi r^2 c_5}{D^2 c_6} \left(\frac{4}{3}\right)^{5/2} (rc_6 f N_o)^{5/(4+\gamma)} B^{-(\gamma+1)/(2+\gamma)} . \tag{4.20}$$

Given the self-absorption frequency and the flux at the self-absorption frequency, it is easy to determine the flux at any frequency as

$$F(\nu) = F(\nu_{sa}) \left(\frac{\nu}{\nu_{sa}}\right)^{\alpha} , \tag{4.21}$$

wher $\alpha = 5/2$ if $\nu < \nu_{sa}$, and $\alpha = -(\gamma - 1)/2$ if $\nu > \nu_{sa}$.

4.3.2 Machine Learning

Our simulations explore variations in four parameters that affect the early evolution of the SN, and produce synthetic data that mimic the observed emission. We use this data to train a neural network and map the observed emission to the underlying parameter space, allowing us to infer the values of the parameters from observational data without doing simulations. By using machine learning to better understand the behavior of the CSM and how it changes with angle, this study aims to provide insights into the evolution and characteristics of iSNe.

To infer the parameters that govern the initial conditions of a iSNe, we first obtained its observed radiative emission data. We then applied our trained neural network to map the observed emission data to the underlying parameter space, using the learned mapping from the simulations. Finally, we obtained the inferred parameter values by solving the inverse problem, using a non-linear optimization algorithm that minimized the difference between the predicted and observed emission data. The neural network model is created using

Keras and Tensorflow (Chollet 2015) libraries to predict the parameters of these astrophysical simulations. The neural network receives a input data the parameters x, i.e. the values of the four parameters that are used to create the initial conditions in the hydrodynamic simulations, α_1, α_2, R_i and dR. By post-processing the numerical simulations, we compute the position of the shock at 55 times, the flux at 15.5 GHz at the same times, the values of the X-ray flux at 8 epochs, and the characteristic temperature of the X-ray flux at the same epochs. The synthetic observations mimic the data avaiable for the SN 2014C, where the observed X-ray emission and temperature are extracted from Margutti, Kamble, et al. 2017 and the radio emission and shock wave position are extracted from Bietenholz, Bartel, et al. 2021. Three different models are created (i.e., the neural network is applied independently for the three models): in the first one, we consider the X-ray emission coming from both forward shock (FS) and reverse shock (RS); in the second one only the X-ray emission coming from the FS is computed. In the third one, we consider the radio emission. The X-ray models take 16 input parameters, which are then divided into two groups of eight parameters each for $f(x)$ and $g(x)$, where $f(x)$ is the X-ray emission and $g(x)$ the temperature. The radio model uses two different sets of synthetic data $f(x)$ and $g(x)$, each one with 55 elements, where $f(x)$ is the radio emission and $g(x)$ shock position. Although the data set is adapted to train with the specific observations of the SN 2014C, training the machine learning model is complete in a matter of minutes, and it can be easily adapted to model any iSNe that has observational data.

All neural network models are trained using mean absolute error (MAE) loss function and optimized with RMSprop function optimizer. The dropout rate is set to 0.1 to avoid overfitting, so different parts of the neural network can learn similar operations. The hidden layers consist of four dense layers interspersed with dropout layers. All layers, besides the last dense layer, use the ReLU activation function and the last dense layer uses the linear activation function. The output from the hidden layers is concatenated and passed through another dense layer with a linear activation function. The final output layer has size of four, corresponding to the four parameters that generate the initial conditions for the CSM. During training, early stopping is used with a patience of five epochs to avoid overfitting. The model is trained for a maximum of 10000 epochs, using a batch size of 256.

The total data set of six thousand simulations is divided in three different sub sets. The first one includes 80% of the data, which are the training data set used to optimize the neural network. The second data set has 10% of the data and is known as validation data. This set is not used in training, but a comparison and a loss function are calculated in each epoch of

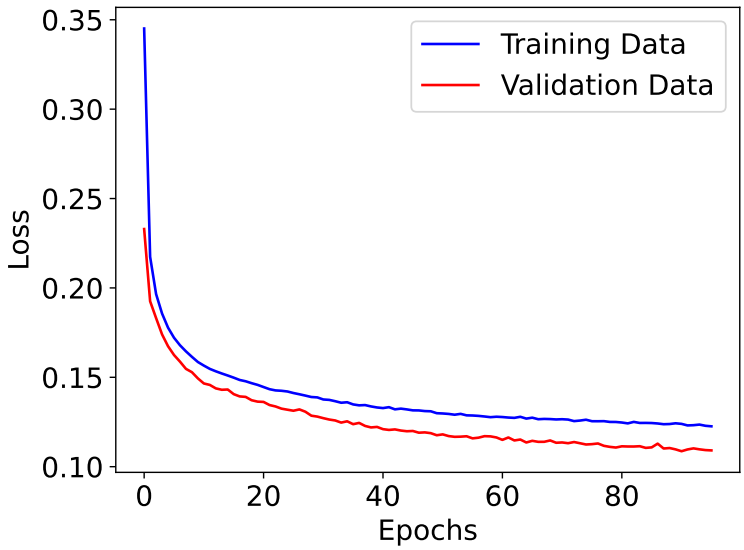

Figure 4.2: Loss function over the epochs of training for the forward shock and reverse shock X-ray training and validation data sets.

evolution of the neural network to confirm that it can solve data that is not used in training. The evolution of the loss function as the neural network evolves can be seen in the Figures 4.2, 4.3 and 4.4. The third data set that has 10% of the total simulations is called test data set and is used to confirm that there is no overfit, which would make the neural network only able to reproduce the training and validation data.

The model predictions are then used to make inferences about the angular distribution of the explosion. The initial simulations are done in 1D with spherical symmetry. We create a variable f, which varies between 0 and 1 and represents the fraction of solid angle emitting radiation. So, for example, if $f = 0.2$, the emission comes from 20% of the total volume of the sphere. A variable $p = 1 - f$ is created to represent the remainder of the solid angle. The idea is to be able to simulate through 1D simulations two different emission regions, one responsible for x-ray data and another for radio.

We tested our inference method on a well-studied Type Ib/c supernova, SN 2014C, using observational data. We compared our inferred parameter values with those obtained from traditional modeling methods, and analyzed the implications for the understanding of the supernova progenitor and explosion mechanism. After the neural network is trained, the values of the initial conditions are found in a matter of seconds.

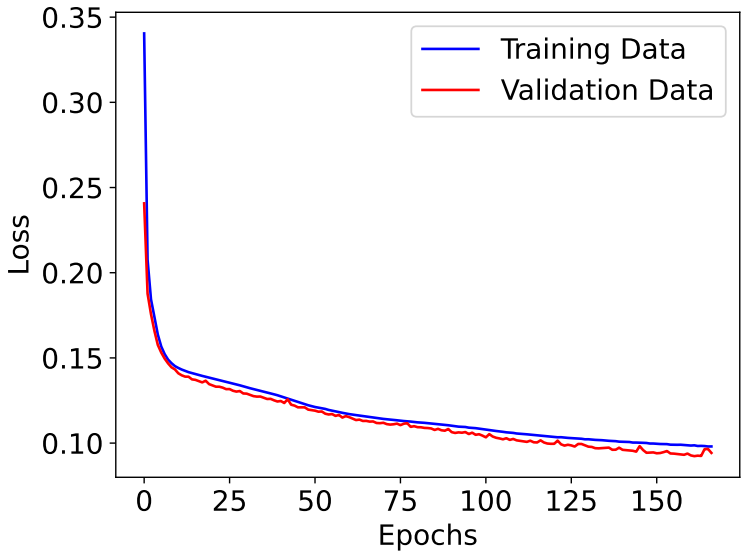

Figure 4.3: Loss function over the epochs of training for the forward shock X-ray training and validation data sets.

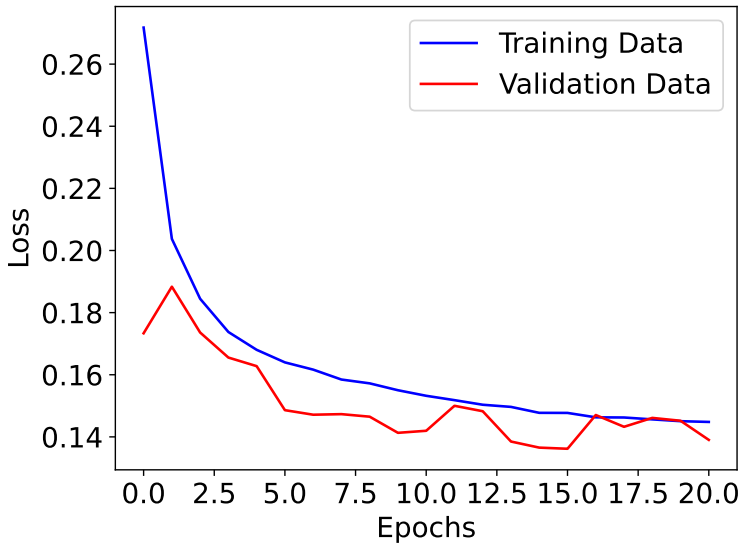

Figure 4.4: Loss function over the epochs of training for the Radio training and validation data sets.

4.4 Results

Figure 4.5 shows the density of the CSM generated by the neural network algorithm, as a function of f and p, for the three machine learning models considered. The top panel shows the RS and FS X-ray model, the middle panel shows the FS model, and the bottom panel shows the radio model. Each curve is generated independently of the others. The X-ray models use the variable f to simulate the varying sizes of the emitting region, while the radio model employs the $p = 1 - f$ variable.

In all models, an increase in the emitting region, corresponding to a larger f in the X-ray models and larger p in the radio model, leads to an increase of the location where the density peaks, and a drop in the density at the peak. This result is expected, as a larger emitting region implies that less mass is needed to get a similar total flux.

In the Tables 4.1, 4.2, 4.3 we can see how the four parameters describing the CSM change with f and p. In the tables, dR and R_1 are normalized with respect to $R_n = 3 \times 10^{16} cm$.

Table 4.1: Best parameters as a function of f for the forward shock and reverse shock X-ray Model.

f	α_1	α_2	R_1	dR
0.2	0.69	-2.54	0.05	1.98
0.5	0.75	-2.84	0.09	2.04
0.8	0.82	-3.14	0.13	2.09
1.0	0.86	-3.33	0.16	2.12

Table 4.2: Best parameters as a function of f for the forward shock X-ray Model.

f	α_1	α_2	R_1	dR
0.2	0.69	-2.37	0.03	1.83
0.5	0.71	-2.41	0.05	1.92
0.8	0.74	-2.65	0.06	2.09
1.0	0.76	-2.81	0.08	2.21

In order to understand how the parametes of the CSM depend on the size of the emitting region, in Figure 4.6 we show how the maximum density, ρ_{peak}, and the initial shell position, R_1, vary as a function of f for the x-ray models and p for the radio model. As shown by Margutti, Kamble, et al. 2017; Brethauer, Margutti, Milisavljevic, Bietenholz, et al. 2022;

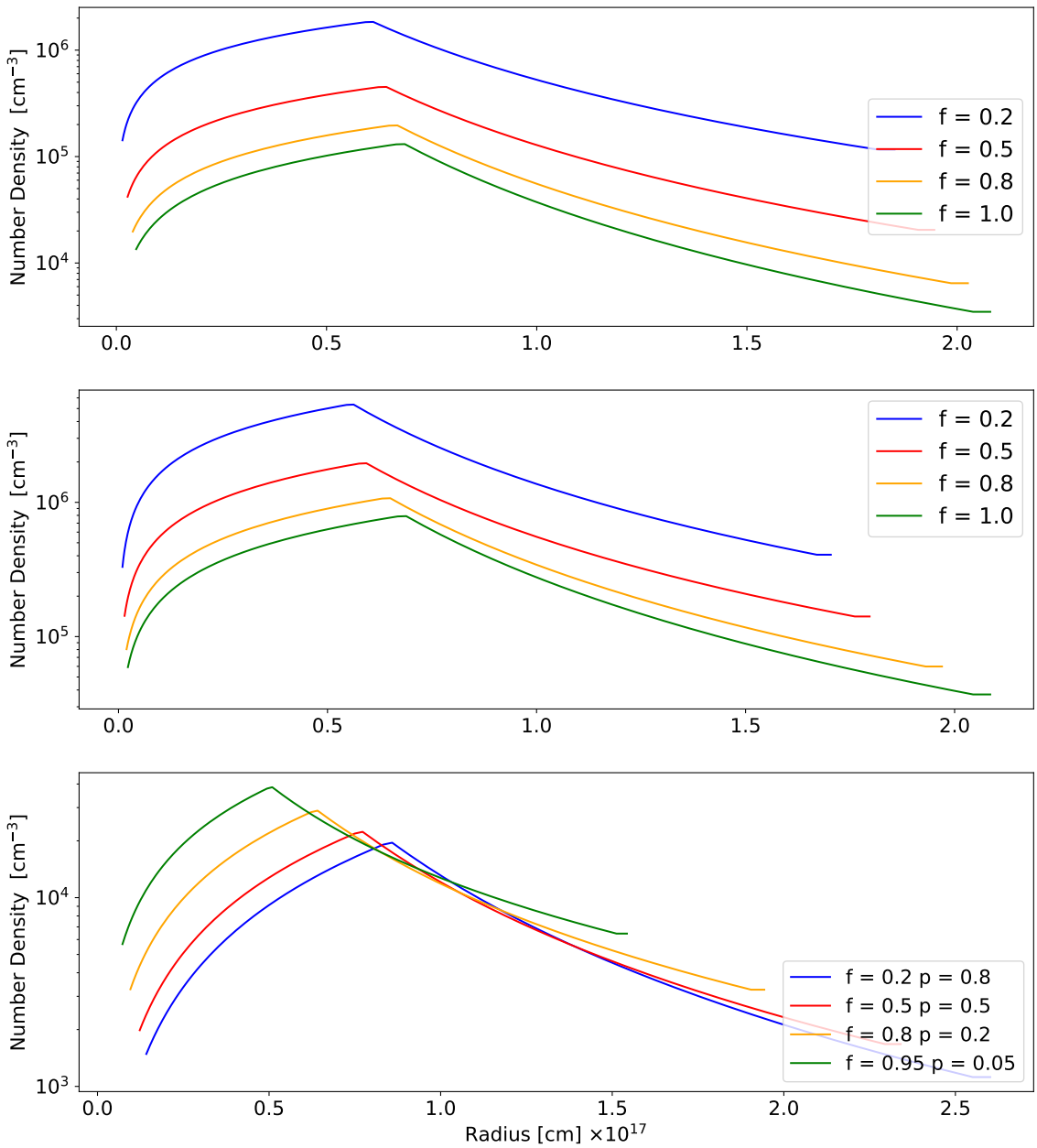

Figure 4.5: Density profile for the three machine learning models. *Top panel:* forward and reverse shock X-ray model. *Mid panel:* forward shock model. *Bottom panel:* radio model. The curves are created independently of each other. The first two models use the variable f to simulate the different sizes of the emitting region, while the radio model uses the $p = 1 - f$ variable.

Table 4.3: Best parameters as a function of f for the radio model.

p	α_1	α_2	R_1	dR
0.2	1.45	-2.63	0.47	2.37
0.5	1.33	-2.38	0.41	2.15
0.8	1.16	-2.01	0.32	1.81
1.0	0.99	-1.64	0.24	1.45

Vargas et al. 2022, the X-ray emission is consistent with a shell with a peak density $\rho_{peak} \approx 10^6 cm^{-3}$ and located approximately at $R_1 \approx 10^{16} cm$, corresponding to a total shell mass $M \approx 3 M_\odot$. Also, as discussed in Vargas et al. 2022, the shell density drop should follow $\rho(r) \approx r^{-3}$. Figure 4.6 shows that, although these restrictions are not used at any moment in the machine learning model, the results are consistent with those obtained in previous works for the X-ray emission. With respect to the X-ray models, Figure 4.6 also shows that quite different outcome are expected if the emission comes from the FS or if the emission comes from the FS and RS. In the latter case, the density is larger independently on the value of f, and the shell is located at larger radii. The density of the material emitting in radio is also located at a larger distance (nearly ~ 10 times larger than in the FS model), and with a smaller density (by ~ 2 orders of magnitude).

In Figure 4.7 we show how the density is distributed with respect to mass. Regions with lower f need more mass to compensate the loss in the emitting area. As discussed above, the radio emission is consistent with shells with a mass much lower than the X-ray emission.

A drawback of the machine learning method used in this work is that it is able to select, given a value of p and f, the best set of parameters. Nevertheless, it can not select, among all best models found at different f and p, the one that reproduces better the observations. To estimate it, we compare the synthetic observations for the models with $f = 0.2, 0.5, 0.8$ with the existing observations. By minimizing the chi-squared, we get that the best values of f are $f = 0.2$ for the forward and reverse shock model, $f = 0.5$ for the forward X-ray model, and $f = p = 0.5$ for the radio emission. In synthesis, our best model has 50% of the solid angle occupied by a massive shell, with a mass of ≈ 3.8 $M_\odot$, in which the forward shock is responsible for the X-rays emission, and a less dense region, occupying the remaining 50% of the solid angle, with a mass of 0.1 $M_\odot$, responsible for the radio emission.

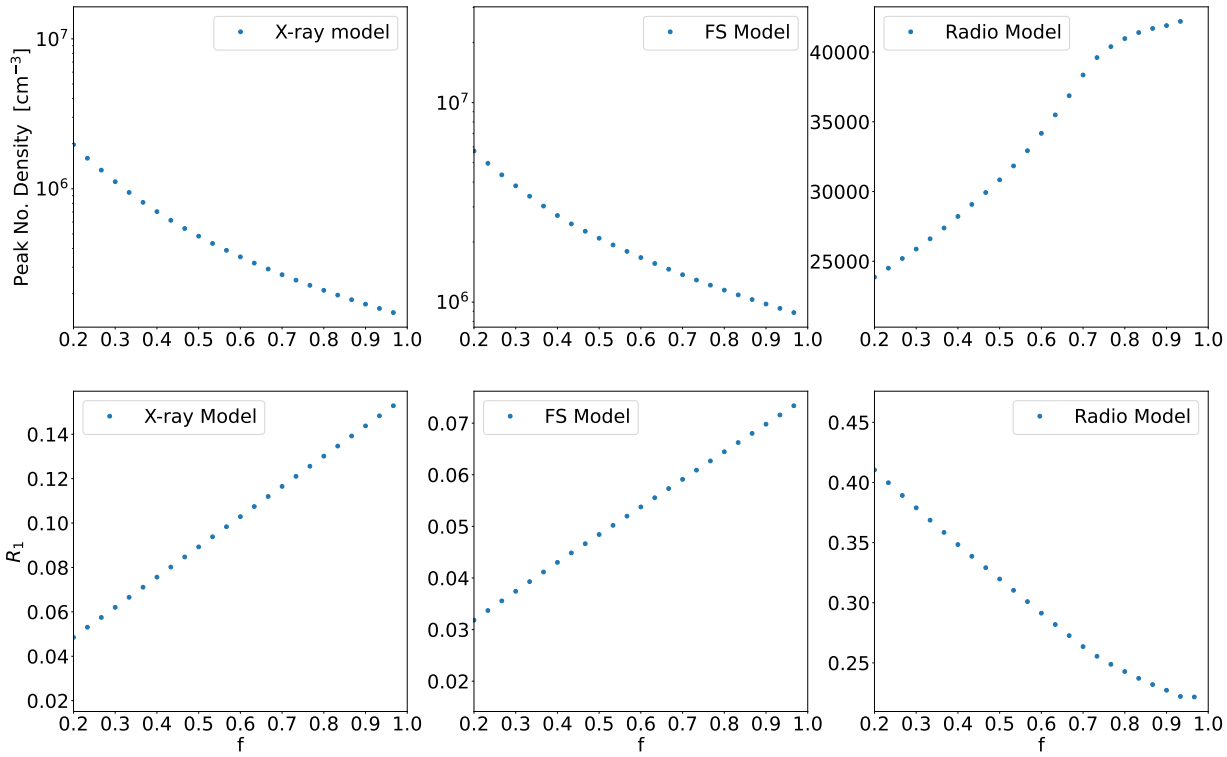

Figure 4.6: Peak density (top panels) and initial position of the shell (bottom) as function of f. From left to right panels: Forward and reverse shock X-ray model, Forward Shock model and Radio model.

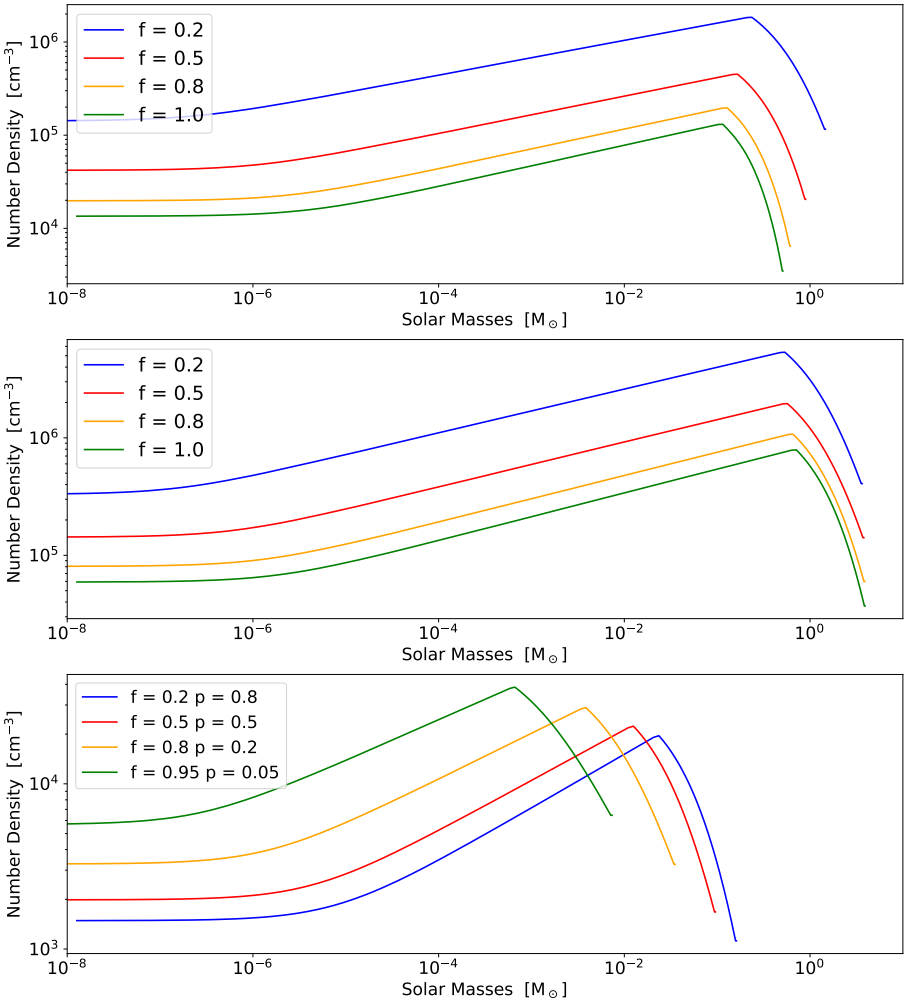

Figure 4.7: Mass coordinate shell density profile in mass coordinates for different values of f and p. From top to bottom panels, forward and reverse shock X-ray model, forward shock model and radio model.

4.5 Discussion and conclusions

In this paper, we study the angular structure of the SN 2014C. We run a large number of one-dimensional, spherical symmetric simulations. We changed the parameters of the CSM and follow the propagation of the SN ejecta through it. We post-process the results of the numerical simulation by producing synthetic observations. These are then used to train a neural network. By feeding the neural network with real radio and X-rays observational data, the neural network is thus able to recover the structure of the CSM.

The CSM is stratified in the angular direction. The X-ray emission is consistent with $\sim 50\%$ of the solid angle occupied by a dense shell, with a maximum density of 2×10^6 cm^{-3} located at 2×10^{16} cm, with a total mass of 3.8 $M_\odot$, while the radio emission is consistent with a region with a density about 100 times lower (2×10^4 cm^{-3}) peaking approximately at the same location as the X-ray emission, and with a mass of ~ 0.1 $M_\odot$.

Our results demonstrate that our machine learning approach can accurately infer the initial conditions of the supernova from its observed emission, with a significant reduction in the number of required simulations. This opens up new possibilities for modeling supernovae and other astrophysical systems, by enabling efficient exploration of large parameter spaces and reducing the computational cost of simulations.

Acknowledgements

We acknowledge the computing time granted by DGTIC UNAM (project LANCAD-UNAM-DGTIC-281).

Software

Matplotlib Hunter 2007, NumPy Contributors 2021, Mezcal De Colle, Granot, et al. 2012.

Chapter 5

Conclusions

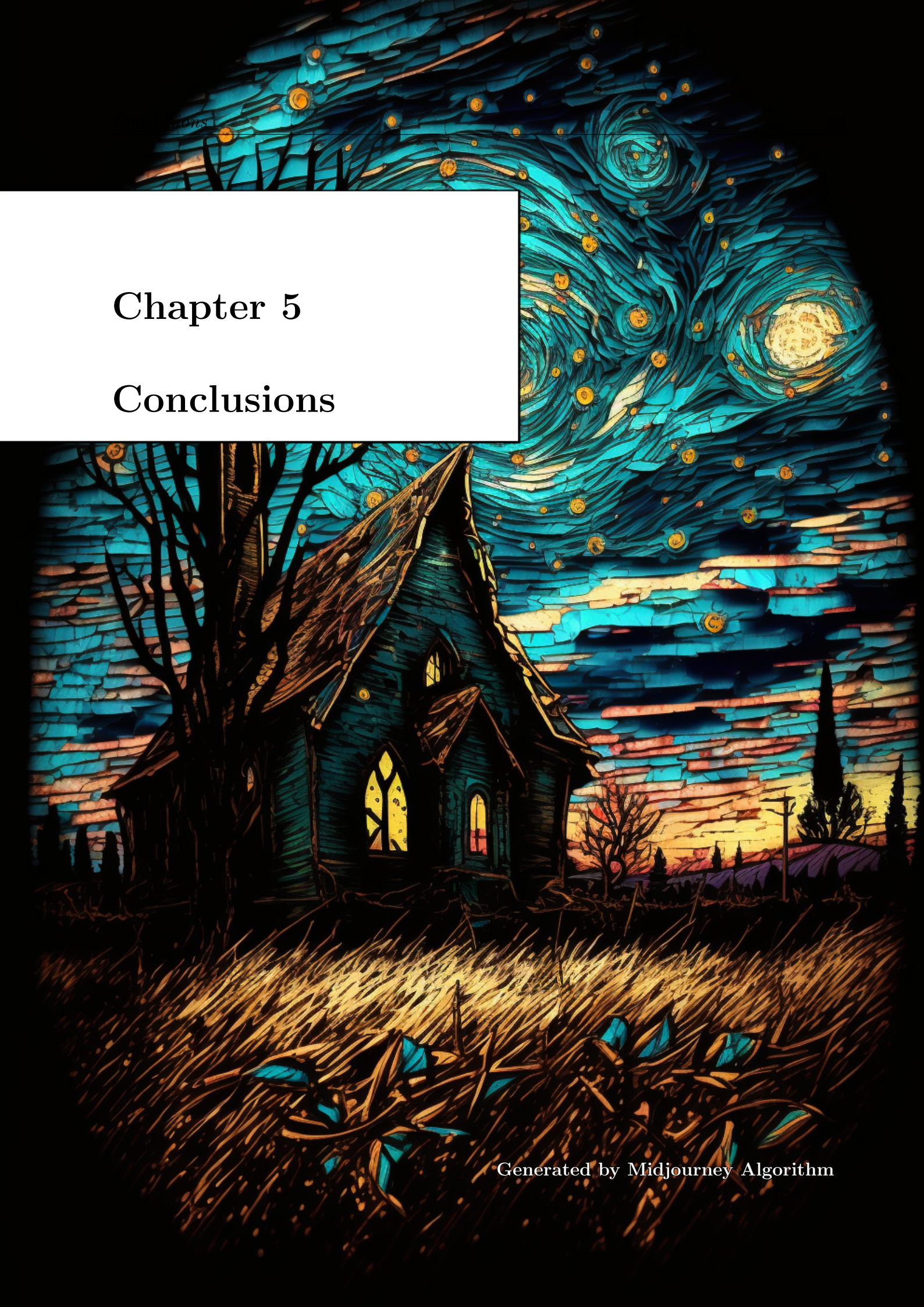

Generated by Midjourney Algorithm

Although the first paper presented in this thesis represents a detailed model of the interaction between the SN ejecta and the surrounding massive CSM, several ingredients are still missing from our model. In particular, we have explored only one pre SN structure; we have modeled only the X-ray emission, while radio emission (especially images obtained by VLBI; see, e.g., Bietenholz, Bartel, et al. 2021) contains detailed information about the evolution of the shock and its interaction with the medium; we have not included a detailed treatment of the photoionization of the upwind medium, which can affect the bound-free absorption. Finally, and most importantly, we assumed that the shell structure is spherically symmetric.

Radio and X-ray emission allows us to understand the mass-loss history of core-collapse SN progenitors on timescales that are impossible to study by direct observations. As we have shown in this paper, optimization methods can be used, coupled with hydrodynamical simulations, to model the density stratification of the environment once data at several epochs are available, as in the case of SN 2014C. The X-ray emission tracks the FS and RS emission, depending on the density of the environment and the ejecta velocity. The Hα emission tracks the shocked shell and the unshocked medium photoionized by the X-ray and UV radiation. Altogether, a detailed fit of the different components can help us to get a better understanding of this system. Then, coupled with detailed modeling of the radio emission, this analysis can allow us to determine the microphysical parameters as a function of time (which are usually degenerate with the density of the environment and ejecta velocity), giving us direct information on the particle acceleration process. In this paper, we describe this technique by analyzing the X-ray bremsstrahlung emission. The extension to radio and optical emission will be considered in a future study.

In the second paper we examine the angular structure of SN 2014C using one-dimensional, spherically symmetric simulations. The parameters of the CSM were adjusted, and the SN ejecta's propagation through it was followed. Synthetic observations were produced to post-process the results of the numerical simulation, and a neural network was trained using these observations. The neural network was then fed with real observational data from radio and X-ray sources to recover the CSM's structure.

The CSM was found to be stratified in the angular direction, with X-ray emission consistent with a dense shell occupying about 50% of the solid angle, with a maximum density of 2×10^6 cm^{-3} located at 2×10^{16} cm, and a mass of 3.8 M$_\odot$. The radio emission was consistent with a region with a density about 100 times lower (2×10^4 cm^{-3}) peaking approximately at the same location as the X-ray emission, with a mass of about 0.1 M$_\odot$.

The study shows that the machine learning approach can accurately determine the super-

nova's initial conditions from its observed emission, reducing the number of required simulations significantly. This method opens up new possibilities for modeling supernovae and other astrophysical systems by efficiently exploring large parameter spaces and reducing computational costs. After a thorough analysis of the data and simulations, it is clear that there is still much to be explored and understood in the field of core-collapse supernovae. The work presented in this paper is just one step towards a more complete picture of the complex interactions between the supernova ejecta and the surrounding medium.

Despite the limitations and simplifications made in our models, we were able to gain valuable insights into the density structure of the environment surrounding SN 2014C. Our optimization methods, coupled with hydrodynamical simulations, allowed us to model the density stratification of the environment once data at several epochs were available. By analyzing the X-ray bremsstrahlung emission, we were able to track the forward and reverse shock emission, depending on the density of the environment and the ejecta velocity. Furthermore, by analyzing the Hα emission, we could track the shocked shell and the unshocked medium photoionized by the X-ray and UV radiation.

To overcome these limitations, future studies should include a more detailed modeling of the radio and optical emission and incorporate a more accurate treatment of the photoionization of the upwind medium. Moreover, to accurately model the non-spherical nature of the supernova ejecta and the surrounding medium, three-dimensional simulations are needed.

The work presented, despite its limitations, represents an important step forward in our understanding of core-collapse supernovae. The insights gained from this study will undoubtedly guide future theoretical work in this field. By combining hydrodynamical simulations with optimization methods and multi-wavelength observations, we can gain a more complete understanding of these fascinating astrophysical events.

Bibliography

Aller, L. H. (1984): *Physics of thermal gaseous nebulae*. DOI: 10.1007/978-94-010-9639-3.

Anderson et al. (Apr. 2017): "The peculiar mass-loss history of SN 2014C as revealed through AMI radio observations". In: *mnras* 466.3, pp. 3648–3662. DOI: 10.1093/mnras/stw3310. arXiv: 1612.06059 [astro-ph.HE].

Anupama et al. (Oct. 2005): "The Peculiar Type Ib Supernova SN 2005bf: Explosion of a Massive He Star with a Thin Hydrogen Envelope?" In: *ApJL* 631.2, pp. L125–L128. DOI: 10.1086/497336. arXiv: astro-ph/0509625 [astro-ph].

Aretxaga, Itziar et al. (Oct. 1999): "SN 1988Z: spectro-photometric catalogue and energy estimates*". In: *MNRAS* 309.2, pp. 343–354. DOI: 10.1046/j.1365-8711.1999.02830.x. arXiv: astro-ph/9905313 [astro-ph].

Arnett and Meakin (Nov. 2011): "Turbulent Cells in Stars: Fluctuations in Kinetic Energy and Luminosity". In: *apj* 741.1, 33, p. 33. DOI: 10.1088/0004-637X/741/1/33. arXiv: 1012.1848 [astro-ph.SR].

Ben-Ami, Sagi et al. (Apr. 2014): "SN 2010mb: Direct Evidence for a Supernova Interacting with a Large Amount of Hydrogen-free Circumstellar Material". In: *ApJ* 785.1, 37, p. 37. DOI: 10.1088/0004-637X/785/1/37. arXiv: 1309.6496 [astro-ph.SR].

Benetti, Cappellaro, et al. (Dec. 2006): "Supernova 2002ic: The Collapse of a Stripped-Envelope, Massive Star in a Dense Medium?" In: *apjl* 653.2, pp. L129–L132. DOI: 10.1086/510667. arXiv: astro-ph/0611125 [astro-ph].

Benetti, Patat, et al. (May 1994): "Narrow features in the early spectrum of SN 1993J". In: *aap* 285, pp. L13–L16.

Bietenholz and Bartel (June 2005): "An Upper Limit on the Expansion Velocity of Gamma-Ray Burst Candidate SN 2001em". In: *apjl* 625.2, pp. L99–L102. DOI: 10.1086/431281. arXiv: astro-ph/0504671 [astro-ph].

— (Aug. 2007): "SN 2001em: No Jet-driven Gamma-Ray Burst Event". In: *apjl* 665.1, pp. L47–L50. DOI: 10.1086/521048. arXiv: 0706.3344 [astro-ph].

Bietenholz, Bartel, et al. (Jan. 2021): "SN 2014C: VLBI image shows a shell structure and decelerated expansion". In: *Monthly Notices of the Royal Astronomical Society* 502.2, pp. 1694–1701. ISSN: 0035-8711. DOI: 10.1093/mnras/staa4003. eprint: https://academic.oup.com/mnras/article-pdf/502/2/1694/36198286/staa4003.pdf. URL: https://doi.org/10.1093/mnras/staa4003.

Bietenholz, De Colle, et al. (May 2014): "Radio limits on off-axis GRB afterglows and VLBI observations of SN 2003gk". In: *mnras* 440.1, pp. 821–832. DOI: 10.1093/mnras/stu246. arXiv: 1310.7171 [astro-ph.HE].

Bietenholz, Kamble, et al. (Apr. 2018): "SN 2014C: VLBI images of a supernova interacting with a circumstellar shell". In: *mnras* 475.2, pp. 1756–1764. DOI: 10.1093/mnras/stx3194. arXiv: 1707.09935 [astro-ph.HE].

Bodenheimer, Peter et al. (Dec. 2006): *Numerical methods in astrophysics*. en. Series in Astronomy and Astrophysics. Boca Raton, FL: CRC Press.

Branch, David and J. Craig Wheeler (2017a): *Supernova Explosions*. Springer.

Branch and Wheeler (2017b): *Supernova Explosions*. DOI: 10.1007/978-3-662-55054-0.

Brethauer, D., Margutti, Milisavljevic, Bietenholz, et al. (Nov. 2022): "Seven Years of Coordinated Chandra-NuSTAR Observations of SN 2014C Unfold the Extreme Mass-loss History of Its Stellar Progenitor". In: *ApJ* 939.2, 105, p. 105. DOI: 10.3847/1538-4357/ac8b14. arXiv: 2206.00842 [astro-ph.HE].

Brethauer, Margutti, Milisavljevic, and M. Bietenholz (Dec. 2020): "Six Years of Luminous X-Ray Emission from the Strongly Interacting Ypye-Ib SN2014C Captured by Chandra and NuSTAR". In: *Research Notes of the American Astronomical Society* 4.12, 235, p. 235. DOI: 10.3847/2515-5172/abd252.

Burrows, David N. et al. (Oct. 2005): "The Swift X-Ray Telescope". In: *SSR* 120.3-4, pp. 165–195. DOI: 10.1007/s11214-005-5097-2. arXiv: astro-ph/0508071 [astro-ph].

Canto, J., S. Curiel, and E. Martinez-Gomez (July 2009): "A simple algorithm for optimization and model fitting: AGA (asexual genetic algorithm)". In: *aap* 501.3, pp. 1259–1268. DOI: 10.1051/0004-6361/200911740. arXiv: 0905.3712 [astro-ph.IM].

Chandra, Poonam (Feb. 2018): "Circumstellar Interaction in Supernovae in Dense Environments—An Observational Perspective". In: *SSR* 214.1, 27, p. 27. DOI: 10.1007/s11214-017-0461-6. arXiv: 1712.07405 [astro-ph.HE].

Chandra et al. (Apr. 2022): "VizieR Online Data Catalog: 19yrs of radio and X-ray obs. of SN 2001em (Chandra+, 2020)". In: *VizieR Online Data Catalog*, J/ApJ/902/55, J/ApJ/902/55.

Chandrasekhar, S. (July 1931): "The Maximum Mass of Ideal White Dwarfs". In: *apj* 74, p. 81. DOI: 10.1086/143324.

Charbonneau, P. (Dec. 1995): "Genetic Algorithms in Astronomy and Astrophysics". In: *ApJS* 101, p. 309. DOI: 10.1086/192242.

Chen et al. (Nov. 2018): "SN 2017ens: The Metamorphosis of a Luminous Broadlined Type Ic Supernova into an SN IIn". In: *apjl* 867.2, L31, p. L31. DOI: 10.3847/2041-8213/aaeb2e. arXiv: 1808.04382 [astro-ph.SR].

Chevalier (July 1982a): "Self-similar solutions for the interaction of stellar ejecta with an external medium." In: *apj* 258, pp. 790–797. DOI: 10.1086/160126.

— (Aug. 1982b): "The radio and X-ray emission from type II supernovae." In: *apj* 259, pp. 302–310. DOI: 10.1086/160167.

Chevalier and Fransson (2003): "Supernova Interaction with a Circumstellar Medium". In: *Supernovae and Gamma-Ray Bursters*. Ed. by K. Weiler. Vol. 598, pp. 171–194. DOI: 10.1007/3-540-45863-810.

— (Nov. 2006): "Circumstellar Emission from Type Ib and Ic Supernovae". In: *ApJ* 651.1, pp. 381–391. DOI: 10.1086/507606. arXiv: astro-ph/0607196 [astro-ph].

Chevalier, Fransson, and Nymark (Apr. 2006): "Radio and X-Ray Emission as Probes of Type IIP Supernovae and Red Supergiant Mass Loss". In: *apj* 641.2, pp. 1029–1038. DOI: 10.1086/500528. arXiv: astro-ph/0509468 [astro-ph].

— (Apr. 2017): "Radio and X-Ray Emission as Probes of Type IIP Supernovae and Red Supergiant Mass Loss". In: *apj* 641.2, pp. 1029–1038. DOI: 10.1086/500528. arXiv: astro-ph/0509468 [astro-ph].

Chevalier, Roger A. (May 1998): "Synchrotron Self-Absorption in Radio Supernovae". In: *apj* 499.2, pp. 810–819. DOI: 10.1086/305676.

— (June 2012): "Common Envelope Evolution Leading to Supernovae with Dense Interaction". In: *apjl* 752.1, L2, p. L2. DOI: 10.1088/2041-8205/752/1/L2. arXiv: 1204.3300 [astro-ph.HE].

Chevalier, Roger A. and Edison P. Liang (Sept. 1989): "The Interaction of Supernovae with Circumstellar Bubbles". In: *ApJ* 344, p. 332. DOI: 10.1086/167802.

Chollet, François et al. (2015): *Keras*. https://keras.io.

Chugai (Jan. 1997): "Supernovae in dense winds". In: *apss* 252, pp. 225–236. DOI: 10.1023/A:1000847125928.

Chugai and Chevalier (Apr. 2006): "Late Emission from the Type Ib/c SN 2001em: Overtaking the Hydrogen Envelope". In: *apj* 641.2, pp. 1051–1059. DOI: 10.1086/500539. arXiv: astro-ph/0510362 [astro-ph].

Chugai, Chevalier, and Utrobin (June 2007): "Optical Signatures of Circumstellar Interaction in Type IIP Supernovae". In: *apj* 662.2, pp. 1136–1147. DOI: 10.1086/518160. arXiv: astro-ph/0703468 [astro-ph].

Chugai, N. N. and I. J. Danziger (May 1994): "SN 1988Z: low-mass ejecta colliding with the clumpy wind?" In: *Monthly Notices of the Royal Astronomical Society* 268.1, pp. 173–180. ISSN: 0035-8711. DOI: 10.1093/mnras/268.1.173. eprint: https://academic.oup.com/mnras/article-pdf/268/1/173/3196597/mnras268-0173.pdf. URL: https://doi.org/10.1093/mnras/268.1.173.

Contributors, NumPy (2021): *NumPy*. https://numpy.org.

Corsi et al. (Feb. 2014): "A Multi-wavelength Investigation of the Radio-loud Supernova PTF11qcj and its Circumstellar Environment". In: *apj* 782.1, 42, p. 42. DOI: 10.1088/0004-637X/782/1/42. arXiv: 1307.2366 [astro-ph.HE].

da Silva, L. A. L. (Apr. 1993): "The classification of supernovae". In: *apss* 202, pp. 215–236. DOI: 10.1007/BF00626878.

De Colle, F. and A. C. Raga (Apr. 2006): "MHD simulations of radiative jets from young stellar objects. Hα emission". In: *aap* 449.3, pp. 1061–1066. DOI: 10.1051/0004-6361:20053300. arXiv: astro-ph/0512199 [astro-ph].

De Colle, Granot, et al. (Jan. 2012): "Gamma-ray burst dynamics and afterglow radiation from adaptive mesh refinement, special relativistic hydrodynamic simulations." In: *The Astrophysical Journal* 746.2, p. 122. DOI: 10.1088/0004-637x/746/2/122.

De Colle, Kumar, and Aguilera-Dena (Aug. 2018a): "Radio Emission from the Cocoon of a GRB Jet: Implications for Relativistic Supernovae and Off-axis GRB Emission". In: *The Astrophysical Journal* 863.1, p. 32. DOI: 10.3847/1538-4357/aad04d.

— (Aug. 2018b): "Radio Emission from the Cocoon of a GRB Jet: Implications for Relativistic Supernovae and Off-axis GRB Emission". In: *The Astrophysical Journal* 863.1, p. 32. DOI: 10.3847/1538-4357/aad04d.

De Colle, Raga, et al. (June 2014): "A stellar wind origin for the G2 cloud: three-dimensional numerical simulations." In: *The Astrophysical Journal* 789.2, p. L33. DOI: 10.1088/2041-8205/789/2/l33.

De Geyter et al. (Feb. 2013): "FitSKIRT: genetic algorithms to automatically fit dusty galaxies with a Monte Carlo radiative transfer code". In: *aap* 550, A74, A74. DOI: 10.1051/0004-6361/201220126. arXiv: 1212.0538 [astro-ph.CO].

De Jager, Nieuwenhuijzen, and van der Hucht (Feb. 1988): "Mass loss rates in the Hertzsprung-Russell diagram." In: *aaps* 72, pp. 259–289.

Dessart, Audit, and Hillier (Apr. 2015): "Numerical simulations of superluminous supernovae of type IIn". In: *Monthly Notices of the Royal Astronomical Society* 449.4, pp. 4304–4325. ISSN: 0035-8711. DOI: 10.1093/mnras/stv609. eprint: https://academic.oup.com/mnras/article-pdf/449/4/4304/18512550/stv609.pdf.

Dessart and Hillier (Apr. 2022): "Modeling the signatures of interaction in Type II supernovae: UV emission, high-velocity features, broad-boxy profiles". In: *AAP* 660, L9, p. L9. DOI: 10.1051/0004-6361/202243372. arXiv: 2204.00446 [astro-ph.SR].

Dwarkadas, . and Gruszko (Jan. 2012): "What are published X-ray light curves telling us about young supernova expansion?" In: *mnras* 419.2, pp. 1515–1524. DOI: 10.1111/j.1365-2966.2011.19808.x. arXiv: 1109.2616 [astro-ph.HE].

Dwarkadas, V. V. (Apr. 2011): "On luminous blue variables as the progenitors of core-collapse supernovae, especially Type IIn supernovae". In: *mnras* 412.3, pp. 1639–1649. DOI: 10.1111/j.1365-2966.2010.18001.x. arXiv: 1011.3484 [astro-ph.SR].

Dwarkadas, V. V., D. Dewey, and F. Bauer (Sept. 2010): "Bursting SN 1996cr's bubble: hydrodynamic and X-ray modelling of its circumstellar medium". In: *Monthly Notices of the Royal Astronomical Society* 407.2, pp. 812–829. ISSN: 0035-8711. DOI: 10.1111/j.1365-2966.2010.16966.x. eprint: https://academic.oup.com/mnras/article-pdf/407/2/812/3890608/mnras0407-0812.pdf. URL: https://doi.org/10.1111/j.1365-2966.2010.16966.x.

Eldridge, J. J., N. Langer, and C. A. Tout (May 2010): "Type Ib/c supernovae in binary systems. I. Evolution and properties of the progenitor stars". In: 514, A53. DOI: 10.1051/0004-6361/200913118. arXiv: 1004.0843 [astro-ph.SR].

Faran et al. (July 2014): "Photometric and spectroscopic properties of Type II-P supernovae". In: *mnras* 442.1, pp. 844–861. DOI: 10.1093/mnras/stu955. arXiv: 1404.0378 [astro-ph.HE].

Ferland, G. J. et al. (2017): *Cloudy 17.01*. http://www.nublado.org. Accessed on: 2023-05-31.

Ferreira, Leonardo et al. (June 2020): "Galaxy Merger Rates up to z $\sim$ 3 Using a Bayesian Deep Learning Model: A Major-merger Classifier Using IllustrisTNG Simulation Data".

In: *ApJ* 895.2, 115, p. 115. DOI: 10.3847/1538-4357/ab8f9b. arXiv: 2005.00476 [astro-ph.GA].

Filippenko, Alexei V. (Jan. 1997): "Optical Spectra of Supernovae". In: *ARA&A* 35, pp. 309–355. DOI: 10.1146/annurev.astro.35.1.309.

Filippenko and R. Chornock (Oct. 2001): "Supernovae 2001ej, 2001em, 2001eq, 2001er, and 2001ew". In: *iaucirc* 7737, p. 3.

Foley et al. (Mar. 2007): "SN 2006jc: A Wolf-Rayet Star Exploding in a Dense He-rich Circumstellar Medium". In: *apjl* 657.2, pp. L105–L108. DOI: 10.1086/513145. arXiv: astro-ph/0612711 [astro-ph].

Fransson et al. (Dec. 2014): "High-density circumstellar interaction in the luminous Type IIn SN 2010jl: the first 1100 days." In: *The Astrophysical Journal* 797.2, p. 118. DOI: 10.1088/0004-637x/797/2/118.

Fraser et al. (Nov. 2013): "Detection of an outburst one year prior to the explosion of SN 2011ht." In: *The Astrophysical Journal* 779.1, p. L8. DOI: 10.1088/2041-8205/779/1/l8.

Freedman et al. (May 2001): "Final Results from the Hubble Space Telescope Key Project to Measure the Hubble Constant". In: *The Astrophysical Journal* 553.1, pp. 47–72. DOI: 10.1086/320638.

Gal-Yam, A. and D. C. Leonard (Apr. 2009): "A massive hypergiant star as the progenitor of the supernova SN 2005gl". In: *nat* 458.7240, pp. 865–867. DOI: 10.1038/nature07934.

Gal-Yam, A., O. Yaron, et al. (Feb. 2021): "Introducing a new Supernova classification type: SN Icn". In: *Transient Name Server AstroNote* 76, pp. 1–76.

Gehrels, N. et al. (Aug. 2004): "The Swift Gamma-Ray Burst Mission". In: *ApJ* 611.2, pp. 1005–1020. DOI: 10.1086/422091. arXiv: astro-ph/0405233 [astro-ph].

Giovanardi and Palla (Feb. 1989): "Revision and extension to low temperature of numerical estimates of the electron collisional rates for atomic hydrogen". In: *aaps* 77.2, pp. 157–160.

González-Casanova et al. (Jan. 2014): "The morphology and dynamics of jet-driven supernova remnants: the case of W49B." In: *The Astrophysical Journal* 781.2, p. L26. DOI: 10.1088/2041-8205/781/2/l26.

Guo, Fan et al. (Feb. 2012): "On the amplification of magnetic field by a supernova blast shock wave in a turbulent medium." In: *The Astrophysical Journal* 747.2, p. 98. DOI: 10.1088/0004-637x/747/2/98. URL: https://doi.org/10.1088/0004-637x/747/2/98.

Harris, C. E. and P. E. Nugent (May 2020): "Outside the Wall: Hydrodynamics of Type I Supernovae Interacting with a Partially Swept-up Circumstellar Medium". In: *ApJ* 894.2, 122, p. 122. DOI: 10.3847/1538-4357/ab879e. arXiv: 2004.03612 [astro-ph.HE].

Heger, Fryer, et al. (July 2003): "How Massive Single Stars End Their Life". In: *apj* 591.1, pp. 288–300. DOI: 10.1086/375341. arXiv: astro-ph/0212469 [astro-ph].

Heger, Langer, and Woosley (Jan. 2000): "Presupernova Evolution of Rotating Massive Stars. I. Numerical Method and Evolution of the Internal Stellar Structure". In: *apj* 528.1, pp. 368–396. DOI: 10.1086/308158. arXiv: astro-ph/9904132 [astro-ph].

Hoffman et al. (Dec. 2008): "The Dual-Axis Circumstellar Environment of the Type IIn Supernova 1997eg". In: *The Astrophysical Journal* 688.2, pp. 1186–1209. DOI: 10.1086/592261.

Hunter, John D. (2007): "Matplotlib: A 2D Graphics Environment". In: *Computing in Science &amp Engineering* 9.3, pp. 90–95. DOI: 10.1109/mcse.2007.55. URL: https://doi.org/10.1109/mcse.2007.55.

Janka, Hanke, et al. (Dec. 2012): "Core-collapse supernovae: Reflections and directions". In: *Progress of Theoretical and Experimental Physics* 2012.1, 01A309, 01A309. DOI: 10.1093/ptep/pts067. arXiv: 1211.1378 [astro-ph.SR].

Janka and Mueller (Feb. 1996): "Neutrino heating, convection, and the mechanism of Type-II supernova explosions." In: *aap* 306, p. 167.

Jin, Harim, Sung-Chul Yoon, and Sergei Blinnikov (Mar. 2021): "The Effect of Circumstellar Matter on the Double-peaked Type Ic Supernovae and Implications for LSQ14efd, iPTF15dtg, and SN 2020bvc". In: *ApJ* 910.1, 68, p. 68. DOI: 10.3847/1538-4357/abe0b1. arXiv: 2101.11171 [astro-ph.HE].

Kim, M. et al. (Jan. 2014): "Supernova 2014C in NGC 7331 = Psn J22370560+3424319". In: *Central Bureau Electronic Telegrams* 3777, p. 1.

Kuriyama, Naoto and Toshikazu Shigeyama (Mar. 2020): "Radiation hydrodynamical simulations of eruptive mass loss from progenitors of Type Ibn/IIn supernovae". In: *Astronomy &amp Astrophysics* 635, A127. DOI: 10.1051/0004-6361/201937226. URL: https://doi.org/10.1051/0004-6361/201937226.

Leitherer, C. (June 2010): "Empirical Mass-Loss Rates across the Upper Hertzsprung-Russell Diagram". In: *Hot and Cool: Bridging Gaps in Massive Star Evolution*. Ed. by C. Leitherer et al. Vol. 425. Astronomical Society of the Pacific Conference Series, p. 171. arXiv: 0903.0608 [astro-ph.SR].

Leonard et al. (June 2000): "Evidence for Asphericity in the Type IIN Supernova SN 1998S". In: *ApJ* 536.1, pp. 239–254. DOI: 10.1086/308910. arXiv: astro-ph/9908040 [astro-ph].

Lochner, Michelle et al. (Aug. 2016): "Photometric Supernova Classification with Machine Learning". In: *ApJS* 225.2, 31, p. 31. DOI: 10.3847/0067-0049/225/2/31. arXiv: 1603.00882 [astro-ph.IM].

Lykins, M. L. et al. (Mar. 2013): "Radiative cooling in collisionally ionized and photoionized plasmas". In: *mnras* 429.4, pp. 3133–3143. DOI: 10.1093/mnras/sts570. arXiv: 1212.1233 [astro-ph.HE].

Malik, Abhishek, Benjamin P Moster, and Christian Obermeier (Dec. 2021): "Exoplanet detection using machine learning". In: *Monthly Notices of the Royal Astronomical Society* 513.4, pp. 5505–5516. ISSN: 0035-8711. DOI: 10.1093/mnras/stab3692. eprint: https://academic.oup.com/mnras/article-pdf/513/4/5505/43865055/stab3692.pdf. URL: https://doi.org/10.1093/mnras/stab3692.

Margutti, Alexander, et al. (Mar. 2018): "The Binary Neutron Star Event LIGO/Virgo GW170817 160 Days after Merger: Synchrotron Emission across the Electromagnetic Spectrum". In: *apjl* 856.1, L18, p. L18. DOI: 10.3847/2041-8213/aab2ad. arXiv: 1801.03531 [astro-ph.HE].

Margutti, Kamble, et al. (Feb. 2017): "Ejection of the Massive Hydrogen-rich Envelope Timed with the Collapse of the Stripped SN 2014C". In: *apj* 835.2, 140, p. 140. DOI: 10.3847/1538-4357/835/2/140. arXiv: 1601.06806 [astro-ph.HE].

Margutti, Milisavljevic, et al. (Jan. 2014): "A Panchromatic View of the Restless SN 2009ip Reveals the Explosive Ejection of a Massive Star Envelope". In: *ApJ* 780.1, 21, p. 21. DOI: 10.1088/0004-637X/780/1/21. arXiv: 1306.0038 [astro-ph.HE].

Matheson, Thomas et al. (Sept. 2000): "Optical Spectroscopy of Supernova 1993J During Its First 2500 Days". In: 120.3, pp. 1487–1498. DOI: 10.1086/301518. arXiv: astro-ph/0006263 [astro-ph].

Matzner, Christopher D. and Christopher F. McKee (Jan. 1999): "The Expulsion of Stellar Envelopes in Core-Collapse Supernovae". In: *apj* 510.1, pp. 379–403. DOI: 10.1086/306571. arXiv: astro-ph/9807046 [astro-ph].

Mauerhan, Filippenko, et al. (June 2018): "Stripped-envelope supernova SN2004dk is now interacting with hydrogen-rich circumstellar material". In: *Monthly Notices of the Royal Astronomical Society* 478.4, pp. 5050–5055. ISSN: 0035-8711. DOI: 10.1093/mnras/sty1307. eprint: https://academic.oup.com/mnras/article-pdf/478/4/5050/25102312/sty1307.pdf. URL: https://doi.org/10.1093/mnras/sty1307.

Mauerhan, Smith, Filippenko, et al. (Apr. 2013): "The unprecedented 2012 outburst of SN 2009ip: a luminous blue variable star becomes a true supernova". In: *MNRAS* 430.3, pp. 1801–1810. DOI: 10.1093/mnras/stt009. arXiv: 1209.6320 [astro-ph.SR].

Mauerhan, Smith, Silverman, et al. (May 2013): "SN 2011ht: confirming a class of interacting supernovae with plateau light curves (Type IIn-P)". In: *MNRAS* 431.3, pp. 2599–2611. DOI: 10.1093/mnras/stt360. arXiv: 1209.0821 [astro-ph.SR].

Maund, J. R. et al. (2004): "The massive binary companion star to the progenitor of supernova 1993J". In: *Nature* 427.6970, pp. 129–131. DOI: 10.1038/nature02156.

Maund, Justyn R (Jan. 2018): "The very young resolved stellar populations around stripped-envelope supernovae". In: *Monthly Notices of the Royal Astronomical Society* 476.2, pp. 2629–2663. ISSN: 0035-8711. DOI: 10.1093/mnras/sty093. eprint: https://academic.oup.com/mnras/article-pdf/476/2/2629/24396686/sty093.pdf. URL: https://doi.org/10.1093/mnras/sty093.

McLaughlin, Brendan M. (Jan. 2001): "Inner-shell Photoionization, Fluorescence, and Auger Yields". In: *Spectroscopic Challenges of Photoionized Plasmas*. Ed. by Gary Ferland and Daniel Wolf Savin. Vol. 247. Astronomical Society of the Pacific Conference Series, p. 87.

Metzger, B. D. (Nov. 2010): "Relic proto-stellar discs and the origin of luminous circumstellar interaction in core-collapse supernovae". In: *mnras* 409.1, pp. 284–304. DOI: 10.1111/j.1365-2966.2010.17308.x. arXiv: 1004.4215 [astro-ph.HE].

Milisavljevic and Robert A. Fesen (Aug. 2013): "A Detailed Kinematic Map of Cassiopeia A's Optical Main Shell and Outer High-velocity Ejecta". In: *ApJ* 772.2, 134, p. 134. DOI: 10.1088/0004-637X/772/2/134. arXiv: 1306.2310 [astro-ph.HE].

Milisavljevic, Margutti, et al. (Dec. 2015): "Metamorphosis of SN 2014C: delayed interaction between a hydrogen-poor core-collapse supernova and a nearby circumstellar shell." In: *The Astrophysical Journal* 815.2, p. 120. DOI: 10.1088/0004-637x/815/2/120.

Morisset, Christophe (Dec. 2016): "Photoionization models of CALIFA HII regions. Genetic method". In: *arXiv e-prints*, arXiv:1612.04250, arXiv:1612.04250. arXiv: 1612.04250 [astro-ph.GA].

Moriya, Takashi J. and Keiichi Maeda (Aug. 2014): "Constraining Physical Properties of Type IIn Supernovae through Rise Times and Peak Luminosities". In: *ApJL* 790.2, L16, p. L16. DOI: 10.1088/2041-8205/790/2/L16. arXiv: 1406.7783 [astro-ph.HE].

Morozova, Piro, and Stefano Valenti (May 2018): "Measuring the Progenitor Masses and Dense Circumstellar Material of Type II Supernovae". In: *ApJ* 858.1, 15, p. 15. DOI: 10.3847/1538-4357/aab9a6. arXiv: 1709.04928 [astro-ph.HE].

Morrison, R. and D. McCammon (July 1983): "Interstellar photoelectric absorption cross sections, 0.03-10 keV." In: *apj* 270, pp. 119–122. DOI: 10.1086/161102.

Nakar, Ehud and Re'em Sari (Nov. 2010): "EARLY SUPERNOVAE LIGHT CURVES FOLLOWING THE SHOCK BREAKOUT". In: *The Astrophysical Journal* 725.1, p. 904. DOI: 10.1088/0004-637X/725/1/904. URL: https://dx.doi.org/10.1088/0004-637X/725/1/904.

Ni, Wei-Tou (2016): "Gravitational wave detection in space". In: *International Journal of Modern Physics D* 25.14, p. 1630001. DOI: 10.1142/S0218271816300019. eprint: https://doi.org/10.1142/S0218271816300019. URL: https://doi.org/10.1142/S0218271816300019.

Nomoto, K. et al. (Aug. 1993): "A type IIb model for supernova 1993J". In: *nat* 364.6437, pp. 507–509. DOI: 10.1038/364507a0.

Palliyaguru, N. T. et al. (Mar. 2021): "VLBI Observations of Supernova PTF11qcj: Direct Constraints on the Size of the Radio Ejecta". In: *The Astrophysical Journal* 910.1, p. 16. DOI: 10.3847/1538-4357/abe1c9.

Papenkova, M. et al. (Sept. 2001): "Supernova 2001em in UGC 11794". In: *iaucirc* 7722, p. 1.

Pastorello, Kochanek, et al. (Feb. 2018): "Supernovae 2016bdu and 2005gl, and their link with SN 2009ip-like transients: another piece of the puzzle". In: *MNRAS* 474.1, pp. 197–218. DOI: 10.1093/mnras/stx2668. arXiv: 1707.00611 [astro-ph.SR].

Pastorello, Smartt, et al. (June 2007): "A giant outburst two years before the core-collapse of a massive star". In: *nat* 447.7146, pp. 829–832. DOI: 10.1038/nature05825. arXiv: astro-ph/0703663 [astro-ph].

Pellegrino et al. (Oct. 2022): "The Diverse Properties of Type Icn Supernovae Point to Multiple Progenitor Channels". In: *ApJ* 938.1, 73, p. 73. DOI: 10.3847/1538-4357/ac8ff6. arXiv: 2205.07894 [astro-ph.HE].

Perley, D. A., S. Schulze, et al. (2021): "The Type Icn SN 2021csp: Implications for the Origins of the Fastest Supernovae and the Fates of Wolf-Rayet Stars". In: *The Astrophysical Journal* 920.2, p. L30.

Perley, Daniel A et al. (2020): "The Zwicky Transient Facility Bright Transient Survey. II. A Public Statistical Sample for Exploring Supernova Demographics". In: *Publications of the Astronomical Society of the Pacific* 132.1019, p. 114301.

Perley, Sollerman, et al. (Mar. 2022): "The Type Icn SN 2021csp: Implications for the Origins of the Fastest Supernovae and the Fates of Wolf-Rayet Stars". In: *ApJ* 927.2, 180, p. 180. DOI: 10.3847/1538-4357/ac478e. arXiv: 2111.12110 [astro-ph.HE].

Pooley, D. and W. H. G. Lewin (Apr. 2004): "Supernova 2001em in UGC 11794". In: *iaucirc* 8323, p. 2.

Pooley, Craig Wheeler, et al. (Sept. 2019): "Interaction of SN Ib 2004dk with a Previously Expelled Envelope". In: *The Astrophysical Journal* 883.2, p. 120. DOI: 10.3847/1538-4357/ab3e36.

Pozzo, M. et al. (Aug. 2004): "On the source of the late-time infrared luminosity of SN 1998S and other Type II supernovae". In: *mnras* 352.2, pp. 457–477. DOI: 10.1111/j.1365-2966.2004.07951.x. arXiv: astro-ph/0404533 [astro-ph].

Provencal, J. L. et al. (Feb. 1998): "Testing the White Dwarf Mass-Radius Relation with HIPPARCOS". In: *apj* 494.2, pp. 759–767. DOI: 10.1086/305238.

Rajpaul, Vinesh (Feb. 2012): "Genetic algorithms in astronomy and astrophysics". In: *arXiv e-prints*, arXiv:1202.1643, arXiv:1202.1643. arXiv: 1202.1643 [astro-ph.IM].

Rybicki, George B. and Alan P. Lightman (1986): *Radiative Processes in Astrophysics*.

Sakurai, Akira (1960): "On the problem of a shock wave arriving at the edge of a gas". In: *Communications on Pure and Applied Mathematics* 13.3, pp. 353–370. DOI: https://doi.org/10.1002/cpa.3160130303. eprint: https://onlinelibrary.wiley.com/doi/pdf/10.1002/cpa.3160130303. URL: https://onlinelibrary.wiley.com/doi/abs/10.1002/cpa.3160130303.

Salas, P. et al. (Jan. 2013): "SN 2007bg: the complex circumstellar medium around one of the most radio-luminous broad-lined Type Ic supernovae". In: *mnras* 428.2, pp. 1207–1217. DOI: 10.1093/mnras/sts104. arXiv: 1208.3455 [astro-ph.HE].

Schinzel, . et al. (Feb. 2009a): "SN 2001em: Not So Fast". In: *ApJ* 691.2, pp. 1380–1386. DOI: 10.1088/0004-637X/691/2/1380. arXiv: 0810.1478 [astro-ph].

Schinzel, F. K. et al. (Feb. 2009b): "SN 2001em: NOT SO FAST". In: *The Astrophysical Journal* 691.2, pp. 1380–1386. DOI: 10.1088/0004-637x/691/2/1380.

Schneider, V. et al. (Mar. 1993): "New Algorithms for Ultra-relativistic Numerical Hydrodynamics". In: *Journal of Computational Physics* 105.1, pp. 92–107. DOI: 10.1006/jcph.1993.1056.

Shivvers et al. (June 2015): "Early emission from the Type IIn supernova 1998S at high resolution." In: *The Astrophysical Journal* 806.2, p. 213. DOI: 10.1088/0004-637x/806/2/213. URL: https://doi.org/10.1088/0004-637x/806/2/213.

Silverman et al. (July 2013): "Type Ia Supernovae Strongly Interacting with Their Circumstellar Medium". In: *ApJS* 207.1, 3, p. 3. DOI: 10.1088/0067-0049/207/1/3. arXiv: 1304.0763 [astro-ph.CO].

Smith (Aug. 2014): "Mass Loss: Its Effect on the Evolution and Fate of High-Mass Stars". In: *araa* 52, pp. 487–528. DOI: 10.1146/annurev-astro-081913-040025. arXiv: 1402.1237 [astro-ph.SR].

— (2017a): "Interacting Supernovae: Types IIn and Ibn". In: *Handbook of Supernovae*. Ed. by Athem W. Alsabti and Paul Murdin, p. 403. DOI: 10.1007/978-3-319-21846-5_38.

Smith and W. David Arnett (Apr. 2014): "Preparing for an Explosion: Hydrodynamic Instabilities and Turbulence in Presupernovae". In: *apj* 785.2, 82, p. 82. DOI: 10.1088/0004-637X/785/2/82. arXiv: 1307.5035 [astro-ph.SR].

Smith, Li, Foley, et al. (Sept. 2007): "SN 2006gy: Discovery of the Most Luminous Supernova Ever Recorded, Powered by the Death of an Extremely Massive Star like η Carinae". In: *ApJ* 666.2, pp. 1116–1128. DOI: 10.1086/519949. arXiv: astro-ph/0612617 [astro-ph].

Smith, Weidong Li, Jeffrey M. Silverman, et al. (July 2011): "Luminous blue variable eruptions and related transients: diversity of progenitors and outburst properties". In: *MNRAS* 415.1, pp. 773–810. DOI: 10.1111/j.1365-2966.2011.18763.x. arXiv: 1010.3718 [astro-ph.SR].

Smith, N. (2017b): *Handbook of Supernovae*. Handbook of Supernovae. Springer International Publishing. ISBN: 9783319218458.

Soderberg, A. M. et al. (Nov. 2006): "The Radio and X-Ray Luminous SN 2003bg and the Circumstellar Density Variations around Radio Supernovae". In: *apj* 651.2, pp. 1005–1018. DOI: 10.1086/507571. arXiv: astro-ph/0512413 [astro-ph].

Sollerman et al. (Nov. 2020): "Two stripped envelope supernovae with circumstellar interaction. But only one really shows it". In: *AAP* 643, A79, A79. DOI: 10.1051/0004-6361/202038960. arXiv: 2009.04154 [astro-ph.HE].

Soraisam, Monika et al. (Feb. 2022): "Optical Rebrightening of Extragalactic Transients from the Zwicky Transient Facility". In: *ApJL* 926.2, L11, p. L11. DOI: 10.3847/2041-8213/ac4e99. arXiv: 2201.08936 [astro-ph.HE].

Stevance, H F et al. (Mar. 2020): "The shape of SN 1993J re-analysed". In: *Monthly Notices of the Royal Astronomical Society* 494.1, pp. 885–901. ISSN: 0035-8711. DOI: 10.1093/mnras/staa721. eprint: https://academic.oup.com/mnras/article-pdf/494/1/885/33009953/staa721.pdf.

Stockdale, C. J., B. Kaster, et al. (Jan. 2005): "Supernova 2001em in UGC 11794". In: *iaucirc* 8472, p. 4.

Stockdale, C. J., S. D. Van Dyk, et al. (Feb. 2004): "Supernova 2001em in UGC 11794". In: *iaucirc* 8282, p. 2.

Sun, Ning-Chen, Justyn R Maund, and Paul A Crowther (Aug. 2020): "The changing-type SN 2014C may come from an 11 Solar masses star stripped by binary interaction and violent eruption". In: *Monthly Notices of the Royal Astronomical Society* 497.4, pp. 5118–5135. ISSN: 0035-8711. DOI: 10.1093/mnras/staa2277. eprint: https://academic.oup.com/mnras/article-pdf/497/4/5118/33687738/staa2277.pdf.

Suzuki, Akihiro et al. (Feb. 2021): "Extremely Energetic Supernova Explosions Embedded in a Massive Circumstellar Medium: The Case of SN 2016aps". In: *ApJ* 908.1, 99, p. 99. DOI: 10.3847/1538-4357/abd6ce. arXiv: 2012.13283 [astro-ph.HE].

Tan, Jo C., Christopher D. Matzner, and Christopher F. McKee (Apr. 2001): "Trans-Relativistic Blast Waves in Supernovae as Gamma-Ray Burst Progenitors". In: *The Astrophysical Journal* 551.2, pp. 946–972. DOI: 10.1086/320245.

Tinyanont, Samaporn et al. (Dec. 2019): "Supernova 2014C: Ongoing Interaction with Extended Circumstellar Material with Silicate Dust". In: *The Astrophysical Journal* 887.1, p. 75. DOI: 10.3847/1538-4357/ab521b.

van Dyk, Schuyler D. et al. (Mar. 1996): "Type "IIn" Supernovae: A Search for Radio Emission". In: *aj* 111, p. 1271. DOI: 10.1086/117872.

Vargas, Felipe et al. (May 2022): "Survival of the Fittest: Numerical Modeling of SN 2014C". In: *ApJ* 930.2, 150, p. 150. DOI: 10.3847/1538-4357/ac649d. arXiv: 2102.12581 [astro-ph.HE].

Velázquez, P. F. et al. (Jan. 2017): "A 3D MHD simulation of SN 1006: a polarized emission study for the turbulent case". In: *Monthly Notices of the Royal Astronomical Society* 466.4, pp. 4851–4857. ISSN: 0035-8711. DOI: 10.1093/mnras/stx064. eprint: https://academic.oup.com/mnras/article-pdf/466/4/4851/10873964/stx064.pdf. URL: https://doi.org/10.1093/mnras/stx064.

Verner, D. A. and G. J. Ferland (n.d.): "Atomic Data for Astrophysics. I. Radiative Recombination Rates for H-like, He-like, Li-like, and Na-like Ions over a Broad Range of Temperature". In: *apjs* 103 (), p. 467. DOI: 10.1086/192284. arXiv: astro-ph/9509083 [astro-ph].

Verner, D. A., G. J. Ferland, et al. (n.d.): "Atomic Data for Astrophysics. II. New Analytic FITS for Photoionization Cross Sections of Atoms and Ions". In: *apj* 465 (), p. 487. DOI: 10.1086/177435. arXiv: astro-ph/9601009 [astro-ph].

Vogl, C. et al. (Jan. 2020): "Spectral modeling of type II supernovae. II. A machine-learning approach to quantitative spectroscopic analysis". In: *AAP* 633, A88, A88. DOI: 10.1051/0004-6361/201936137. arXiv: 1911.04444 [astro-ph.HE].

Weiler, Kurt W. et al. (Oct. 1991): "The 10 Year Radio Light Curves for SN 1979C". In: *ApJ* 380, p. 161. DOI: 10.1086/170571.

Wellons, Sarah, Alicia M. Soderberg, and Roger A. Chevalier (May 2012): "RADIO OBSERVATIONS REVEAL UNUSUAL CIRCUMSTELLAR ENVIRONMENTS FOR SOME TYPE Ibc SUPERNOVA PROGENITORS". In: *The Astrophysical Journal* 752.1, p. 17. DOI: 10.1088/0004-637x/752/1/17.

Yalinewich, Almog and Simon Portegies Zwart (Feb. 2019): "The Signature of a Windy Radio Supernova Progenitor in a Binary System". In: *The Astrophysical Journal Letters* 872.1, p. L3. DOI: 10.3847/2041-8213/ab01e4. URL: https://dx.doi.org/10.3847/2041-8213/ab01e4.

Yoon, Sung-Chul, Luc Dessart, and Alejandro Clocchiatti (May 2017): "Type Ib and IIb Supernova Progenitors in Interacting Binary Systems". In: *ApJ* 840.1, 10, p. 10. DOI: 10.3847/1538-4357/aa6afe. arXiv: 1701.02089 [astro-ph.SR].